`

UNIVERSITY OF CALIFORNIA,
IRVINE

Probing Single Molecules with a Tunable Femtosecond Laser Coupled RF-STM

DISSERTATION

submitted in partial satisfaction of the requirements
for the degree of

DOCTOR OF PHILOSOPHY

in Materials Science and Engineering

by

Weicai Cao

Dissertation Committee:
Professor Wilson Ho, Research Advisor
Professor Martha Mecartney, Committee Chair
Professor Regina Ragan

2015

`

`

DEDICATION

To

Annie and our family

`

TABLE OF CONTENTS

`

LIST OF FIGURES

`

ACKNOWLEDGMENTS

I would like to express the deepest appreciation to my research advisor, Professor Wilson Ho, for his guidance, support, and the great opportunity to work on the exciting projects in the Ho Group. Without his kind guidance and persistent support this dissertation would not have been possible. During these years I have been benefited from his high standard in conducting research in the frontier of science. The extraordinary experience working in the Ho Group prepared me for future challenges.

I would like to thank Professor Martha Mecartney for being my co-advisor and committee chair, I deeply appreciate for her kind advice, and I enjoyed being her head TA and got the best chances to practice my speaking and communicating. I would like to thank Professor Regina Ragan for serving in both my Advancement and Doctoral committees; I deeply appreciate for her kind advice. I would like to thank Professor Eric Potma and Professor Daniel Mumm who served in my Advancement committee.

It has been a great pleasure of working with all the Ho Group members during my years in the group: Ungdon Ham, Joonhee Lee, Qing Huan, Ying Jiang, Freddy Toledo, Chilun Jiang, Hikari Kimura, Zhumin Han, Chen Xu, Arthur Yu, Shaowei Li, Calvin Patel, Greg Czap, Haigang Zhang and Han Kyu Lee.

I would like to particularly thank a few members with whom I worked most closely with. Ungdon Ham, Freddy Toledo and Chilun Jiang who taught me about instrumentation; Calvin Patel for running the 4T-BTD molecule and PDI molecule experiments with me; Hikari Kimura who moved the STM system and set up the laser system with me; Arthur Yu for helping in the initial stage of moving; Shaowei Li, Arthur Yu, Greg Czap, Zhumin Han and Chen Xu for their

advice on the CO and H_2 imaging. I appreciate the help from all Ho group members when I need to transfer liquid helium.

I thank Gregory C. Welch and Prof. Guillermo C. Bazan at UCSB for the collaboration on the 4T-BTD molecule project. I thank Min Feng and Prof Hrvoje Petek at University of Pittsburgh for their collaboration on the PDI molecule project. I would also like to thank Yong Wang and Xuejun Liu from Potma Group, Yang Han and Yuan Feng from Ge group, Shawn Perdue and Joonhee Lee from the Apkarian Group for their advice on optics.

I would like to thank UCI Physical Science Machine Shop for their help on my instrumentation projects. I also thank UCI Laser Spectroscopy Facility for testing my PDI molecule samples and optical parts.

I would like to thank the Department of Chemical Engineering and Materials Science for providing support in the form of Teaching Assistant positions and fellowships.

I owe my loving thanks to my wife Annie and our family, who are always my firm support and great comfort.

Last but not least I would like to thank the support of the projects: National Science Foundation Center for Chemical Innovation at the Space-Time Limit (CaSTL) under Grant No. CHE-1414466.

`

WEICAI CAO

115, Verano Place, Irvine, CA 92617
wcao@uci.edu, weicaicao@gmail.com
(224)-436-6967

Education

University of California, Irvine, Ph.D.; Materials Science and Engineering 09/2015
Thesis Advisor: Dr. Wilson Ho

University of California, Irvine, M.S.; Materials Science and Engineering 03/2010
Graduate Advisor: Dr. Martha Mecartney

Huazhong University of Science and Technology, China, B.S.; Materials Science and Engineering 06/2008

Professional Skills

- Designing, constructing, maintaining and improving Scanning Tunneling Microscope (STM) along with related scientific instruments.
- Setting up and maintaining complicated tunable femtosecond laser system which covers wide wavelength range.
- Probing single molecules, single atoms and nanoclusters with a homemade tunable femtosecond laser (100fs, 210~1040nm) coupled low temperature (10 kelvin) ultrahigh vacuum (4×10^{-11} torr) Radio Frequency (80MHz) STM.
- Characterizing microstructure of materials with scanning electron microscope (SEM), atomic force microscope (AFM), transmission electron microscope (TEM) and x-ray diffraction (XRD); characterizing mechanical, optical and electrical properties of materials.
- Other skills: ultrahigh vacuum techniques; machining; data acquisition through instrument interface; software applications (Solidworks, AutoCAD, Origin, etc.); electronics; materials selection, design and synthesis.

Professional Experience

University of California, Irvine, Department of Physics & Astronomy and Department of Chemical Engineering and Materials Science
Graduate Research Assistant of Dr. Wilson Ho 07/2009-Present

- Moved a homemade STM system to a new lab; designed and assembled a molecular interlock system for exchange of evaporators; designed, machined and assembled atom and molecule evaporators; designed and built a mobile pump station (leak detector) to leak check and detect current of evaporators; designed and built a station to capture the helium (He) gas used during LHe LT experiments, co- designed and built systems for storage, purification, and liquefaction of He.

`

- Set up a new tunable femtosecond laser system that can cover whole solar spectrum from 210nm to 1040nm with second, third and fourth harmonic generations; overlapped two ultrafast laser beams (MaiTai fundamental+fundamental, fundamental+2^{nd} harmonic, fundamental+3^{rd} harmonic) spatially and temporally on the optical table and in the STM junction; co-designed, modified and built new microscopes to detect weak laser induced signal in the tunneling regime.
- Performed STM experiments of molecules, atoms and nanoclusters on oxide and metal surfaces (properties of these systems were probed at the single molecule level with sub-Å resolution; light molecule interactions mediated by plasmons at the nanoscale were also studied by combining laser with STM). Investigated molecules are C_{60}, alizarin, Th-Th-BT-Th-Th, azulene, and PDI, investigated atoms and nanoclusters included Ag, Au, Fe, K and Mg.

University of California, Irvine, Department of Chemical Engineering and Materials Science
Rotation Graduate Researcher 10/2008-07/2009

- Characterized microstructure and mechanical properties of nanocrystalline Ni; Synthesized and characterized microstructure and mechanical properties of Al_2O_3-YAG-ZrO_2 three phase ceramic; Characterized microstructure and catalytic activities of Au nanoparticles.

Huazhong University of Science and Technology, Department of Materials Science and Engineering, Undergraduate Researcher 09/2007-06/2008

- Synthesized and Characterized $LaMnO_3$ nanoparticles.

Teaching Experience

University of California, Irvine, Department of Chemical Engineering and Materials Science

- Teaching Assistant for the course "Materials Selection and Design" 2011
- Lead Teaching Assistant for the course "Advanced Lab on Synthesis & Characterization of Materials" 2012~2014

Publications

W. Cao, C. J. Patel, G. C. Welch, G. C. Bazan and W. Ho, to be submitted to *Nano Lett*.
"Imaging Molecular Orbitals of 4, 7-Di ([2, 20-bithiophen]-5-yl) benzo[c] [1, 2, 5] thiadiazole (4T-BTD) with a STM"

W. Cao, C.J. Patel, M. Feng, H. Petek and W. Ho, prepared to be submitted to *J. Chem. Phys*.
"Imaging Metal-Molecule Chain and Single Molecule of 1, 4-Phenylene Diisocyanide (PDI) on Noble Metal Surfaces and Their Interaction with Small Molecules"

Presentations

08/2015 250^{th} ACS National Meeting, Boston, MA, 2015,
W. Cao, C. J. Patel, S. Li, A. Yu, W. Ho *et al* "Chemical Imaging and Spectroscopy of Single Molecules with a Tunable Femtosecond Laser Coupled RF-STM"

`

Affiliations

American Chemical Society

Honors/Awards

Graduate Student Fellowship, UC Irvine 09/2008~06/2009
Outstanding Graduate, Huazhong University of Science and Technology 06/2008

`

ABSTRACT OF THE DISSERTATION

Probing Single Molecules with a Tunable Femtosecond Laser Coupled RF-STM

By

Weicai Cao

Doctor of Philosophy in Materials Science and Engineering

University of California, Irvine, 2015

Professor Wilson Ho, Research Advisor

Professor Martha Mecartney, co-Advisor and Chair

Scanning Tunneling Microscope (STM) has become a powerful tool in nanoscience for imaging, manipulation and electronic spectroscopy. STM inelastic electron tunneling spectroscopy (IETS) first achieved chemical identification of molecular species by characterizing vibrational energies. Recently, with the STM itProbe and H_2 rotational spectromicroscopy, molecular structure and chemical bonds are observed with the STM. Despite these successes in spatial resolution, various efforts have been made to combine fs laser with STM to overcome the temporal resolution limitation of STM, there is so far no clear evidence of simultaneous fs and Å resolution.

Electronic properties of organic molecules are of central importance to applications such as molecular electronics, organic LEDs, and solar cells. Properties of these molecules can be probed by the scanning tunneling microscope (STM) at the single molecule level and with sub-Å spatial resolution. The molecular orbital of 4, 7-Di ([2, 20-bithiophen]-5-yl) benzo[c] [1, 2, 5] thiadiazole (4T-BTD) with intramolecular donor-acceptor-donor sites is probed with the electronic state dI/dV imaging and H_2 rotational and vibrational spectromicroscopy. 1, 4-Phenylene Diisocyanide (PDI) is probed by imaging with a CO-terminated tip and H_2. PDI can

self-assemble on noble metal surfaces to form nanostructures, which could have potential applications in molecular electronics and catalysis.

Further combination of a RF-STM with a tunable femtosecond laser enables the investigation of light-molecule interactions. In this dissertation, efforts are spent to setup a new tunable fs laser (220 nm~1040 nm) to couple with the RF-STM. The effects of the femtosecond laser are followed by detecting photo induced electron emission and photochemistry. A new double lock-in technique is applied to detect the weak laser-induced signal in the tunneling regime. To sharpen the energy width and increase the lifetime of the excited states of molecules, thin aluminum oxide and copper oxide are grown on metal surfaces to provide electronic isolation of the metal substrate and adsorbed molecules. Metal nanoclusters are grown on metal and oxide to improve laser-induced signal through plasmonic enhancements.

`

Chapter 1

Introduction

1.1 Background of STM

Scanning tunneling microscopy (STM) has been a powerful tool to study surface sciences for imaging, spectroscopy and manipulation [1] after its invention in 1980's [2]. By modifying various experimental conditions such as temperature and pressure, coupling magnetic fields or electromagnetic radiation, and functionalizing the STM tip with single molecules, STM has demonstrated its versatility to probe chemistry and physics of various materials at the atomic scale.

The heart of STM is the quantum mechanical effect of tunneling through a potential barrier applied between two metallic leads. An applied potential difference between the sample and tip causes a tunneling electron current when the distance between the tip and sample is close, typically 5Å to 10Å. This current depends exponentially on the gap distance of the tip and sample surface, typically if the tip and surface get 1 Å closer, the tunneling current will become 10 times bigger. The tunneling current can be kept constant with STM electronics feedback on, which applies offset voltage to the STM piezos to keep a preset tunneling current. STM images obtained in this constant current mode are obtained by scanning the STM tip across the surface and adjusting the tip position required to maintain a constant current. These applied piezo voltages are used to reconstruct STM topographic images which are a convolution of the geometric and electronic structure of the surface [1, 3].

The tunneling current can be expressed by using first-order perturbation theory as:

`

$$I_T = \frac{4\pi e}{\hbar}\int_{-\infty}^{\infty} \rho_t\,(\varepsilon - \varepsilon V_T)\rho_s(\varepsilon)(f_t(\varepsilon - \varepsilon V_T) - f_s(\varepsilon))|M(\varepsilon - \varepsilon V_T)|^2 d\varepsilon \qquad (1.1)$$

where ρ_t and ρ_s represent the density of states (DOS) of the tip and sample respectively, $f_t(\varepsilon)$ and $f_s(\varepsilon)$ are temperature dependent Fermi distribution functions of the tip and sample respectively, and $|M(\varepsilon)|^2$ is the tunneling matrix element taking into account the coupling between the electron wavefunctions of the tip and sample. The difficulty in evaluating equation (1.1) lies in determining the tunneling matrix element which depends strongly on the local density of states of both the tip and surface. However, a simple approximation has been performed by *J. Tersoff* and *D. R. Hamman* [3, 4] to simplify the expression for the tunneling current.

In the *Tersoff-Hamman* approximation the STM tip is treated as atomically sharp where only the last atom in the tip contributes to the tunneling process. In addition, the only contributions of wavefunction states of the tip are those that have spherical s-like orbitals. Using these approximations and taking a zero temperature and low bias limit the tunneling current expression can be simplified to:

$$I_T \propto \rho_t \int_0^{eV_T} \rho_s(\varepsilon)d\varepsilon \qquad (1.2)$$

and the derivative of this expression with respect to voltage will give the differential conductance:

$$\frac{\partial I_T}{\partial V} \propto \rho_s(\varepsilon) \qquad (1.3)$$

which is direct measure of the local density of states (LDOS) of the sample surface or atoms and molecules adsorbed on the surface [1, 3 and 4].

STM electronic spectroscopy is performed in the constant height, the STM feedback electronics are off after the tunneling gap is set; the tunneling current is recorded as the sample bias is ramped in certain bias range. For STM, all the spectroscopy information is recorded in the I-V curve. I-V curve is mostly linear since the tunneling is predominantly a linear process. If

`

there are electronic states on the surface or molecules adsorbs on the surface, a step will appear in the I-V curve. Such a change is more apparent in the dI/dV curve, with a peak at the bias of the electronic states. Another reason to record dI/dV signal is expressed in equation 1.3, dI/dV is directly related to density of states on the surface or molecules adsorbs on the surface. The dI/dV signal can be readily recorded with lock-in detection by applying a small modulating bias to the tunneling bias.

Despite being a powerful tool in imaging, manipulation and spectroscopy, STM has its limitations, the first one being lack of chemical sensitivity. In 1998, STM inelastic electron tunneling spectroscopy (IETS) first achieved chemical identification of molecular species by characterizing vibrational energies [1, 5]. The operation of STM can be treated as an equivalent circuit consisting of a power supply and a resistor (STM junction, typical 1MΩ to 1GΩ); the resistor is of atomic dimensions, if the molecule in the STM junction moves in the form of vibration, rotation, etc, the resistance will change. Such a resistance change is reflected in the tunneling current change; however, such a small change is too small to be measured in the I-V curve. A few times a change in the dI/dV could be observed, most of time d^2I/dV^2 needs to be recorded and the junction resistance change due to the molecule motion is associated with a positive peak on the positive bias side and a negative peak on the negative bias side [1, 5].

1.2 Imaging with H_2 and CO

Even though STM can routinely achieve high spatial resolution of surfaces and image single molecules, it can also provide electronic and vibrational signatures of single molecules, STM imaging fails to resolve complex chemical structure until recently. Scanning tunneling hydrogen

`

microscopy (STHM) [6], inelastic tunneling probe (itProbe) [7] and hydrogen rotational spectromicroscopy [8, 9] achieved chemical and structural imaging of single molecules with unprecedented details. Such great-detail chemical structures have also been observed with a noncontact atomic force microscope (NC-AFM) [10].

In all these techniques, small molecules like H_2 and CO are attached to the tip or trapped in scanning probe junction, acting as a sensor of the chemical structure. In the itProbe and NC-AFM, a CO terminated tip is attached to the tip. As the tip scanned across the surface, either the shift in the resonance frequency or inelastic tunneling signal is recorded. Skeletal structure of molecule and chemical bonds can be imaged. Especially STM itProbe broadens STM's applications to study electronic properties, vibrational properties, molecular structure and chemical bonding of the same molecules combing with STM imaging, electronic spectroscopy and IETS.

Recently it has been demonstrated that by trapping H_2 in the STM junction at low temperature, the chemical structure of organic molecules can be imaged with high resolution revealing geometrical structures and intermolecular hydrogen interactions between monolayers of organic molecules, this way of imaging is called Scanning Tunneling Hydrogen Microscopy (STHM) [6]. More recently, the rotational excitations of hydrogen molecule weakly adsorbed on surfaces have been measured with the STM [11, 12]. It was also shown that similar to the vibrations of a CO molecule attached to the tip [7], changes in the adsorption potential well induced by varying the tip-sample distance shift the energies in both vibrational and rotational modes for the hydrogen temporally trapped in the tunnel junction [13]. The sensitivity of the H_2 modes to different chemical environments has been applied to achieve sub-Å structural and molecular orbital imaging of MgP on metal and oxide surfaces [8, 9].

`

1.3 Laser STM

Shortly after the invention of STM in 1982 [1], the idea of combining optical techniques with STM has been pursued [13]. One way to couple optical techniques with STM is the STM induced light emission; this technique now has achieved submolecular resolution [14]. Due to the thermal effects induced by laser and some other experimental challenges, for long time, little success has been achieved toward the combination of high spectral and temporal resolution of laser with the spatial resolution of STM [13]. Submolecular Raman spectral imaging has been achieved by coupling the Raman process to tunneling [15].

More importantly, fs laser techniques like 2 Photon Photoemission (2PPE) has achieved fs temporal resolution [16], by combining fs laser with STM, simultaneous temporal fs resolution and spatial sub-Å resolution could be achieved. However, despite the successes in spatial and spectral resolution, although lots of efforts have been spent, there is so far no clear evidence of simultaneous fs and Å resolution, achieving this great goal has been the “holy grail” in the field [17].

Besides STM induced light emission, there were also efforts in the Ho Group to achieve simultaneous fs- Å resolution [18, 19]. In these efforts, the Ti: Sapphire laser beam fundamental beams are used for the pump-probe time resolved experiments. The problem by using two fundamental beams is they will cause optical interference when the two beams spatially and temporally overlapped. One way to solve this is using two different polarization beams although the two beams will still slightly interfere [18, 19], a better way to avoid interference is by using two different color laser beams.

`

In this dissertation, efforts are spent to setup a tunable wavelength (220nm~1040nm) femtosecond laser system by using a harmonic generator to extend the wavelength from a MaiTai Deepsee laser. Different color laser beams (fundamental and 2^{nd} harmonic, fundamental and 3^{rd} harmonic) are made overlapped on the diagnostic path. However, it's hard to overlap the two color beams in the junction given there are lenses inside the UHV chamber to focus the beams and the refractive index is different for different colors and will change the beam path. The excited states of molecules are usually in the visible to the UV, another reason that the wavelength of the laser needs to be tunable in this range is in order to be able to excite the tunneling electrons into resonance with an excited state of the molecule.

To reach sub-Ångström spatial limit in optical experiments of single molecules, previous studies have been shown that it is necessary to couple light to the tunneling process [19]. The difficulty in such experiments is that the rate of production of photoinduced tunneling electrons is very low in relation to the background of bias-induced tunneling electrons in the operation of the STM. We are using a new method by detecting the electrons produced at the repetition rate of the femtosecond laser (~80 MHz), which provides an intrinsic modulation of the photon emitted or photon-induced tunneling electrons. An external bias tee was used to separate the DC and RF signal, a 50Ω terminal resistor was used as the RF current to voltage converter. The RF signal will go to the 200MHz RF lock-in (or spectrum analyzer) through the RF amplifier for detection. Further discrimination is achieved by connecting the output of 200 MHz lock-in amplifier to a second lock-in amplifier that detects a lower frequency signal generated by modulating the sample bias, for dI/dV and d^2I/dV^2 spectroscopy. To improve, a new cryogenic amplifier can be installed to get better signal/noise ratio, a fabricated plasmonic tip or nanoclusters on surface can be used for better plasmonic enhancement.

`

1.4 Summary of Contents

In the introduction, methods to extend both the spatial and temporal resolution of STM were addressed. In the remaining part of this chapter a brief summary of the following chapters is presented of the work conducted in this thesis.

Chapter 2: "A Tunable fs Laser Coupled RF-STM" describes the effort to set up the new 220 nm~1040 tunable fs laser system, including alignment, characterization and simulation on the optical table. And then this chapter describes the alignment of different color beams to the STM junction, especially the effort to align two different color beams overlap spatially and temporally in the STM junction. Lastly, this chapter describes the detection of laser induced current, including the DC rectified current and the RF current with the double lock in technique.

Chapter 3: "Imaging Molecular Orbitals of 4, 7-Di ([2, 20-bithiophen]-5-yl) benzo[c] [1, 2, 5] thiadiazole (4T-BTD) with a STM" by W. Cao, C. J. Patel, G. C. Welch, G. C. Bazan and W. Ho, prepared to submitted to *Nano Lett*. 4T-BTD is an organic molecule with intramolecular donor-acceptor-donor sites. This paper first describes the STM topography of the 4T-BTD molecule on the NiAl(110) surface, which shows bias dependence, the electron poor benzothiodiazole fragment in the acceptor site can only be clearly imaged at bias near the LUMO peak. LUMO dI/dV spectra clearly show that the center acceptor unit has higher peaks, LUMO dI/dV imaging more clearly highlights the center acceptor part. H_2 rotational IETS imaging is performed on the molecule, LUMO structure of the molecule are more clearly imaged at sub-Å resolution, which is the first time observe sub- Å details of the molecular orbital on the metal surface by using H_2.

`

Chapter 4: "Imaging Metal-Molecule Chain and Single Molecule of 1, 4-Phenylene Diisocyanide (PDI) on Noble Metal Surfaces and Their Interaction with Small Molecules" by W. Cao, C.J. Patel, M. Feng, H. Petek and W. Ho, prepared to be submitted to *Journal of Chemical Physics*. This paper first describes the chains on noble metal surfaces and the IETS of CO_2 trapped on the chain, and then focuses on the imaging of single PDI molecules. Single PDI molecules are studied on Cu (110) surface with H_2 imaging. At low H_2 coverage, while the STM topography image only shows two dimples which may be the N-C groups, the STM H_2 IETS image clearly shows the two N sites. At high H_2 coverage, the topography image already shows three parts of the molecule with interactions with the surface, the IETS image shows more details of the molecule and its interaction with the substrate, with better contrast and sharper transitions.

Chapter 5: "Exploration of New Oxide Surfaces and Study of Molecules in Various Chemical Environments" describes the STM work of molecules on oxide surfaces. Large aluminum oxide islands are formed on NiAl (110) surface by modifying previous recipes, CuO is formed on Cu (110) surface with well-defined structure. STM imaging and spectroscopy are performed on molecules (including C_{60}, azulene, alizarin and CO) adsorbed on Al_2O_3 and CuO surfaces. The thin oxide provides electronic decoupling from the underlying metal substrate that sharpens the electronic states energy width of the molecule, the oxide can also increase the lifetime of excited states of adsorbed molecules.

Chapter 6: "Imaging and Electronic Spectrum of Fe Nanoclusters on Al_2O_3/NiAl (110) at Various Temperatures with a Laser-STM" describes the imaging and electronic properties of Fe nanoclusters that are formed on Al_2O_3/NiAl (110) surface with STM. Fe clusters are formed on oxide at room temperature and 84K. Bigger Fe cluster can be formed by annealing the sample to

high temperature. Electronic properties are studied at 84K and 21K, DC and RF dI/dV spectra are also studied with 220nm fs laser in junction.

The concluding chapter (Chapter 7) summarizes the dissertation and significance. New directions for further experimental directions are proposed that should elucidate the experiments conducted in this thesis.

Appendix A includes the catalog of the STM4 laser system and describes the alignment and the key parts and homemade parts of the system. Appendix B describes the evaporator loadlock of the STM4 system and new evaporators.

`

Bibliography

1. "Single-molecule Chemistry", W. Ho, *J. Chem. Phys.* **117**, 11033-11061 (2003).
2. "Surface Studies by Scanning Tunneling Microscopy", G. Binning. H. Rohrer, Ch. Gerber, and E. Weibel, *Phys. Rev. Lett.* **49**, 57-61 (1982).
3. "Introduction to Scanning Tunneling Microscopy", C. J. Chen, Oxford University Press, Oxford 2008.
4. "Theory and Application for the Scanning Tunneling Microscope", J. Tersoff, D. R. Hamann, *Phys. Rev. Lett.* **50**, 1998-2001 (1983).
5. "Single Molecule Vibrational Spectroscopy and Microscopy", B. C. Stipe, M. A. Rezaei, W. Ho, *Science* **262**, 218-220(1998).
6. "Direct Imaging of Intermolecular Bonds in Scanning Tunneling Microscopy", C. Weiss, C. Wagner, R. Temirov, and F. S. Tautz, *J. Am. Chem. Soc.* **132**, 11864 (2010).
7. "Real-Space Imaging of Molecular Structure and Chemical Bonding by Single-Molecule Inelastic Tunneling Probe", C. L. Chiang, C. Xu, Z. Han and W. Ho, *Science* **344**, 885-888(2014).
8. "Rotational Spectromicroscopy: Imaging the Orbital Interaction between Molecular Hydrogen and an Adsorbed Molecule", S. Li, D. Yuan, A. Yu, G. Czap, R. Wu and W. Ho, *Phys. Rev. Lett.* **114**, 206101 (2015).
9. "Single-Molecule Rotational and Vibrational Spectroscopy and Microscopy with the Scanning Tunneling Microscope", A. Yu, S. Li, G. Czap and W. Ho, *J. Phys. Chem. C*, **119**, 14737-14741 (2015).
10. "The Chemical Structure of a Molecule Resolved by Atomic Force Microscopy", L. Gross, F. Mohn, N. Moll, P. Liljeroth and G. Meyer, *Science* **325**, 1110-1114(2009).

`

11. “Rotational and Vibrational Excitations of a Hydrogen Molecule Trapped within a Nanocavity of Tunable Dimension”, S. Li, A. Yu, F. Toledo, Z. Han, H. Wang, H. Y. He, R. Wu and W. Ho, *Phys. Rev. Lett.* **111**, 146102 (2013).
12. “Distinction of Nuclear Spin States with the Scanning Tunneling Microscope”, F. D. Natterer, F. Patthey and H. Brune, *Phys. Rev. Lett.* **111**, 175303 (2013).
13. “Photoassisted Scanning Tunneling Microscopy”, S.Grafström, *J. Appl. Phys.* **91**, 1717-1753 (2002).
14. “Viewing the Interior of a Single Molecule: Vibronically Resolved Photon Imaging at Submolecular Resolution”, C. Chen, P. Chu, C. A. Bobisch, D. L. Mills, and W. Ho, *Phys. Rev. Lett.* **105**, 217402 (2010).
15. “Chemical Mapping of a Single Molecule by Plasmon-Enhanced Raman Scattering”, R. Zhang, Y. Zhang, Z. C. Dong, S. Jiang, C. Zhang, L. G. Chen, L. Zhang, Y. Liao, J. Aizpurua, Y. Luo, J. L. Yang, J. G. Hou, *Nature* **498**, 82–86 (2013).
16. “Femtosecond Time-Resolved Two-Photon Photoemission Studies of Electron Dynamics in Metals”, H. Petek and S. Ogawa, *Prog. Surf. Sci.* **56**, 239-310(1997), and private communication with H. Petek and M. Wolf.
17. “Single-Molecule Femtochemistry: Molecular Imaging at the Space-Time Limit”, H. Petek, *ACS Nano.* **8**, 5-13(2014).
18. “Observation of Coherent Electron Excitation and Electron-Phonon Scattering at Metal Surfaces”, Y.-M. Chang, L.J. Lauhon, and W. Ho, to be published.
19. “Two-Photon-Induced Hot-Electron Transfer to a Single Molecule in a Scanning Tunneling Microscope”, S. W. Wu and W. Ho, *Phys. Rev. B.* **82**, 085444 (2010).

`

Chapter 2

A Tunable fs Laser Coupled RF-STM

2.1 Introduction/Overview

Shortly after the invention of STM in 1982 [1], the idea of combining optical techniques with STM has been pursued [2]. One way to couple optical techniques with STM is the STM induced light emission [3]; this technique now has achieved submolecular resolution [4]. Due to the thermal effects induced by laser and some other experimental challenges, for long time, little success has been achieved toward the combination of high spectral and temporal resolution of laser with the spatial resolution of STM [2]. Submolecular Raman spectral imaging has been achieved by coupling the Raman process to tunneling [5]. Regarding temporal resolution, although lots of efforts have been spent, there is so far no clear evidence of simultaneous fs and Å resolution [6-15].

In the Ho group, the first STM built in 1998 was to study photo dissociation of O2 molecules on Pt [6]. Later the group pushed STM induced light emission to submolecular resolution [4]. There were also efforts to achieve simultaneous fs- Å resolution [7, 8]. In this thesis, a tunable femtosecond laser was assembled; different colors of laser beams are aligned to overlap temporally and spatially; photoemission current is detected in the STM junction with a RF-STM.

`

2.2 STM4 Laser System Setup

In order to have the femtosecond laser interacting resonantly with the single molecule, the wavelength of the laser needs to be tunable in order to be able to excite the tunneling electrons into resonance with an excited state of the molecule. Since excited states are usually in the visible to the UV, we have coupled the near-IR output of the Mai Tai Deepsee Ti:sapphire laser to nonlinear crystals in Photop Harmonic Generator to generate second, third, and fourth harmonics, thus achieving continuous tunable femtosecond light output from 1040 nm down to 210 nm, with a gap between 520 and 690 nm. A delay stage and several other linear optical stages are used to get the temporal and spatial overlap of fundamental-fundamental, fundamental-2^{nd} harmonic and fundamental-3^{rd} harmonic. A BEOC-LPC is used to stabilize the laser power.

Fig2.1 is a diagram of the STM4 laser system, Fig2.2 is a photo of the STM 4 laser table, the inset shows the diagnostic path, Fig2.3 shows the powers at different wavelengths; all parts are listed in Appendix of this dissertation. As shown in fig2.1 and fig2.2, after the laser beam comes out from the Mai Tai, a periscope is used to change the beam polarization from horizontal to vertical, then a mirror pair is used to steer the beam into the LPC. Since the diameter of the incoming beam is required to be smaller than 4mm for the LPC to stabilize laser power, a lens pair is used to slightly reduce the beam size. After the LPC, a 30/70 beam splitter is used the divide the laser power, ~30% of the beam will go through the fundamental path and 70% of the beam will go into the harmonic generator to generate 2^{nd}, 3^{rd} and 4^{th} harmonics.

On the fundamental path, three mirrors are used to steer the beam into a Michelson Interferometer, a 50/50 beam splitter is used to get the same power of the two arms. One arm is a

`

Newport UBBR1-1S retroreflector mounted on a homemade piezo shake attached to a Newport UTS100CC delay stage, ensuring parallel of the outgoing beam to the incoming beam; the other arm is a mirror pair sits on a plate attached to a 3-direction stage. For the fundamental pump-probe experiments, we need both arms of fundamental beam. For the time resolved experiments using two different colors (like 2PPE), we only need the retroreflector-shaker-delay stage fundamental beam. Different from the former STM2 laser system setup, we have the delay stage and shaker in the same arm. The reason is that we need both fundamental+2^{nd} and fundamental+3^{rd} for time resolved experiments, thus not convenient to put either the delay stage or shaker on one of the 2^{nd} or 3^{rd} harmonic paths.

70% of the fundamental power goes into the harmonic generator to generate 2^{nd}, 3^{rd} and 4^{th} harmonics. The horizontal-polarized 2^{nd} harmonic is generated through second harmonic generation (SHG) by focusing the vertical-polarized fundamental beam through a 2^{nd} harmonic BBO crystal; since we need vertical beam (polarized along the tip direction) to couple with STM to get maximum photon-induced signal, we use two periscopes to change the polarization, the 1^{st} periscope changes the beam height to 3 inches and the 2^{nd} periscope change the polarization (to vertical) and change the height back. From the beam splitter to the dichroic mirror (d1) which combines the fundamental and 2^{nd} harmonic, we need to make sure the travel distance is the same so they can temporally overlap; first we need to roughly measure the distance, then we uses linear stages for fine adjustments. The vertical-polarized 3^{rd} harmonic is generated through sum frequency generation (SFG) by focusing the horizontal polarized fundamental and 2^{nd} harmonic beams through the 3^{rd} harmonic BBO crystal, a wave plate is used to rotate the fundamental beam while keep the 2^{nd} harmonic beam horizontal. The 3^{rd} harmonic beam also travels the same distance as the fundamental to get the temporal overlap; same as 2^{nd} harmonic path, a linear stage

`

is used to do fine adjustment. The vertical polarized 4^{th} harmonic is generated through a SHG process by focusing 2^{nd} harmonic beam through a 4^{th} harmonic crystal, the 4^{th} harmonic travels shorter than the other 3 beams since 4^{th} harmonic is used only for one-photon photoemission experiments. The diameter of the harmonic beams is too big so we used a lens pair in each path to reduce the beam size.

2.3. Characterization and Simulation on the Optical Table

With the development of ultrafast lasers, different lab techniques, most notably the time-resolved two photon photoemission (2PPE) have been successfully studied the ultrafast charge carrier dynamics [15, 16]. However, 2PPE and other time-resolved techniques do not have the spatial resolution to study single molecules and atoms. Thus, combining laser techniques like 2PPE with STM could achieve the simultaneous temporal and spatial resolution in principle to study the ultrafast dynamics at single molecule level.

Before shining the laser beams into the junction, the beams can be characterized on the optical table. Especially for the pump probe experiments; it's desirable to make sure the beams overlap spatially and temporally before shining into the junction. A flip mirror mount is used to direct the beam to the diagnostic path; the distance between the flip mirror mount and the nonlinear crystal on the optical path is about the same as the distance from the distance between the flip mirror mount and the STM junction. A 3.38" fused silica viewport and two fused silica windows are used to simulate the path to the STM junction. Same fused silica lens is used to focus the beam to the non-linear crystal.

After the 2 arms of fundamental beams combine on the dichroic mirror of the Michelson Interferometer, they travel to the chamber to shine into the STM junction; we flip m30 on the

`

optical path to direct the beams towards the diagnostic path to characterize he beam. The same 3" focal length lens is used to focus down the beams at the BBO crystal, which is mounted on the 3-direction linear stage for fine adjustments. 2^{nd} harmonic beam (usually with green color) is generated through the BBO crystal, a color filter is used to filter out the fundamental residual. When the 2 arms of beams are spatially and temporally overlapped, we could see the fundamental beam blinking; the blinking of the 2^{nd} harmonic after the BBO crystal is much more obvious. To quantitatively characterize the beam, a photodiode (from Thorlabs) is used to covert the 2^{nd} harmonic laser signal to current, then voltage signal is obtained after the current goes through a terminal resistor (with different resistances, also from Thorlabs). The voltage signal can be fed into an oscilloscope or a DAQ, a LabVIEW program is used to record the voltage signal as the delay stage moves. An example of the autocorrelation data is shown in fig6; as could be seen on the top figure, if the polarization of both beams is vertical to the table, there will be significant interference. Such interference will cause tip crash in the tunneling regime even with very small laser power, however, photons need to couple with tunneling process to study the ultrafast dynamics at the single molecule level [7, 8]. One way to minimize the interference is to use one vertical polarized beam and one horizontal polarized beam (to optical table); the horizontal beam is got by using a waveplate and a polarizer (fig6). The interference gets much smaller, though there is still some especially around time zero.

Another better way to minimize the interference is to use different wavelength of laser beams. We can use fundamental and 2^{nd} harmonic or fundamental and 3^{rd} harmonic. Similar to fundamental-fundamental, we use the same fused silica lens to focus the beams down on a different nonlinear crystal. The orientation of the nonlinear crystal will be quite different from using 2^{nd} harmonic to 3^{rd} harmonic. 3^{rd} harmonic beam is generated by focusing the fundamental

`

and 2nd harmonic beam on the nonlinear crystal (“2+1”); we use a Schott glass filter to filter fundamental and 2nd harmonic residual before the beam reaches the photodiode. 2nd harmonic beam is generated by focusing the fundamental and 3rd harmonic on the nonlinear crystal (“3-1”); the same Chroma filter for fundamental overlap is used to filter fundamental and 3rd harmonic before the beam reaches the photodiode. The 2nd harmonic and 3rd harmonic are weaker than the fundamental; sometimes a CCD camera is needed to detect the even weaker beam after the nonlinear crystal and filter.

2.4. Alignment of Laser Beams into STM Junction

After characterization on the optical table, the laser beams are ready to shine into the junction. To align the laser to the junction, a pair of plano-convex lenses was mounted on two separate translation-and-tilt stages inside the UHV chamber. The laser incident and exit angles are 45° from the surface normal. One of the lenses was used to focus the laser into the junction; the other was used to image the STM junction onto a CMOS or CCD camera. When the laser was aligned to the junction, the STM tip was shown on the bottom in and its mirror image appeared on the top due to the high reflectivity of the sample. The focal spot in the junction was estimated to be around 50 μm in diameter. The laser electric field was linearly polarized in the plane of incidence (p polarized) to maximize the laser-induced signal [17]; except for changing polarization of one arm of fundamental to minimize the interference when 2 fundamental beams are used. Fig2.7 (B) is a CMOS tip-mirror image with the fundamental in the junction while fig2.7(C) is a CMOS tip-mirror image with the 4th harmonic in the junction, both were taken on the laser outgoing side.

`

To set up the new system, the initial alignment to the junction could be very tricky. First tip-mirror image should be clearly seen on the bottom mirrors of the periscope on both the beam incoming and outgoing side by shining white night from the 8" front window, and the image should be focused and in the center of view , it also depends on which angle we view from (fig2.8 A). Then the tip-mirror image could be got on a CCD/CMOS at the laser outgoing side, but due to the 2D nature of our two lens system, even when the beam seems at the junction as shown in fig2.7 (B) and (C), it may hit somewhere on the sample and then reflects out (eg, point e in fig2.9A). We can see the sample from the pyrometer viewport with the help of a finder scope, the CMOS tip-mirror image got from here is 3D, and when the beam seems at the junction on the image, it is actually in the junction. Since no commercial finder scope can see 3^{rd} or 4^{th} harmonic (220nm~330nm), a homemade finder scope made of fused silica lenses was assembled to help seeing the UV beams from the pyro viewport (fig2.8 D).

If the two p-polarized fundamental is in the junction or along the tip mirror axis, we can clearly see the STM Z feedback voltage oscillation, both in and out of tunneling regime due to the interference (fig2.9), multiphoton current can also be detected, as shown in fig2.10 A. Even if the polarization of the fundamental beams is different, we can still clearly see more multiphoton signals around time 0 if the two arms of fundamental overlap on the tip-mirror axis.

Although we can easily and reproducibly overlap two fundamental beams temporally and spatially in the STM tip-sample junction; it is very hard for us to align two different colors (fundamental + 2^{nd} harmonic "1+2" or fundamental+3^{rd} harmonic "1+3") to the junction. The main reason is that we have a lens in the UHV chamber to focus the laser beam to the STM junction (fig2.7A); the refractive index for different wavelengths is different and it will change the beam overlap unless the beams hit the center of the lens. The beam path is very hard to check

or simulate given that the lens is in UHV chamber. It's also hard to overlap the 2 different color beams with CCD/CMOS from the laser outgoing viewport or pyro viewport, given that the lens of the finder scope will change the overlap. For the 2PPE setup, a curved mirror outside the UHV chamber is used to focus the beam on the sample, so as long as the 2 beams overlap on the diagnostic path, they overlap on the sample in the UHV chamber [15, 16]. 2PPE also has the hemispherical energy analyzer to collect the photoemitted electrons [15, 16]; it's probably more sensitive than the STM tip/sample to collect electrons.

2.5. Laser Induced Current Detection

To reach sub-Ångström spatial limit in optical experiments of single molecules, previous studies have been shown that it is necessary to couple light to the tunneling process [8]. The difficulty in such experiments is that the rate of production of photoinduced tunneling electrons is very low in relation to the background of bias-induced tunneling electrons in the operation of the STM. One way to detect the laser-induced current is through the DC rectified current. The multiphoton current shown in figure.10 is the DC current amplified by the DC preamplifier used for DC bias induced tunneling current, such current could not be detected in the tunneling regime given that certain laser power is needed to detect the current, and such a laser power will make the tunneling junction unstable.

We are using a new method by detecting the electrons produced at the repetition rate of the femtosecond laser (~80 MHz), which provides an intrinsic modulation of the photon emitted or photon-induced tunneling electrons (fig2.11). We were using an external bias tee to separate the DC and RF signal, a 50Ω terminal resistor was used as the RF current to voltage converter. The RF signal will go to the 200MHz RF lock-in (or spectrum analyzer) through the RF amplifier for detection. Fig2.12 shows the power spectrum with 220nm in the STM junction of

`

Ag tip and Cu (110) surface. The 79.7MHz peak is at the repetition rate of the Mai Tai Deepsee laser, illustrating the feasibility of detecting the electron signal created by each laser pulse by lock-in detection at the repetition rate of the oscillator. Further discrimination is achieved by connecting the output of 200 MHz lock-in amplifier to a second lock-in amplifier that detects a lower frequency signal generated by modulating the sample bias, for dI/dV and d^2I/dV^2 spectroscopy. This double lock-in approach is shown in Figure 2.11 (A), the RF current and dI_{RF}/dV detected is shown in fig2.13. However, these measurements are performed with tip retracted. While the bandwidth of the terminal resistor is essentially infinite, the gain is greatly compromised, making it not sensitive enough to go to tunneling to get detectable laser-induced RF or DC signal.

To improve, a new cryogenic amplifier can be installed to get better signal/noise ratio, a fabricated tip can be used for better plasmonic enhancement. We can also use two different color beams for pump-probe. Schematic layout of the 80 MHz Laser-STM showing the detection of the 80 MHz component of the dI/dV and d^2I/dV^2 signals due to changes in the STM junction induced by time delayed pulse pairs.

2.6 Conclusions

A tunable fs laser (210nm~1040nm with a gap from 520nm~690nm) system has been set up by using a Mai Tai Deepsse laser (690~1040nm, ~100fs) and a Photop Haramonic Generator to generate 2^{nd} 3^{rd} and 4^{th} harmonics. 4^{th} harmonic (~220nm) can be used in 1-photon photoemission and deep UV laser-induced chemistry. The fundamental, 2^{nd} harmonic and 3^{rd} harmonic can be used for plasmon enhanced chemistry and time-resolved studies. Fundamental and fundamental ("1+1"), fundamental and 2^{nd} harmonic ("1+2"), fundamental and 3^{rd} harmonic

`

("1+3") are temporally and spatially overlapped on the optical table diagnostic path. Fundamental and fundamental can be reproducibly aligned to overlap in the STM junction although causing significant optical interference. Fundamental and 2^{nd}, fundamental and 3^{rd} could not be reproducibly aligned into the STM junction due to the lens inside the UHV chamber. The laser-induced signal is still too noisy even the double lock-in technique is used to detect the weak laser-induced signal in the tunneling regime. To improve the signal to noise ratio, a cryogenic amplifier can be used. A fabricated Ag, Au or Cu tip can also be used to improve the plasmonic enhancement.

Acknowledgements

This work is supported by the National Science Foundation Center for Chemical Innovation at the Space-Time Limit (CaSTL) under Grant No. CHE-0802913.

`

Fig2.1. STM 4 fs laser system layout (m stands for mirror, d stands for dichroic mirror, TS stands for translational stage, LPC stands for laser power controller; for a complete list of parts, refer to A.1 catalog of Appendix A in this dissertation).

`

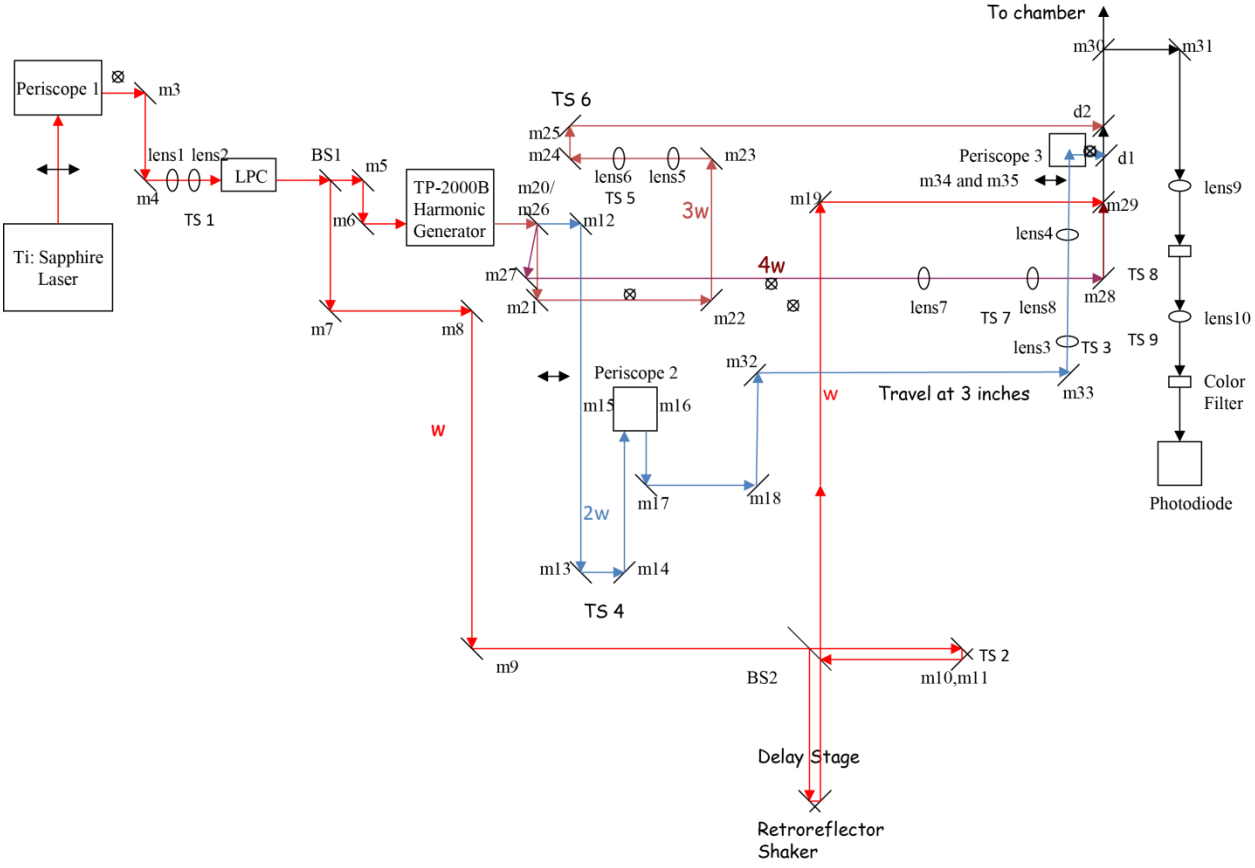
To chamber
m30
m31
Periscope 1
m3
TS 6
m25
m24
lens6
lens5
m23
d2
Periscope 3
d1
lens1
lens2
LPC
BS1
m5
TP-2000B
Harmonic
Generator
m20/
m26
TS 5
3w
m34 and m35
lens9
m4
TS 1
m6
m12
m19
m29
lens4
Ti: Sapphire
Laser
m27
4w
TS 8
m21
m22
lens7
lens8
TS 7
m28
lens10
m7
m8
lens3
TS 3
TS 9
Periscope 2
m32
m15
m16
w
Travel at 3 inches
m33
Color
Filter
w
m17
m18
2w
Photodiode
m13
m14
TS 4
m9
BS2
TS 2
m10,m11
Delay Stage
Retroreflector
Shaker

`

Fig2.2. Photo of the STM4 laser system layout, (A) photo of the whole laser system, with the key parts labeled, (B) the diagnostic path.

`

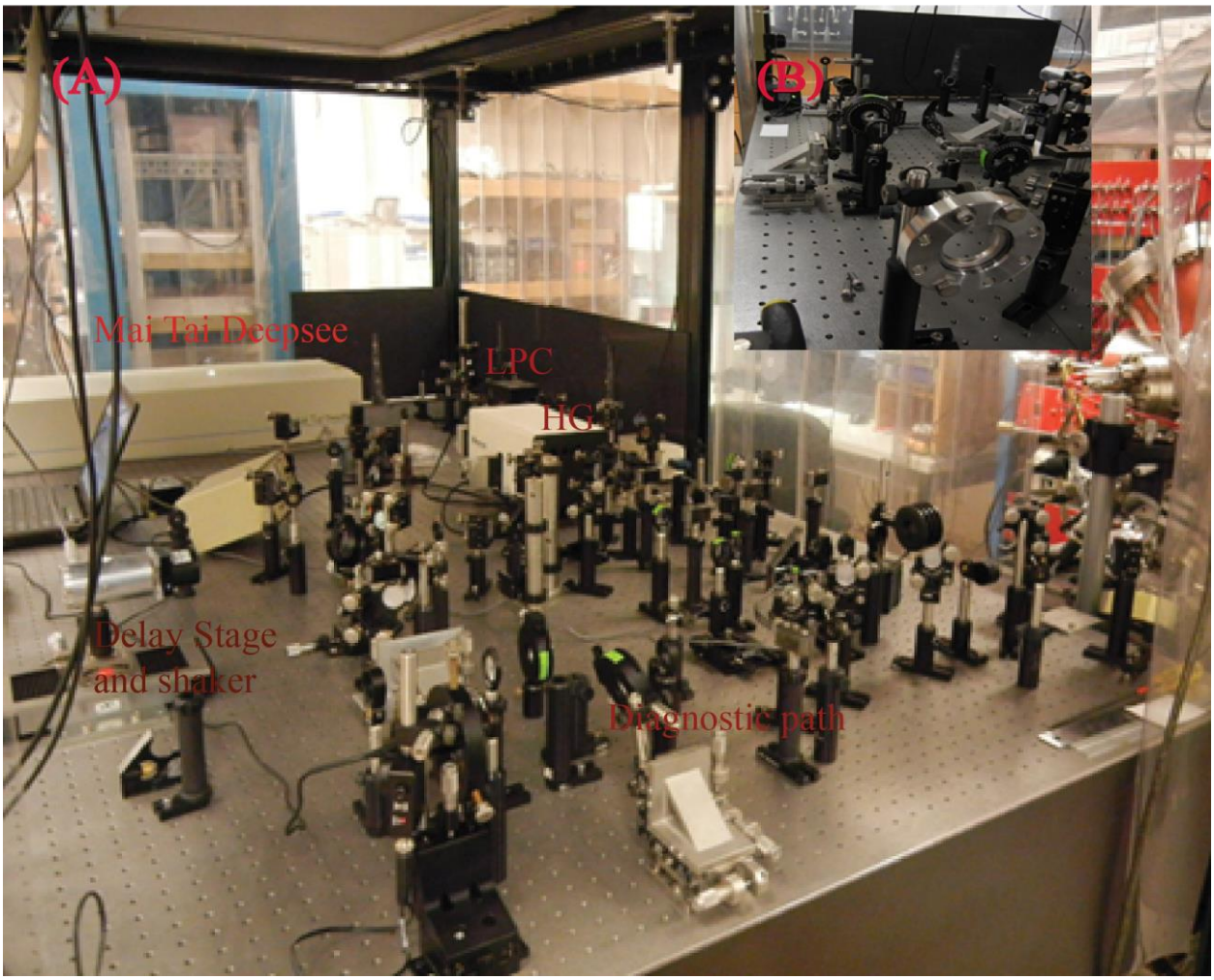
(A)
(B)
Mai Tai Deepsee
LPC
HG
Delay Stage
and shaker
Diagnostic path

`

Fig2.3. STM 4 fs laser power spectrum

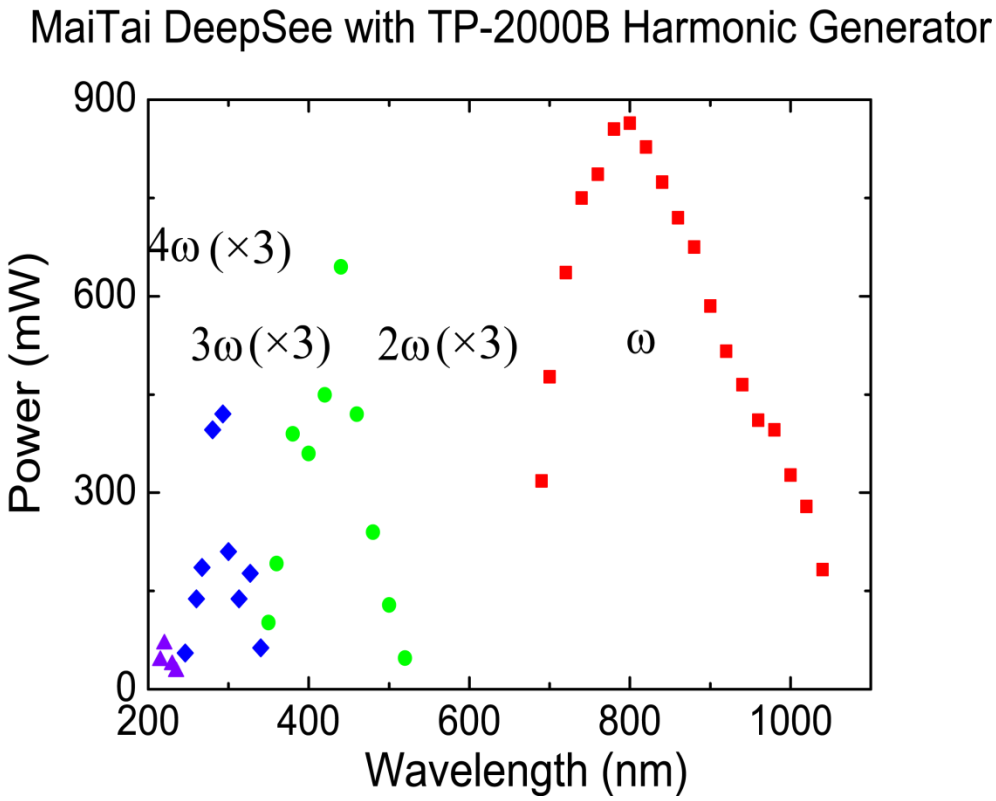
MaiTai DeepSee with TP-2000B Harmonic Generator
Power (mW)
Wavelength (nm)
900
600
300
0
200
400
600
800
1000
4ω (×3)
3ω (×3)
2ω (×3)
ω

`

Fig2.4. autocorrelation data obtained on the diagnostic path, the laser wavelength is 800nm. (A) without wave plate or polarizer, (B) with wave plate and polarizer, so the polarization of the two fundamental beams is 90 degrees away and the interference is minimum.

(A)

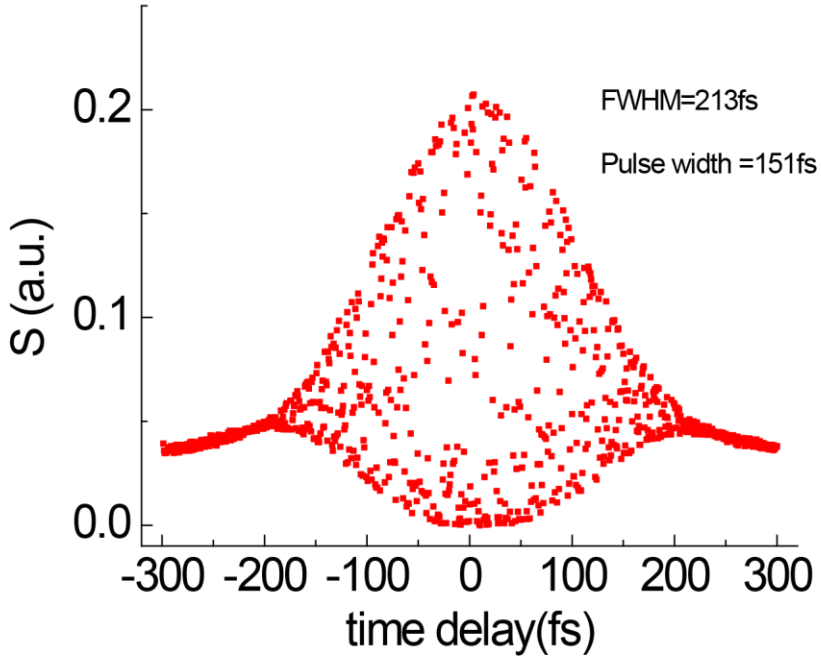
FWHM=213fs
Pulse width =151fs
S (a.u.)
0.0
0.1
0.2
-300 -200 -100 0 100 200 300
time delay(fs)

(B)

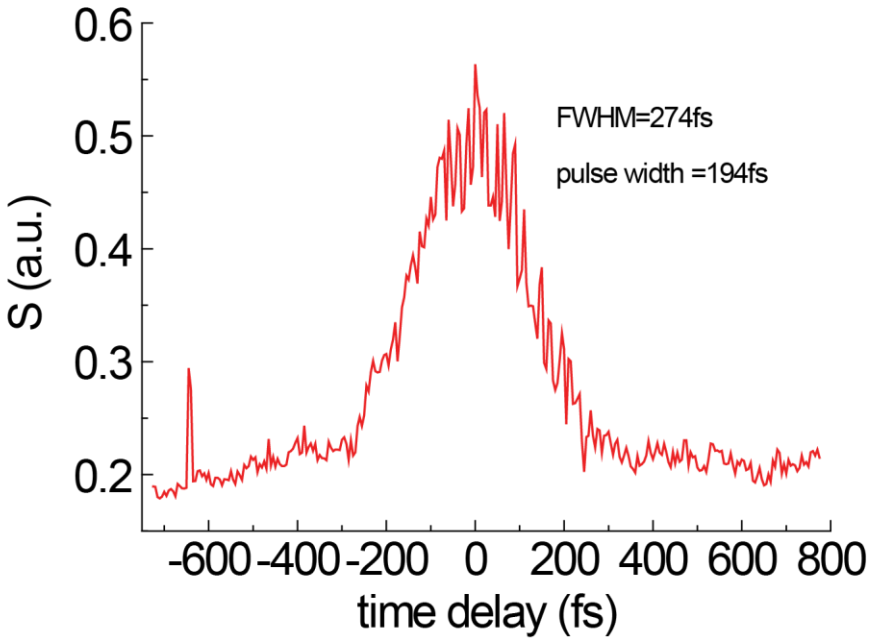
FWHM=274fs
pulse width =194fs
S (a.u.)
0.2
0.3
0.4
0.5
0.6
-600 -400 -200 0 200 400 600 800
time delay (fs)

`

Fig2.5. “1+2”autocorrelation data obtained of on the diagnostic path, the fundamental is 840nm and the 2nd harmonic is 420nm.

(A)

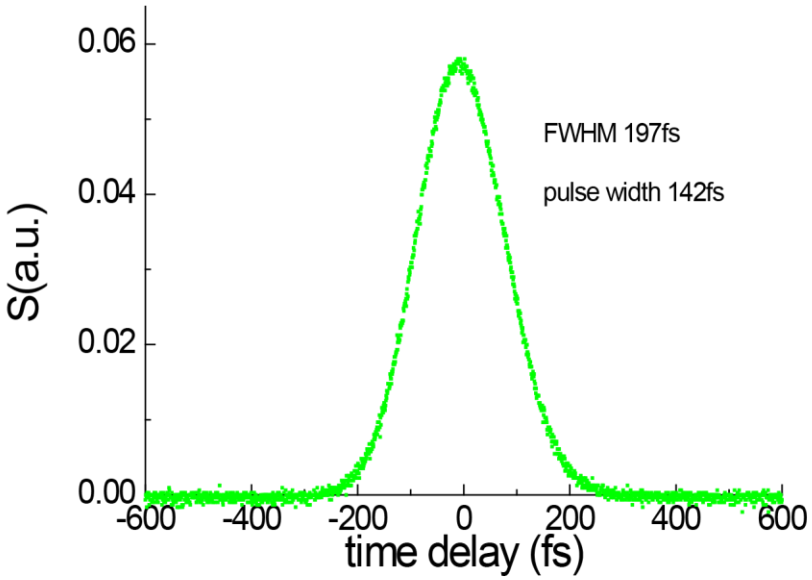
0.06
0.04
0.02
0.00
S(a.u.)
FWHM 197fs
pulse width 142fs
-600
-400
-200
0
200
400
600
time delay (fs)

(B)

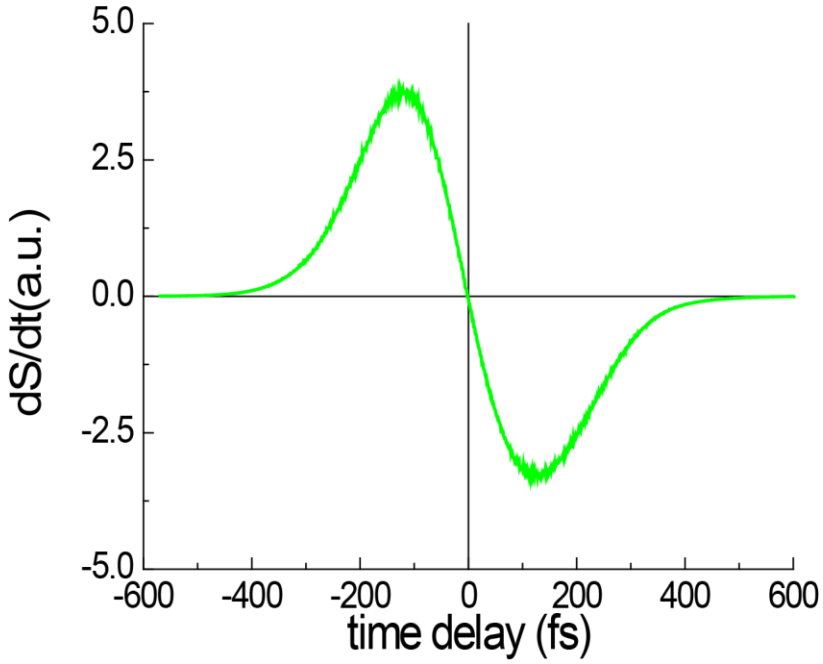
5.0
2.5
0.0
-2.5
-5.0
dS/dt(a.u.)
-600
-400
-200
0
200
400
600
time delay (fs)

`

Fig2.6. “3-1”autocorrelation data obtained of on the diagnostic path, the fundamental is 840nm and the 3rd harmonic is 280nm.

`

(A)

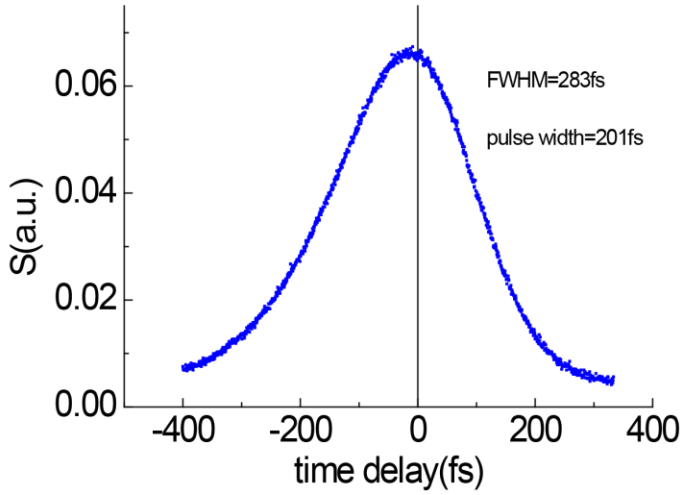
FWHM=283fs
pulse width=201fs
S(a.u.)
0.00
0.02
0.04
0.06
-400
-200
0
200
400
time delay(fs)

(B)

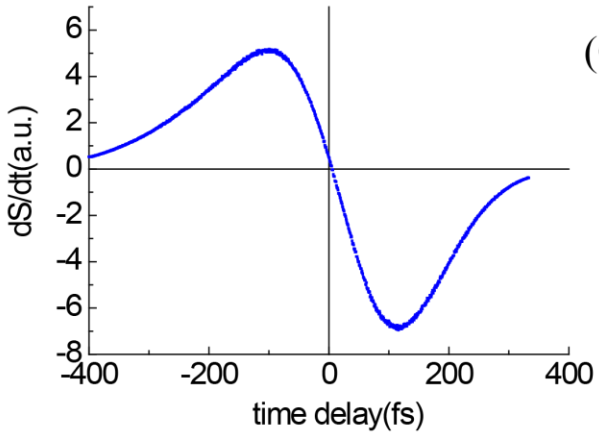
dS/dt(a.u.)
6
4
2
0
-2
-4
-6
-8
-400
-200
0
200
400
time delay(fs)

(C)

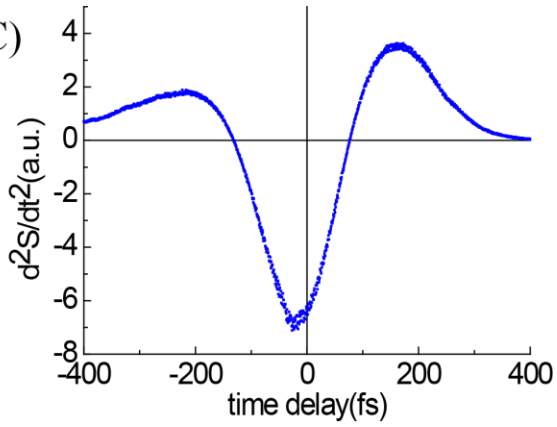
d2S/dt2(a.u.)
4
2
0
-2
-4
-6
-8
-400
-200
0
200
400
time delay(fs)

`

Fig2.7. (A) optical path through the STM junction, (B) CMOS camera tip mirror image from outgoing viewport with the fundamental (780nm) shining into the junction, (C) CMOS camera tip mirror image from outgoing viewport with the 4^{th} harmonic (220nm) shining into the junction

`

(A)

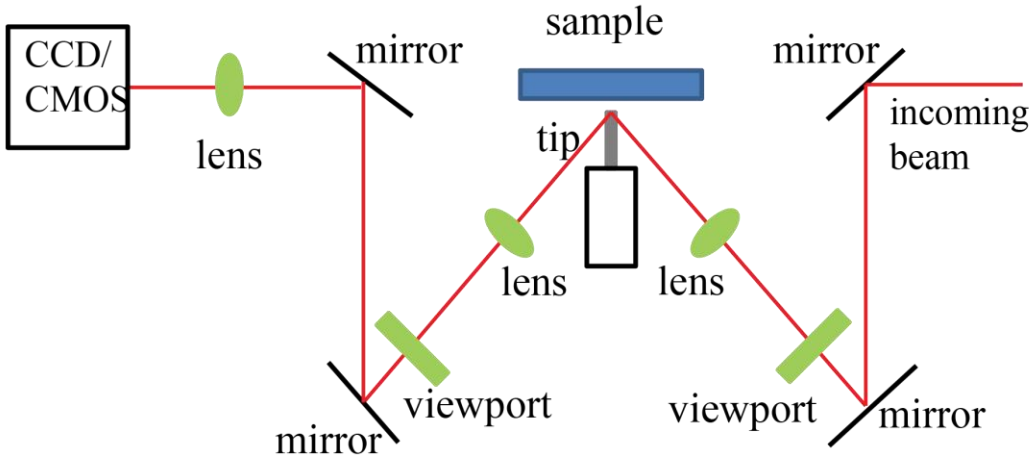
CCD/
CMOS
lens
mirror
sample
tip
lens
lens
mirror
incoming
beam
viewport
mirror
viewport
mirror

(B)

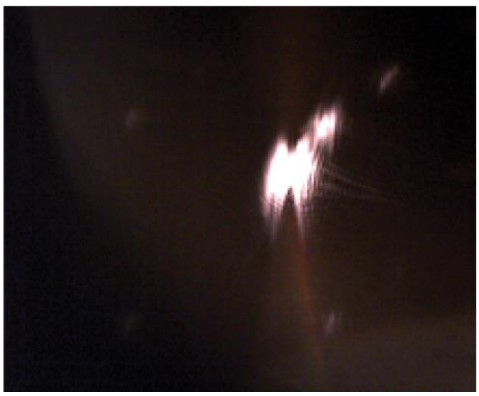

(C)

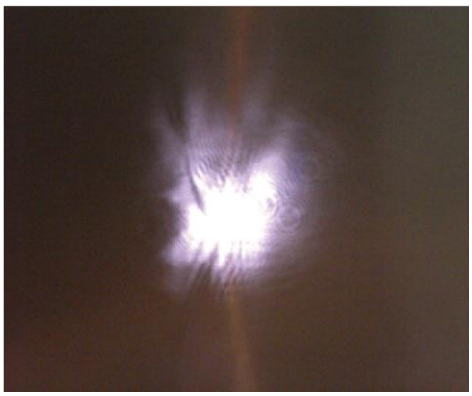

`

Fig2.8. (A) tip-mirror image on the bottom mirror of the periscope, (B) sample and tip from pyro viewport, (C) tip mirror image from pyro viewport with the CMOS camera, the beam is 2^{nd} harmonic 420nm, (D) homemade finderscope made of fused silica lens to see 3^{rd} and 4^{th} harmonic beams in junction.

`

(A)

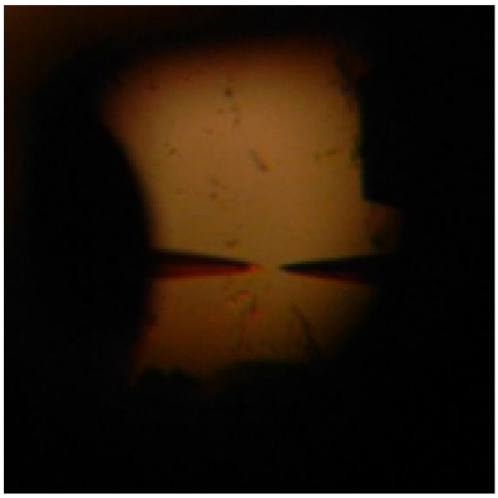

(B)

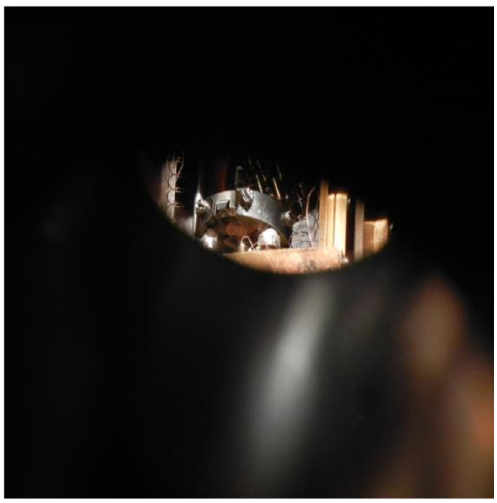

(C)

(D)

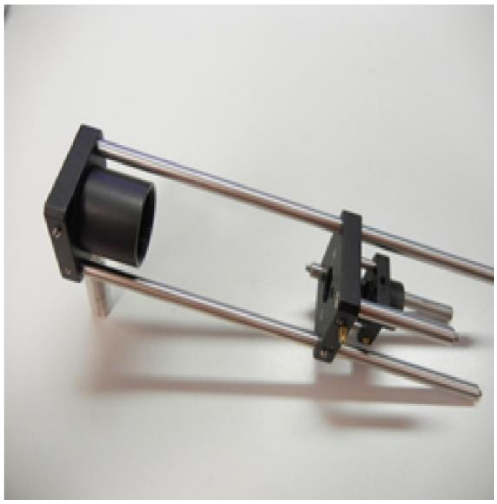

`

Fig2.9. (A), different beam position around the junction, Z-oscillation or multiphoton current can be detected when the beam is along the tip-mirror axis (eg, a, b and c), the oscillation or current won’t be detected when the beam hit other place (eg, c and d); (B) Z oscillation out of tunneling, (C) Z oscillation when tunneling.

`

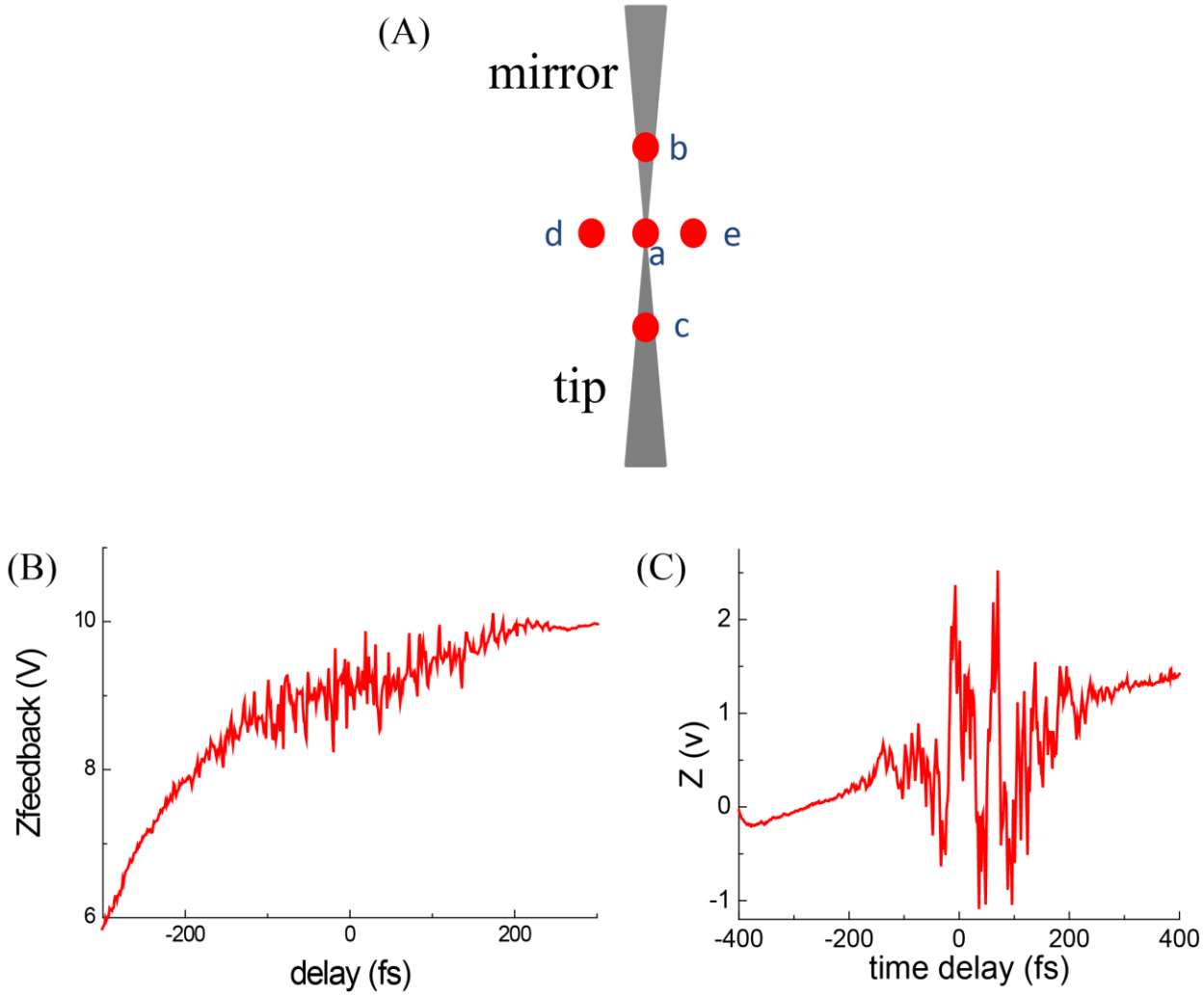
(A)
mirror
b
d
a
e
c
tip
(B)
Zfeedback (V)
10
8
6
-200
0
200
delay (fs)
(C)
Z (v)
2
1
0
-1
-400
-200
0
200
400
time delay (fs)

`

Fig2.10. (A)multiphoton current detected in the STM junction, 2 fundamental beams are both p-polarzied, (B) multiphoton current detected in the STM junction, one fundamental beam is p-polarized the other one is s-polarized.

(A)

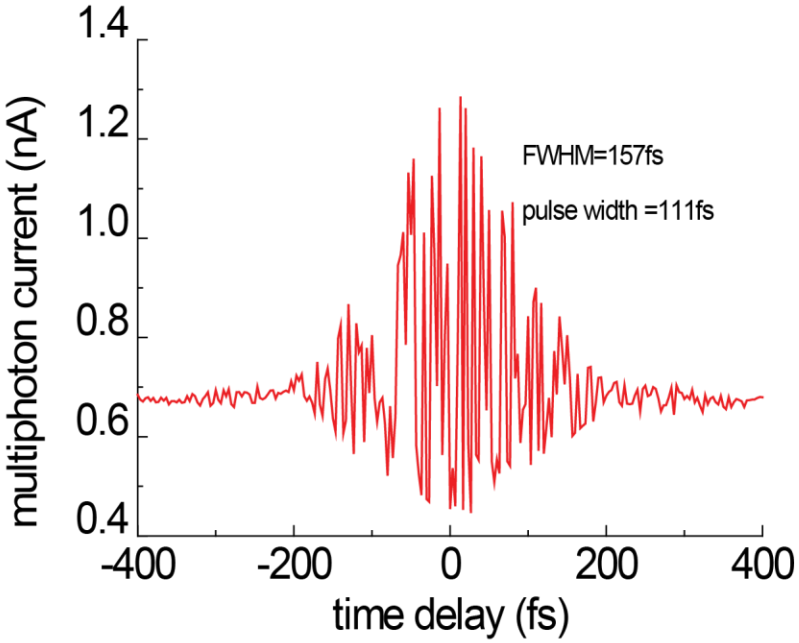
1.4
1.2
1.0
0.8
0.6
0.4
multiphoton current (nA)
FWHM=157fs
pulse width =111fs
-400
-200
0
200
400
time delay (fs)

(B)

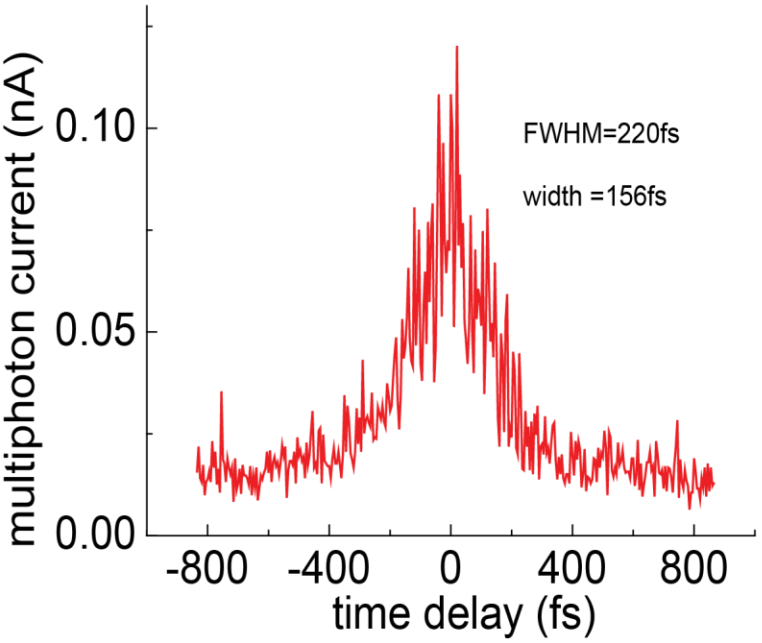
0.10
0.05
0.00
multiphoton current (nA)
FWHM=220fs
width =156fs
-800
-400
0
400
800
time delay (fs)

`

Fig2.11 (A) Schematic of experimental arrangement combining a tunable femtosecond laser system with a low temperature RF-STM, The uniqueness of the instrument lies in the lock-in detection of laser induced current due to each laser pulse of a repetitive pulse train at 80 MHz, Laser induced RF current was detected with a bias tee and terminal resistor; (B) laser induced RF current detection with a UHV low temperature ~80MHz amplifier with Q=100 and sensitivity of 20,000V/A.

(A)

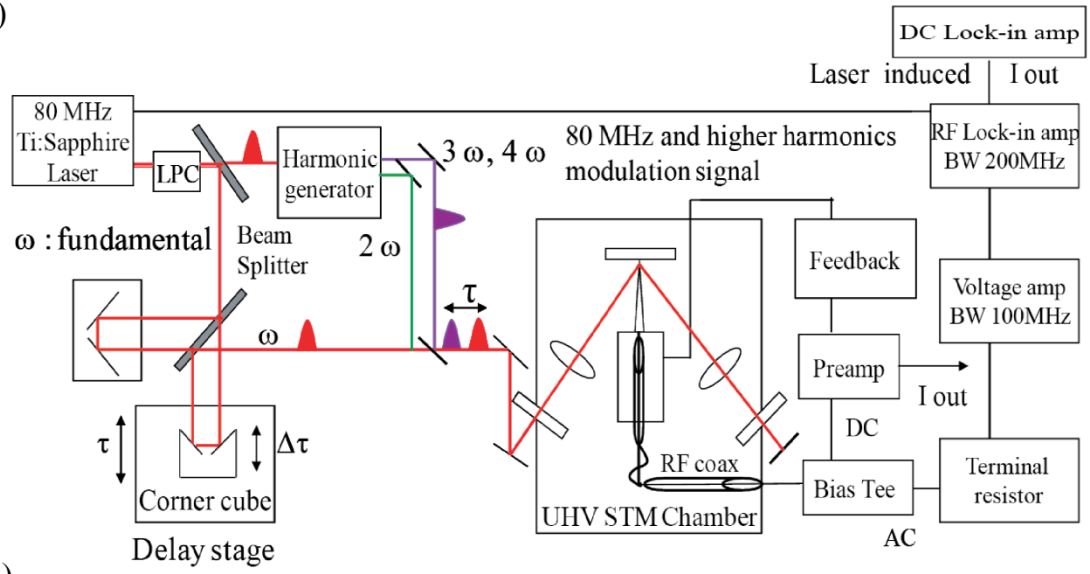
DC Lock-in amp
Laser induced
I out
80 MHz
Ti:Sapphire
Laser
LPC
Harmonic
generator
3 ω, 4 ω
80 MHz and higher harmonics
modulation signal
RF Lock-in amp
BW 200MHz
ω : fundamental
Beam
Splitter
2 ω
τ
ω
Feedback
Voltage amp
BW 100MHz
Preamp
I out
DC
τ
Δτ
Corner cube
Delay stage
RF coax
Bias Tee
Terminal
resistor
UHV STM Chamber
AC

(B)

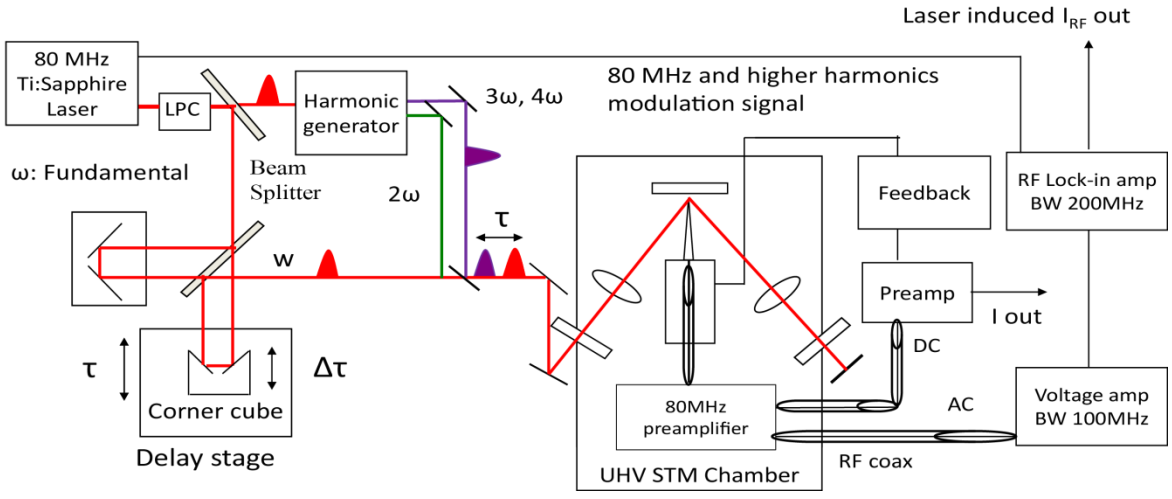
Laser induced I_{RF} out
80 MHz
Ti:Sapphire
Laser
LPC
Harmonic
generator
3ω, 4ω
80 MHz and higher harmonics
modulation signal
ω: Fundamental
Beam
Splitter
2ω
τ
w
Feedback
RF Lock-in amp
BW 200MHz
Preamp
I out
DC
τ
Δτ
Corner cube
Delay stage
80MHz
preamplifier
AC
Voltage amp
BW 100MHz
UHV STM Chamber
RF coax

`

Fig2.12 (A) Noise spectrum with the center frequency set at 79.5 MHz of the spectrum analyzer. Spectrum obtained by blocking the femtosecond laser. (B) Power spectrum of the photoemitted electron signal induced by 230 nm femtosecond laser irradiating the junction. The peak of photoemitted electron pulses are seen at 79.7 MHz, with the spectrum analyzer's center frequency set to this frequency, the repetition rate of the femtosecond oscillator.

`

(A)

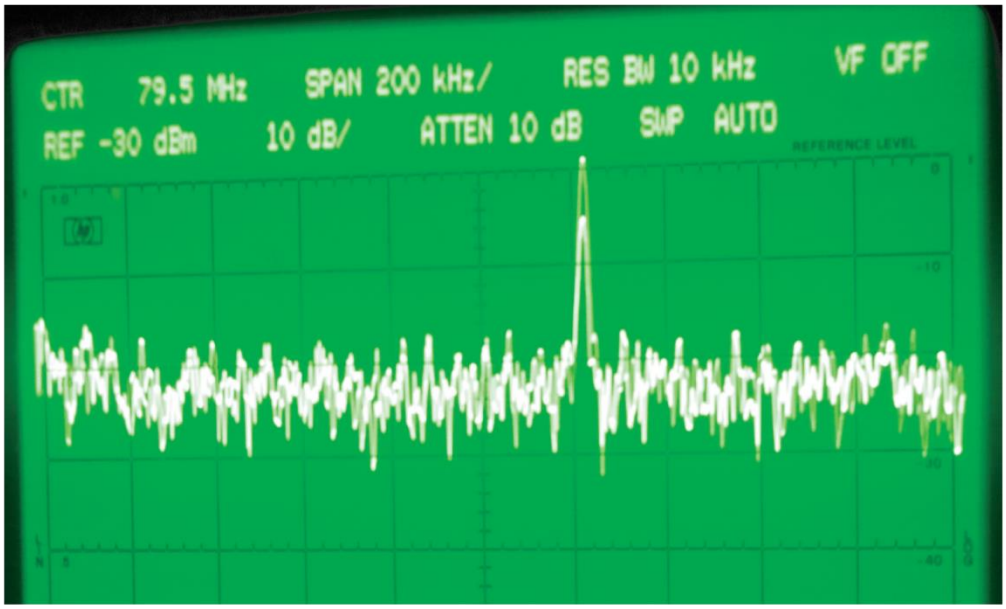
CTR 79.5 MHz
SPAN 200 kHz/
RES BW 10 kHz
VF OFF
REF -30 dBm
10 dB/
ATTEN 10 dB
SWP AUTO

(B)

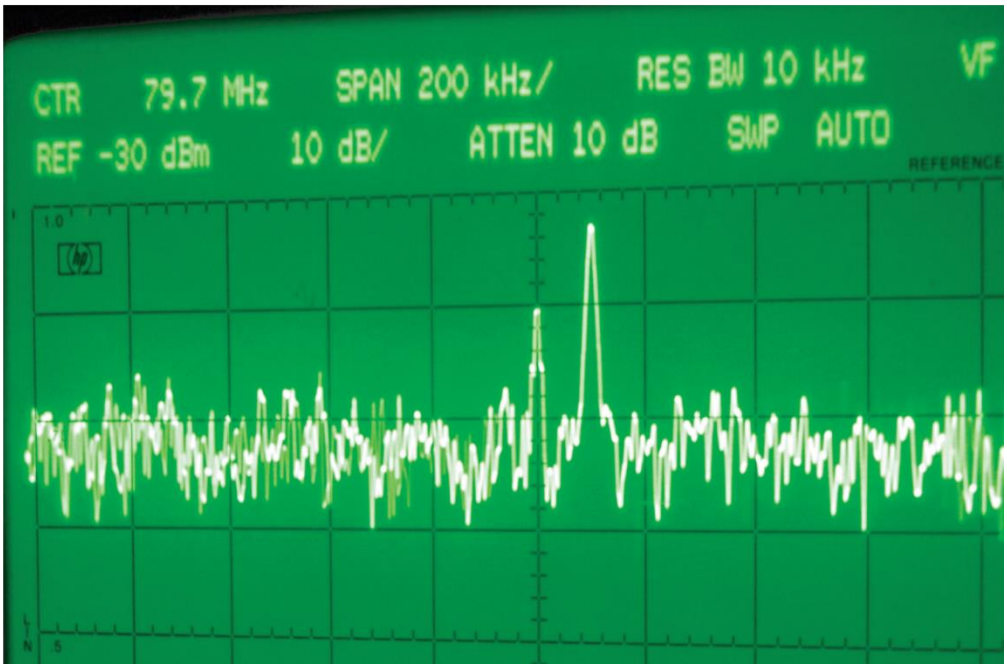
CTR 79.7 MHz
SPAN 200 kHz/
RES BW 10 kHz
VF
REF -30 dBm
10 dB/
ATTEN 10 dB
SWP AUTO

`

Fig2.13 Laser-induced DC and RF current detection with the double lock in technique, the junction is formed by a Ag tip and Cu (110) surface, 220 FHG beam shines into the junction at 2.5mW power out of tunneling, (A) photo-induced electron from tip to sample at positive sample bias, (B) I_{DC} detected by the DC lock-in (black), I_{RF} detected by the RF lock-in (blue), dI_{RF}/dV by the double lock-in technique (red).

`

(A)

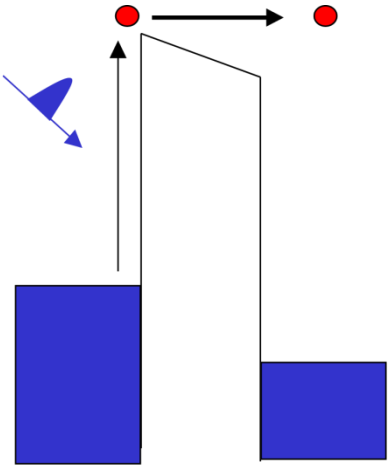
vacuum
Ag tip
Cu(110)

(B)

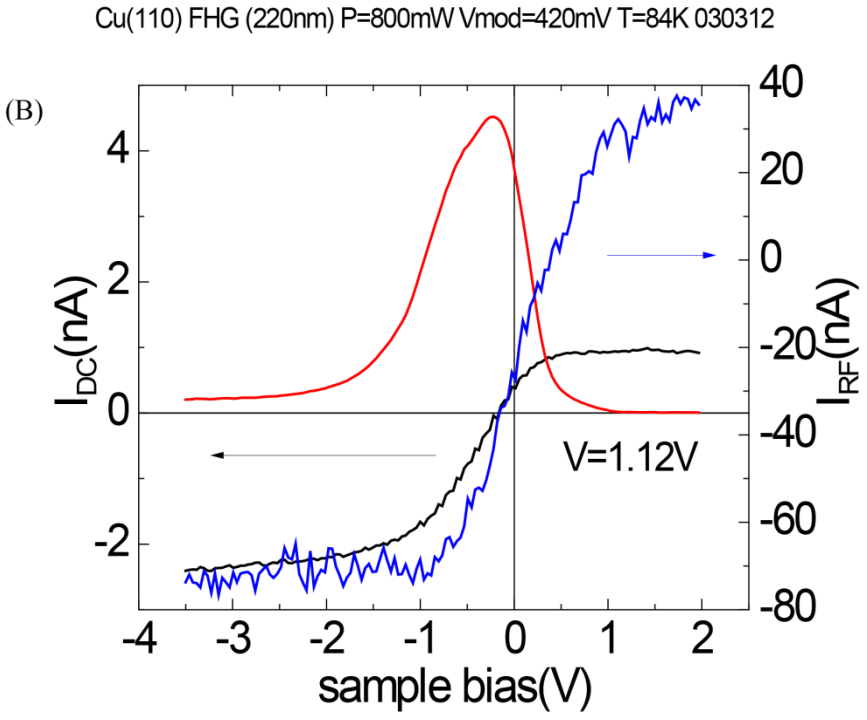
Cu(110) FHG (220nm) P=800mW Vmod=420mV T=84K 030312
I_{DC}(nA)
I_{RF}(nA)
V=1.12V
sample bias(V)

`

Bibliography:

1. "Surface Studies by Scanning Tunneling Microscopy", G. Binning, H. Rohrer, Ch. Gerber and E. Weibel, *Phys. Rev. Lett.* **49**, 57-61(1982).
2. "Photoassisted Scanning Tunneling Microscopy", S.Grafström, *J. Appl. Phys.* **91**, 1717-1753 (2002).
3. "Photon Emission with the Scanning Tunneling Microscope", J. K. Gimzewski, B. Reihl, J. H. Coombs, and R. R. Schlittler, *Z. Phys. B - Condensed Matter* **72**, 497-501 (1988).
4. "Viewing the Interior of a Single Molecule: Vibronically Resolved Photon Imaging at Submolecular Resolution", C. Chen, P. Chu, C. A. Bobisch, D. L. Mills, and W. Ho, *Phys. Rev. Lett.* **105**, 217402 (2010).
5. "Chemical Mapping of a Single Molecule by Plasmon-Enhanced Raman Scattering", R. Zhang, Y. Zhang, Z. C. Dong, S. Jiang, C. Zhang, L. G. Chen, L. Zhang, Y. Liao, J. Aizpurua, Y. Luo, J. L. Yang, J. G. Hou, *Nature* **498**, 82–86 (2013).
6. "Reactions at Metal Surfaces Induced by Femtosecond Lasers, Tunneling Electrons and Heating", W.Ho, *J. Phys. Chem.* **100**, 13050-13060 (1996), and conversations with Wilson and senior group members.
7. "Observation of Coherent Electron Excitation and Electron-Phonon Scattering at Metal Surfaces", Y.-M. Chang, L.J. Lauhon, and W. Ho, to be published.
8. "Two-Photon-Induced Hot-Electron Transfer to a Single Molecule in a Scanning Tunneling Microscope", S. W. Wu and W. Ho, *Phys. Rev. B.* **82**, 085444 (2010).
9. "Real-Space Imaging of Transient Carrier Dynamics by Nanoscale Pump-Probe Microscopy", Y. Terada, S. Yoshida, O. Takeuchi, and H. Shigekawa, *Nat. Photon.* **4**, 869−874 (2010).

`

10. “Probing of Ultrafast Spin Dynamics with Optical Pump-Probe Scanning Tunneling Microscopy”, S. Yoshida, Y. Aizawa, Z. Wang, R. Oshima, Y. Mera, E. Matsuyama, H. Oigawa, O. Takeuchi and H. Shigekawa, *Nat. Nano*. **125** 1-6 (2014).
11. “Two-Color Ultrafast Photoexcited Scanning Tunneling Microscopy”, A. Dolocan, D.P. Acharya, P. Zahl, P. Sutter and N. Camillone III, *J. Phys. Chem. C.*, **115**, 10033-10043 (2011).
12. “An Ultrafast Terahertz Scanning Tunneling Microscope” T. L. Cocker, V. J. Jelic, M. Gupta, S. J. Molesky, J. A. J. Burgess, G. De Los Reyes, L. V. Titova, Y. Y. Tsui, M. R. Freeman, and F. A. Hegmann, *Nat. Photon.* **7**, 620-625(2013).
13. “Laser-Induced Scanning Tunneling Microscopy: Linear Excitation of the Junction Plasmon”, J. Lee, S.M. Perdue, D. Whitmore and V.A. Apkarian, *J. Chem. Phys.* **133**, 104706 (2010).
14. “Single-Molecule Femtochemistry: Molecular Imaging at the Space-Time Limit”, H. Petek, *ACS Nano.* **8**, 5-13(2014).
15. “Ultrafast Electron Dynamics at Cu (111): Response of an Electron Gas to Optical Excitation”, T. Hertel, E. Knoesel, M. Wolf and G. Ertl, *Phys. Rev. Lett.* **76**, 535-538 (1996).
16. “Femtosecond Time-Resolved Two-Photon Photoemission Studies of Electron Dynamics in Metals”, H. Petek and S. Ogawa, *Prog. Surf. Sci.* **56**, 239-310(1997), and private communication with H. Petek.
17. “Field Enhancement of Optical Radiation in the Nearfield of Scanning Probe Microscope Tips”, J. Jersch, F. Demming, L.J. Hilddenhagen and K. Dickmann, *Appl. Phys. A* **66**, 29-34(1998).

`

Chapter 3

Imaging Molecular Orbitals of 4, 7-Di ([2, 20-bithiophen]-5-yl) benzo[c] [1, 2, 5] thiadiazole (4T-BTD) with a STM

3.1 Abstract

STM imaging and spectroscopy are performed to study an organic semiconductor molecule 4, 7-Di ([2, 20-bithiophen]-5-yl) benzo[c] [1, 2, 5] thiadiazole (4T-BTD) on NiAl (110) surface. The STM topography image shows bias dependence, the benzo[c][1, 2, 5] thiadiazole could only be clearly observed at positive biases near lowest unoccupied molecular orbital (LUMO) peak. LUMO and HOMO (highest occupied molecular orbital) dI/dV spectroscopy and imaging show the structure and electronic properties of the molecule at the single molecule level. Inelastic electron tunneling spectroscopy (IETS) imaging at the hydrogen rotational energy shows the sub-Å details of the LUMO orbital of the molecule.

3.2 Introduction

The scanning tunneling microscope (STM) has been a powerful tool to study single-molecule chemistry by imaging and electronic spectroscopy [1]. Despite these successes, various efforts have been made to extend the structural and chemical sensitivities of STM. In 1998, Seventeen years after the invention of STM, STM inelastic electron tunneling spectroscopy (STM-IETS) first achieved chemical identification of molecular species by characterizing vibrational energies [2]. Only recently, scanning tunneling hydrogen microscopy (STHM) [3], inelastic tunneling probe (itProbe) [4] and hydrogen rotational spectromicroscopy [5, 6] achieved chemical and

structural imaging of single molecules with unprecedented details. Such great-detail chemical structures have also been observed with a noncontact atomic force microscope (NC-AFM) [7].

4, 7-Di ([2, 20-bithiophen]-5-yl) benzo[c] [1, 2, 5] thiadiazole (4T-BTD) is a semiconductor benzothiadiazole molecule which has potential applications in organic light emitting diodes (LEDs), organic field effect transistors (FETs) and solar cells [8, 9]. 4T-BTD has donor-acceptor-donor sites inside a single molecule, enabling intramolecular electron transfer; 4T-BTD and its small molecular semiconductor relatives have received great attention due to their advantages *versus* polymer semiconductors: ease of purification, higher charge mobility and overall better performance [10, 11]. Electronic properties of such organic molecules are of central importance to applications, understanding the properties of the conjugated building blocks will help building blocks to extended semiconducting molecules with predictable properties, and ultimately understanding and controlling the collective behavior of multiple components in functional devices [12]. Structure and electronic properties of these molecules can be probed by the STM at the single molecule level and with sub-Å spatial resolution [4, 5, and 6].

The rotational excitations of hydrogen molecule weakly adsorbed on surfaces have been measured with the STM [13, 14]. It was also shown that similar to the vibrations of a CO molecule attached to the tip [4], changes in the adsorption potential well induced by varying the tip-sample distance shift the energies in both vibrational and rotational modes for the hydrogen temporally trapped in the tunnel junction [13]. The sensitivity of the H_2 modes to different chemical environments has been applied to achieve sub-Å structural and molecular orbital imaging of MgP on metal and oxide surfaces [5, 6].

3.3 Experiment

`

The experiments were performed using a home-built STM operating at 12.5 K and a base pressure of 3×10^{-11} Torr [15]. The preparation of NiAl (110) follows previously reported procedures [16]; the NiAl sample was sputtered with Ne ions and annealed at ~1350K. The Ag tip was electrochemically etched and in situ cleaned by a few sputter-anneal cycles. The clean surface at 12.5 K was dosed *in situ* with 4T-BTD. As hydrogen molecules have limited residence time on the NiAl(110) surface at 12.5 K, a background pressure of H_2 is kept at 2×10^{-10} Torr throughout the experiment to maintain a constant population of adsorbed molecules on the surface following an initial dose at 5×10^{-10} Torr for 5 min. A bias voltage is applied to the sample with the tip at virtual ground.

3.4 Results and Discussion

STM topography and spectroscopy are performed to study the 4T-BTD molecule on the NiAl (110) surface in the absence of H_2. The molecules show bias dependence in the topography image. The electron poor benzothiodiazole fragment, which acts as the acceptor unit, can only be clearly imaged at positive biases close to the LUMO energy. Fig 2.1 A is taken at sample bias 1V and the benzothiodiazole fragment is clearly seen, while the benzothiodiazole fragment could not be cleanly imaged in fig 2.1E at sample bias 0.5V. Electronic dI/dV spectrum are performed on a few points of the molecule from 0.8V to 1.8V, the background spectrum on NiAl (110) is flat at this bias range (fig 2.1D, 2.2D and 2.3D BKGD spectrum). There are LUMO peaks on different points of the molecule, although the peak energies of the spectra at different points of the molecules are the same around 1.25V, they show different intensities, with the benzothiodiazole fragment has the strongest peak and two electron rich bithiophen units (donor parts) have the weakest peak. During the spectrum on point D of fig 2.1A, the molecule rotates to a different orientation as shown if fig 2.1E, showing the STM-induced rotational motion of this big 4T-BTD

`

molecule and the possibility of building blocks to extended semiconducting molecules by STM [12].

Spectroscopy LUMO dI/dV imaging is performed to further study the molecular orbitals in the absence of H_2.The dI/dV imaging is taken at 1.2V, near the LUMO peak, dI/dV signal is recorded at each point during the scan. The image is taken at constant current mode (feedback is on during moving the tip and is off during taken the dI/dV signal, fig 2.2B, 2.3B and 2.4B) or constant height mode (tunneling gap is set on the first point and feedback is off during the scan, fig 2.2C, 2.3C and 2.4C). Electronic dI/dV spectra are also taken on various points on the molecules. From the spectroscopy imaging; there are two kinds of LUMO geometries of molecules (fig 2.2 and 2.3). Both kinds have much stronger LUMO dI/dV signal in the center acceptor unit than in the two side donor units (fig 2.2 B, C and fig 2.3B, C). The first LUMO geometry is shown if fig 2.2, there is a dip (around point B in the topography image fig2.2A) in the benzothiodiazole fragment between the high dI/dV signal [1, 2, 5] thiadiazole and benzene ring parts, both in the constant current and constant height dI/dV image. This dip is confirmed by the almost flat dI/dV spectrum on point B of fig 2.2A (fig 2.2D). In the constant current mode, the thiodiazole unit has the strongest signal, there are also side features in the donor parts; while in the constant height mode, the benzene ring part has the strongest dI/dV signal and there are no side features. There is no dip in the second LUMO geometry (fig 2.3B and C), suggesting more hybridization in these molecules, there are no obvious side features in the constant current dI/dV imaging (fig 2.3B). Same as in the first LUMO geometry, the thiodiazole unit has the strongest signal in the constant current mode dI/dV imaging (fig 2.3B) and the benzene ring part has the strongest dI/dV signal in the constant height mode (fig 2.3C). Point dI/dV spectra are also performed on this molecule, different from the molecule in fig 2.2, the points near the center of

this molecule (4, 5, 6, 7 a, b and c) all have strong peak near 1.2V, with points a and 5 have the strongest dI/dV signal.

Calculations show that 4T-BTD molecule has a HOMO-LUMO gap of 2.31eV [11]. The LUMO peak is about 1.2V (fig 2.1, 2.2 and 2.3), thus the HOMO peak should be around -1.1V. Since the NiAl (110) background has some electronic states at the negative bias range -1.4V~-0.5V (fig 2.4D BKGD spectrum), the HOMO dI/dV spectra and images are not as clear as the LUMO ones. However, the electric properties and HOMO geometry can still be studied by dI/dV spectra and HOMO dI/dV imaging (fig 2.4). The molecule shown in fig2.4 is the same one as in fig2.3; the benzothiodiazole unit is not clearly imaged in the topography fig 2.4A at V_B=-1.1V. The constant current dI/dV image highlights the donor units on the two sides of the molecule, especially the top unit (fig 2.4B). The donor units are not so obvious in the HOMO constant height image (fig 2.4C). In both the constant current and constant height dI/dV images, the electron poor [1, 2, 5] thiadiazole are not observed. As can be seen from the point spectra in fig 2.4D, the -1.1V peak is only obvious in the top parts of the molecule (points 1 and 2), spectra on the other points are very similar to the background spectrum.

The STM tip and surface (or molecules absorbed on the surface) form a nanocavity and molecular H_2 can be trapped, the rotational and vibrational modes of the trapped H_2 can be characterized by STM IETS [13, 14]. After introducing H_2 into the UHV chamber, IETS spectra are performed on different points of the molecule to study the interaction between H_2 molecule and the 4T-BTD molecule. While the H_2 IETS spectrum on the background is nearly featureless, the H_2 IETS spectra on different points of the molecule clearly show strong features. H_2 is an electron donor [5], 4T-BTD molecule is an electron acceptor here and the LUMO orbital of the molecule readily accepts electron from H_2. Different from the IETS spectra of H_2 trapped

between tip and MgP molecule on Au (111) and NiAl (110) surfaces, on which both H_2 vibrational and rotational modes could be clearly observed [5, 6]; the IETS spectra of H_2 molecule trapped between tip and the 4T-BTD molecule shows very strong j=0⟶2 rotational mode but the v=0⟶1 vibrational mode signal is much weaker compared to the rotational mode (fig 2.5). The rotational mode position varies from about 37mV to 42mV on the eight points of the molecule; the intensities on the points are also different. These differences suggest the trapped H_2 experience spatially dependent interactions with the underlying 4T-BTD molecule.

Constant current H_2 rotational IETS images (feedback is on during moving the tip and is off during taken the d^2I/dV^2 signal) are taken based on the sensitivity of H_2 interacting with the 4T-BTD molecule. Surprisingly, LUMO of 4T-BTD are clearly imaged on the NiAl (110) surface at V_B=37.1mV, I_T=0.4nA, despite the strong electronic interaction of the molecule and metal substrate. As shown in fig 2.6 B and C, the H_2 rotational IETS imaging matches really well with the calculation from ref.11, except the IETS image is slightly not symmetric probably due to the molecule is slightly tilted as shown in the topography image fig 2.6A. In contrast, the H_2 rotational imaging of MgP can only observe the submolecular electronic structure on the oxide surface [5, 6].

Since the spectra show different peak positions on different points of the molecule (fig 2.5C), H_2 rotational IETS images are taken at different biases; these images highlight different parts of the molecule, fig 2.6D highlights the LUMO geometry on the left side of the molecule and fig 2.6E highlights the LUMO geometry of the right side of the molecule. In contrast, the IETS image taken at V_B=60.1mV, I_T=0.65nA (far away from H_2 rotational mode) is featureless (fig 2.6F).

`

3.5 Conclusions

STM imaging and spectroscopy are performed on 4T-BTD molecule, a molecule that has intramolecular donor-acceptor-donor sites. The electron poor benzothiodiazole fragment in the acceptor site can only be clearly imaged at bias near the LUMO peak. LUMO dI/dV spectra clearly show that the center acceptor unit has higher peaks, LUMO dI/dV imaging more clearly highlights the center acceptor part. In contrast, HOMO dI/dV spectra weakly shows the two side donor units have stronger peak and the HOMO imaging confirms this. H_2 rotational IETS imaging is performed on the molecule, LUMO structure of the molecule are more clearly imaged at sub-Å resolution, which is the first time observe sub- Å details of the molecular orbital on the metal surface by using H_2. Such an understanding of this kind of molecules will help building blocks to extended semiconducting molecules with predictable properties.

Acknowledgements

This work is supported by the National Science Foundation Center for Chemical Innovation at the Space-Time Limit (CaSTL) under Grant No. CHE-1414466, we thank S.W. Li, A. Yu and G. Czap for stimulating discussions.

`

Fig 3.1 (A) 29Å ×29Å constant current STM topographic image of a 4T-BTD molecue on NiAl (110) surface, the tunneling gap is set with V_B=1.0V and I_T=0.1nA and the temperature is at 12.5K, (B) diagram of this 4T-BTD molecule, (C) ball-stick model of the molecule, (D) Tunneling spectra taken on different points of the 4T-BTD molecule in (A), the tunneling gap is set with V_B=1V and I_T=0.1nA, (E) 29Å ×29Å constant current STM topographic image of a 4T-BTD molecue on NiAl (110) surface, the tunneling gap is set with V_B=0.05V and I_T=0.1nA, the molecule rotates after doing spectroscopy on point D in panel (A), also the "benzothiodiazole fragment" is not so obvious as with V_B=1V.

`

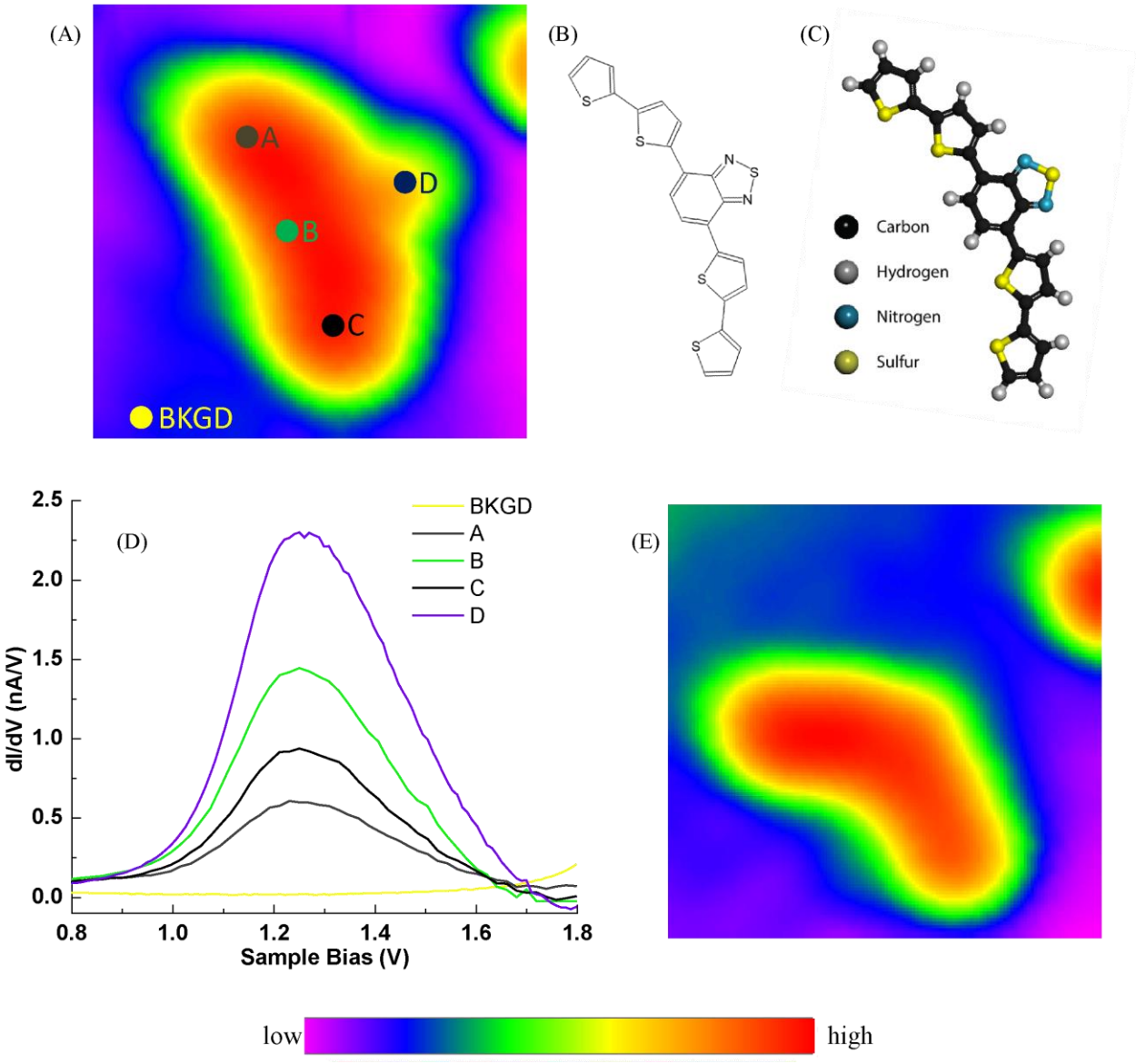
(A)
A
D
B
C
BKGD
(B)
S
S
N
S
N
S
S
(C)
Carbon
Hydrogen
Nitrogen
Sulfur
(D)
BKGD
A
B
C
D
dI/dV (nA/V)
2.5
2.0
1.5
1.0
0.5
0.0
0.8
1.0
1.2
1.4
1.6
1.8
Sample Bias (V)
(E)
low
high

`

Fig 3.2: (A) 29Å ×29Å STM topography image taken at V_B=1V, I_T=60pA, (B) constant current dI/dV image taken at V_B=1.2V, the tunneling gap is set at V_B=1V, I_T=60pA, (C) constant height dI/dV image taken at V_B=1.2V, the tunneling gap is set at V_B=1V, I_T=150pA, (D) dI/dV spectra taken at different points of the molecule, the tunneling gap is set at V_B=1V, I_T=60pA.

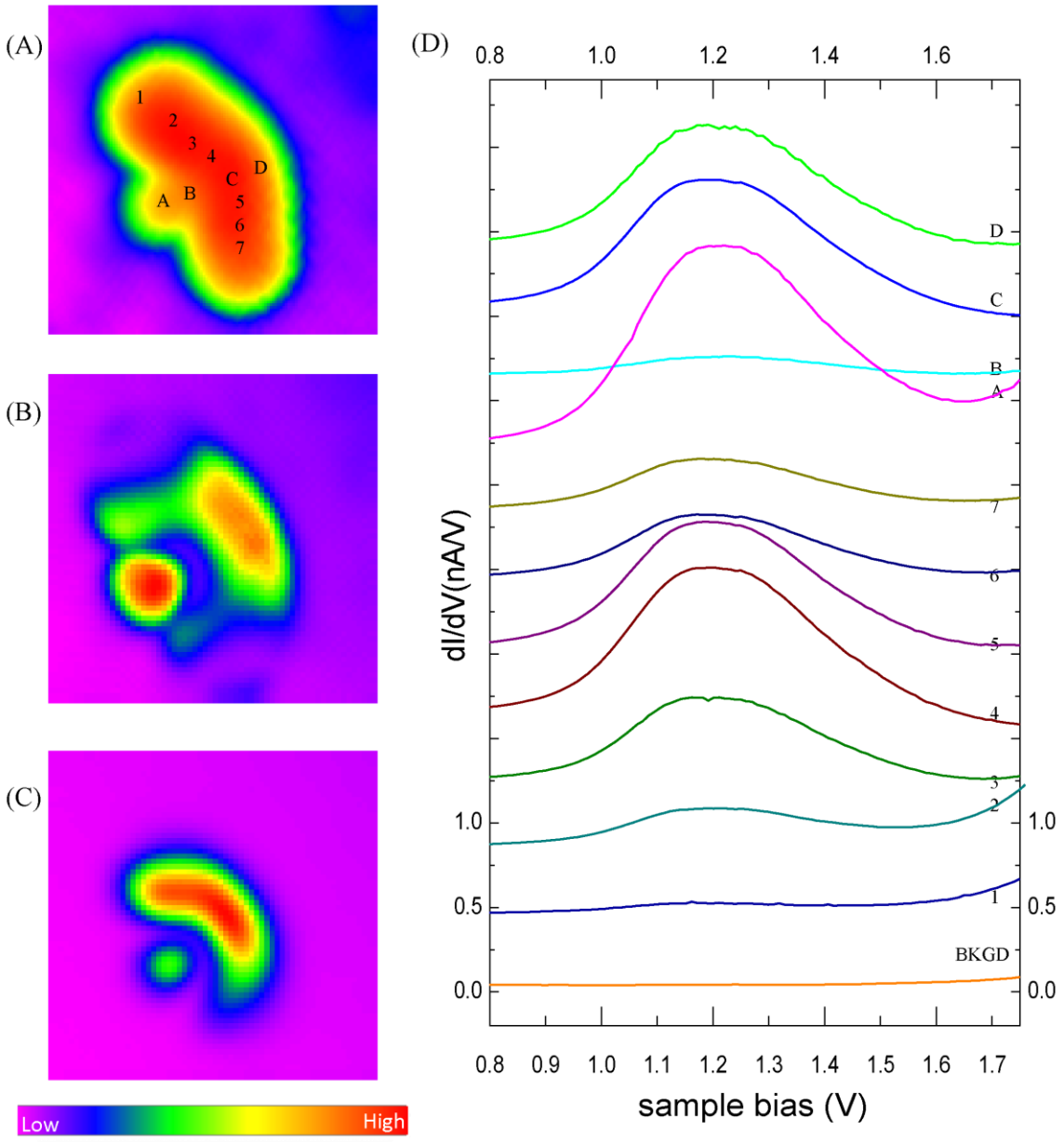
(A)
1
2
3
4
C
D
A
B
5
6
7
(B)
(C)
Low
High
(D)
0.8
1.0
1.2
1.4
1.6
D
C
B
A
7
6
5
4
3
2
1
BKGD
dI/dV(nA/V)
1.0
0.5
0.0
0.8
0.9
1.0
1.1
1.2
1.3
1.4
1.5
1.6
1.7
sample bias (V)

`

Fig 3.3: (A) 29Å ×29Å STM topography image taken at V_B=1.2V, I_T=50pA, (B) constant current dI/dV image taken at V_B=1.2V, I_T=50pA, (C) 29Å ×29Å constant height dI/dV image taken at V_B=1.2V, I_T=50pA, (D) dI/dV spectra taken at different points of the molecule, the tunneling gap is set at V_B=1.2V, I_T=50pA.

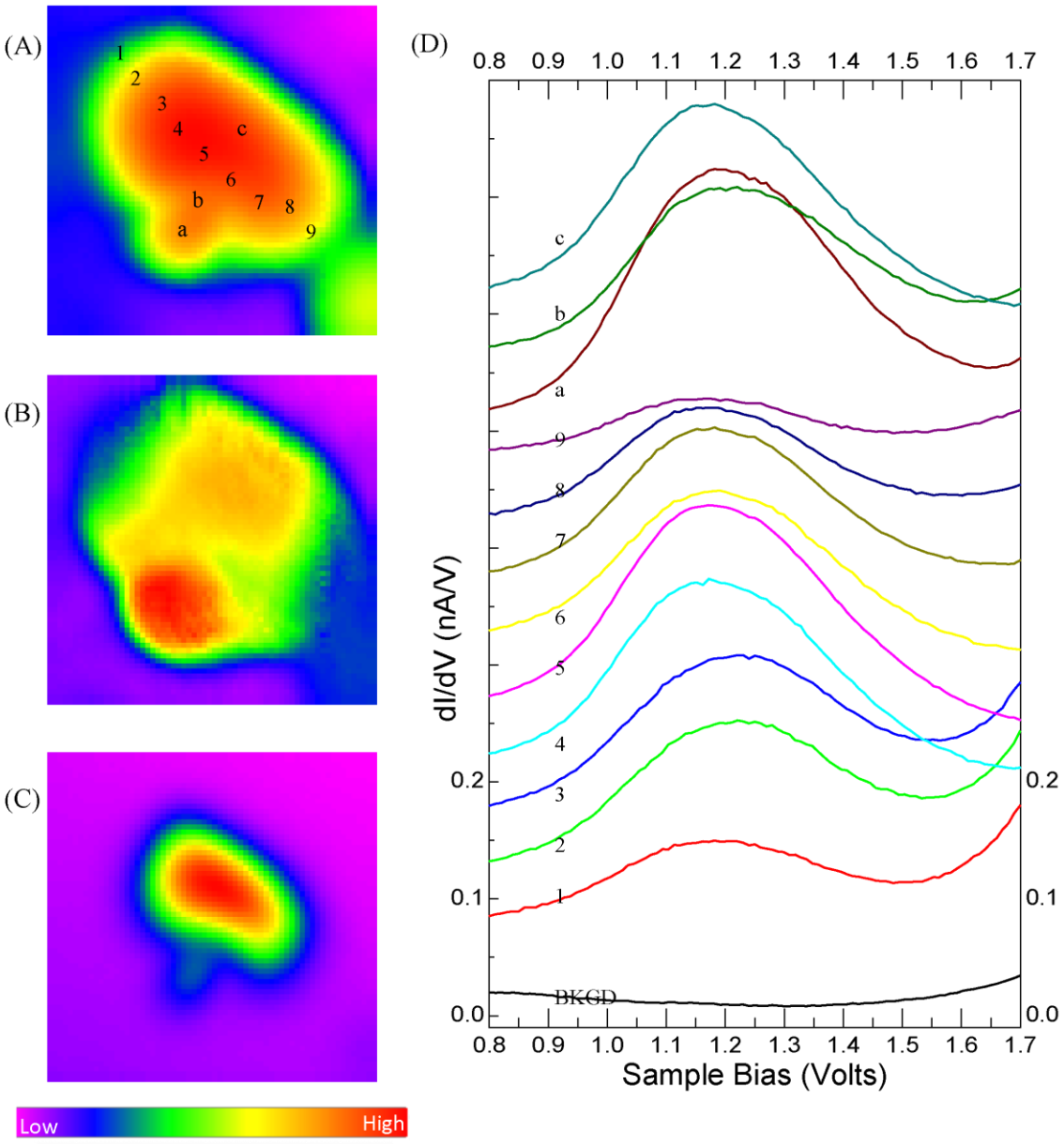
(A)
1
2
3
4
c
5
6
b
7
8
a
9
(B)
(C)
Low
High
(D)
0.8 0.9 1.0 1.1 1.2 1.3 1.4 1.5 1.6 1.7
c
b
a
9
8
7
6
5
4
3
2
1
BKGD
dI/dV (nA/V)
0.0
0.1
0.2
Sample Bias (Volts)

`

Fig 3.4: (A) 29Å ×29Å STM topography image taken at V_B=-1.1V, I_T=60pA, (B) constant current dI/dV image taken at V_B=-1.1V, I_T=60pA, (C) 29Å ×29Å 29Å ×29Å constant height dI/dV image taken at V_B=-1.1V, I_T=60pA, (D) dI/dV spectra taken at different points of the molecule, the tunneling gap is set at V_B=-1.07V, I_T=100pA.

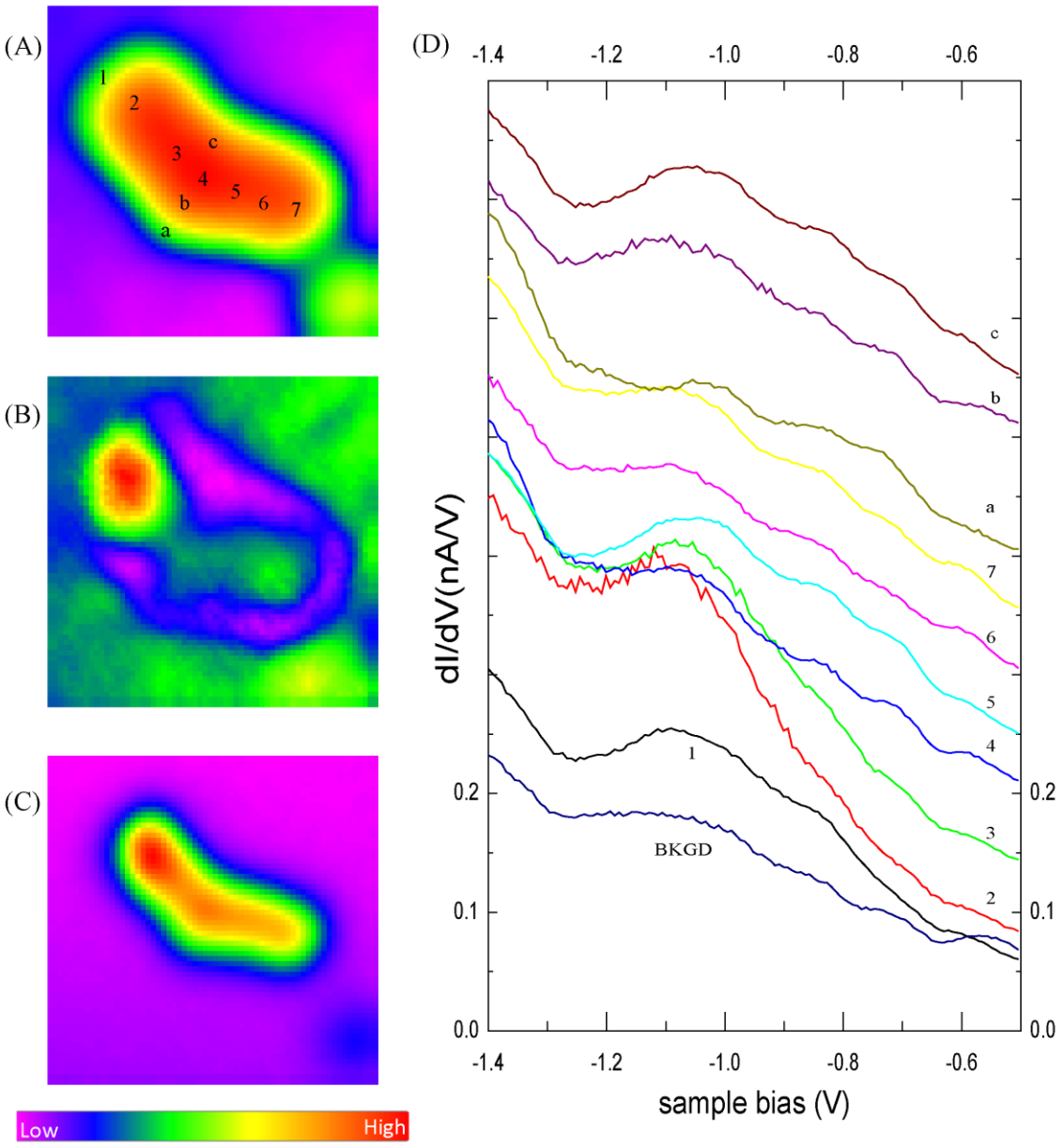
(A)
1
2
3
c
4
5
b
6
7
a
(B)
(C)
Low
High
(D)
-1.4
-1.2
-1.0
-0.8
-0.6
dI/dV(nA/V)
c
b
a
7
6
5
4
1
3
BKGD
2
0.2
0.1
0.0
sample bias (V)

`

Fig 3.5: (A) 30.5Å ×30.5Å STM topography image taken at V_B=37.1mV, I_T=0.4nA, (B) IETS image at V_B=37.1mV, I_T=0.4nA, (C) IETS spectra taken at different points of the molecule, the tunneling gap is set at V_B=38mV, I_T=400pA.

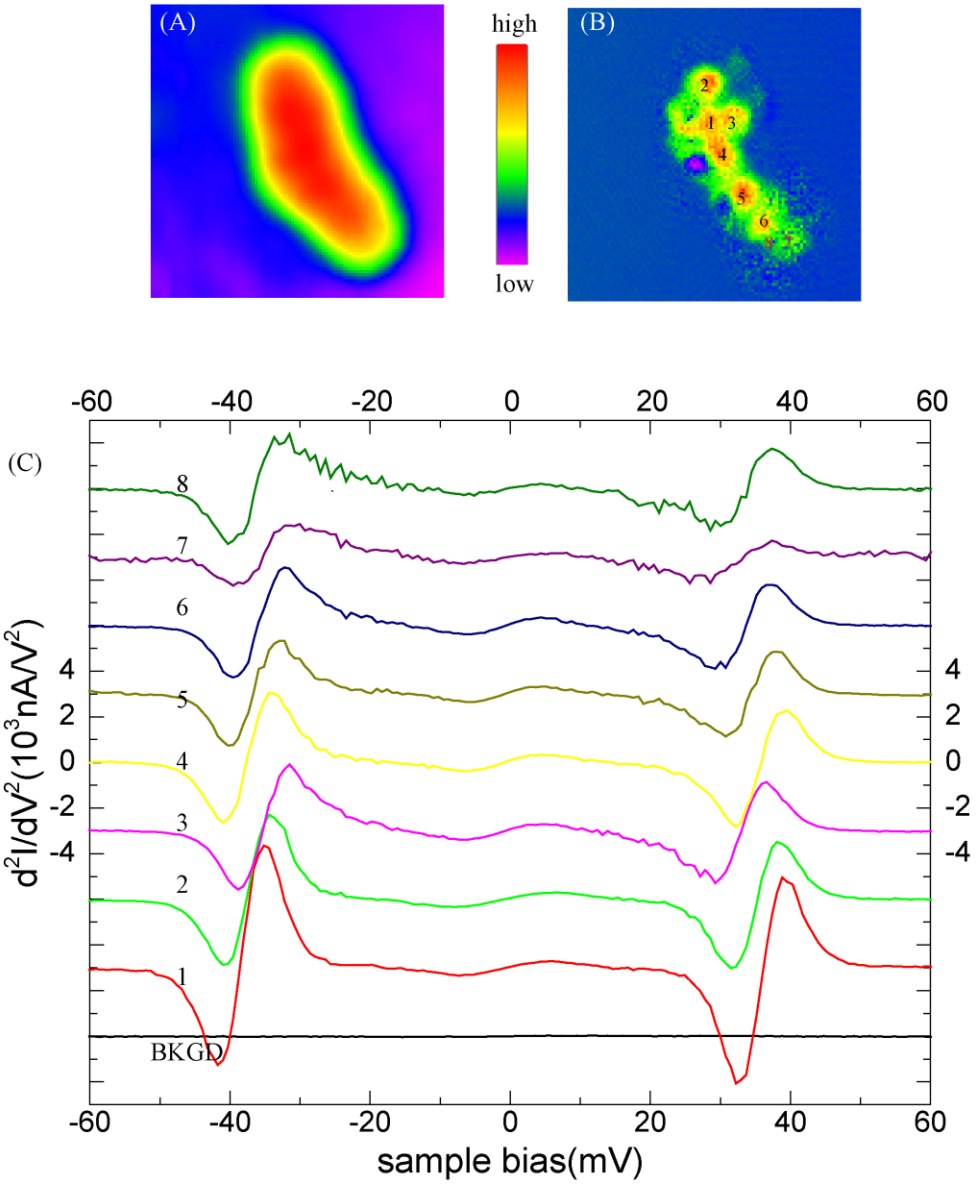
(A)
high
low
(B)
1
2
3
4
5
6
(C)
8
7
6
5
4
3
2
1
BKGD
-60
-40
-20
0
20
40
60
4
2
0
-2
-4
$d^2I/dV^2(10^3nA/V^2)$
sample bias(mV)

`

Fig 3.6: (A) 30.5Å ×30.5Å STM topography image taken at V_B=37.1mV, I_T=0.4nA, (B) IETS image at V_B=37.1mV, I_T=0.4nA, (C) 30.5Å ×30.5Å IETS image taken at V_B=44.9mV, I_T=0.48nA, (D) 29Å ×29Å IETS image at V_B=-39.1mV, I_T=0.65nA, (E) 30.5Å ×30.5Å IETS image at V_B=34.9mV, I_T=0.45nA, (F) 29Å ×29Å IETS image at V_B=60.1mV, I_T=0.65nA.

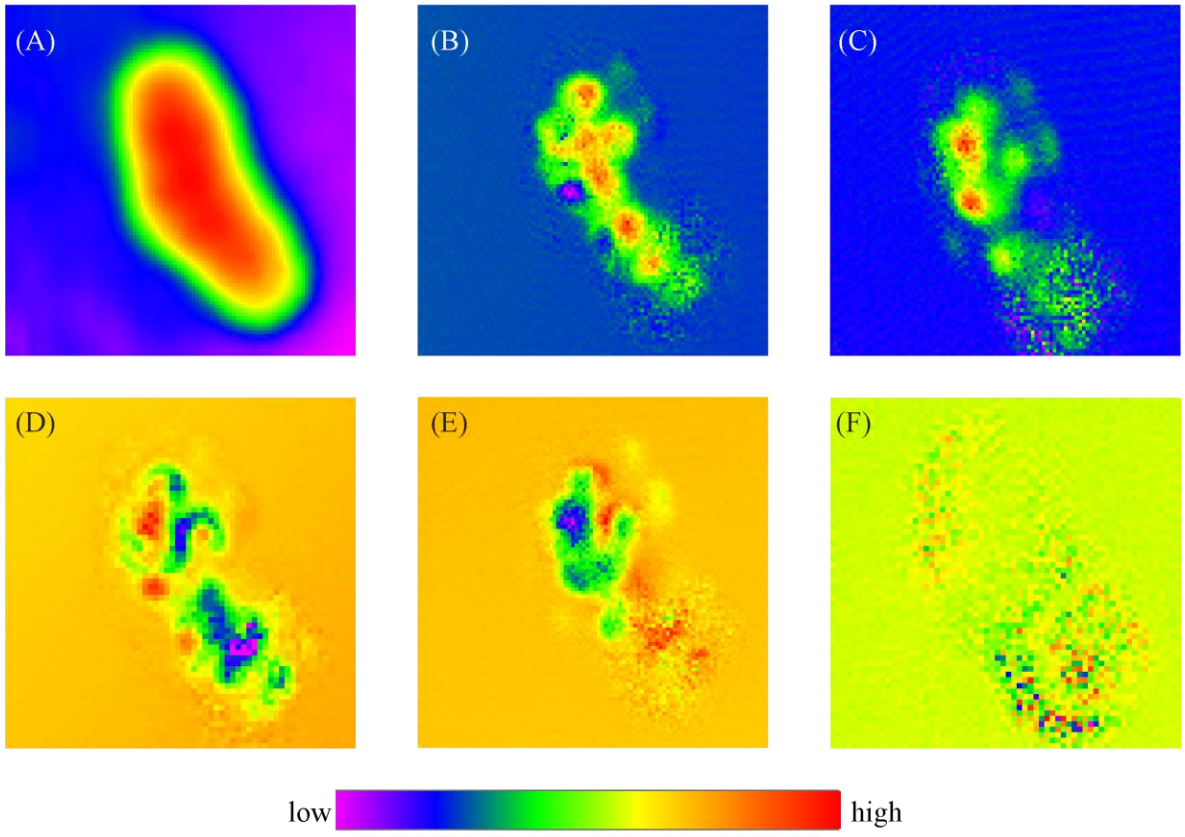
(A)
(B)
(C)
(D)
(E)
(F)
low
high

`

Bibliography

1. "Single-molecule Chemistry", W. Ho, *J. Chem. Phys.* **117**, 11033-11061 (2003).
2. "Single Molecule Vibrational Spectroscopy and Microscopy", B. C. Stipe, M. A. Rezaei, W. Ho, *Science* **262**, 218-220(1998).
3. "Direct Imaging of Intermolecular Bonds in Scanning Tunneling Microscopy", C. Weiss, C. Wagner, R. Temirov, and F. S. Tautz, *J. Am. Chem. Soc.* **132**, 11864 (2010).
4. "Real-Space Imaging of Molecular Structure and Chemical Bonding by Single-Molecule Inelastic Tunneling Probe", C. L. Chiang, C. Xu, Z. Han and W. Ho, *Science* **344**, 885-888(2014).
5. "Rotational Spectromicroscopy: Imaging the Orbital Interaction between Molecular Hydrogen and an Adsorbed Molecule", S. Li, D. Yuan, A. Yu, G. Czap, R. Wu and W. Ho, *Phys. Rev. Lett.* **114**, 206101 (2015).
6. "Single-Molecule Rotational and Vibrational Spectroscopy and Microscopy with the Scanning Tunneling Microscope", A. Yu, S. Li, G. Czap and W. Ho, *J. Phys. Chem. C*, **119**, 14737-14741 (2015).
7. "The Chemical Structure of a Molecule Resolved by Atomic Force Microscopy", L. Gross, F. Mohn, N. Moll, P. Liljeroth and G. Meyer, *Science* **325**, 1110-1114(2009).
8. "Small Molecule Organic Semiconductors on the Move: Promises for Future Solar Energy Technology", A. Mishra and P. Bäuerle, *Angew. Chem. Intl. Ed*, **51**, 2020-2067(2012).
9. "Luminescent solar concentrator comprising disubstituted benzothiadiazole compounds", *European Patent Application* **EP** 2 557 606 A1 (2013).

`

10. “Solution-processed Small-molecule Solar Cells with 6.7% efficiency”, Y. Sun, G. C. Welch, W. L. Leong, C. J. Takacs, G. C. Bazan and A. J. Heeger, *Nat. Mater*. **11** 44-48 (2012).
11. “Perfluoroalkyl-substitution *versus* Electron-deficient Building Blocks in Design of Oligothiophene Semiconductors”, H. T. Black, A. Dadvand, S. Liu, V. S. Ashby and D. F. Perepichka, *J. Mater. Chem. C* **1** 260-267(2013).
12. “Design Strategies for Organic Semiconductors beyond the Molecular Formula”, Z. B. Henson, K. Müllen and G. C. Bazan, *Nat. Chem*. **4** 699-704 (2012).
13. “Rotational and Vibrational Excitations of a Hydrogen Molecule Trapped within a Nanocavity of Tunable Dimension”, S. Li, A. Yu, F. Toledo, Z. Han, H. Wang, H. Y. He, R. Wu and W. Ho, *Phys. Rev. Lett.* **111**, 146102 (2013).
14. “Distinction of Nuclear Spin States with the Scanning Tunneling Microscope”, F. D. Natterer, F. Patthey and H. Brune, *Phys. Rev. Lett.* **111**, 175303 (2013).
15. “A Variable-temperature Scanning Tunneling Microscope Capable of Single-molecule Vibrational Spectroscopy”, B. C. Stipe, M. A. Rezaei, W. Ho, *Rev. Sci. Instrum*. **70**, 137−143 (1999).
16. “Vibrationally Resolved Fluorescence Excited with Submolecular Precision”, X. H. Qiu, G. V. Nazin, W. Ho, *Science* 299, 542-546(2003).

`

Chapter 4

Imaging Metal-Molecule Chain and Single Molecule of 1, 4-Phenylene Diisocyanide on Noble Metal Surfaces and Their Interaction with Small Molecules

4.1 Abstract

1, 4-Phenylene Diisocyanide (PDI) forms 1-D nanochains on Au (111) surface, IETS spectra are performed on the CO_2 adsorbed on the chain. PDI forms chains on Cu (110) surface at room temperature, CO_2 also prefers to adsorb on the chains even the Cu-PDI chains break after cooling down to 12.5K. The single PDI molecule, which can capture small molecules like H_2, is also studied on Cu (110) and Ag (100) surfaces. Imaging of the single molecule with H_2 and CO shows sub-Å details of the molecule. On the Cu (110) surface, at low H_2 coverage, the H_2 IETS image highlights the two N atoms in the molecule; at high H_2 coverage, the topography image when the tip is close shows the molecule structure and the interaction of molecule with the surface, the more detailed ring structure and molecule interaction with the substrate are observed in the IETS image. H_2 IETS spectra are taken on different points of the molecule, showing H_2 sensitivity of interaction with the molecule. Moreover, CO adsorbed on the Ag (100) surface can be picked up by a Ag tip and high resolution images of single PDI molecule is also got with the Ag-CO tip.

4.2 Introduction

The scanning tunneling microscope (STM) has been a powerful tool to study single-molecule chemistry by imaging and electronic spectroscopy [1]. Despite these successes, various efforts

`

have been made to extend the structural and chemical sensitivities of STM. STM inelastic electron tunneling spectroscopy (STM-IETS) first achieved chemical identification of molecular species by characterizing vibrational energies [2]. Only recently, scanning tunneling hydrogen microscopy (STHM) [3], inelastic tunneling probe (itProbe) [4] and hydrogen rotational spectromicroscopy [5, 6] achieved chemical and structural imaging of single molecules with unprecedented details. Such great-detail chemical structures have also been observed with a noncontact atomic force microscope (NC-AFM) by using a CO-terminated tip [7].

1, 4-Phenylene Diisocyanide (PDI) is a unique molecule that can self-assemble into nanostructures on noble metal Au [8-11], Cu [12] and Ag [13] surfaces. The negatively charged carbon atom in the two N-C groups readily to donate electrons to noble metal atoms on the surface and form nanostructures like 1D nanochains [9, 10], which are 1-D conductor. Moreover, the nanochains can chemically and physically absorb small molecules like carbon dioxide (CO_2) [11, 12]. When linked between nanoparticles [14, 15] or formed layers on surface [16], PDI molecules show interesting electrical and plasmonic properties, making it a potential candidate for molecular electronics. Structure and electronic properties of the PDI molecule can be probed by the STM at the single molecule level and with sub-Å spatial resolution [4, 5, and 6].

The vibrational and rotational excitations of hydrogen molecule weakly adsorbed on surfaces have been measured with the STM [17, 18]. It was also shown that similar to the vibrations of a CO molecule attached to the tip [4], changes in the adsorption potential well induced by varying the tip-sample distance shift the energies in both vibrational and rotational modes for the hydrogen temporally trapped in the tunnel junction [17]. The sensitivity of the H_2 modes to different chemical environments has been applied to achieve sub-Å structural and molecular orbital imaging of MgP on metal and oxide surfaces [5, 6]. With a CO terminated tip,

`

even higher resolution STM itProbe [4] and NC-AFM images [7] have been achieved. Here we focus on the sub-Å imaging and spectroscopy of single PDI molecule with H_2 and CO, the understanding of single PDI sub-molecular should help the understanding the self-assembled structure, its electronic properties and the interactions with nanoparticle and small molecules.

4.3 Experiment

The experiments were performed using a home-built STM operating at 12.5 K and a base pressure of 3×10^{-11} Torr [19]. The Au (111), Cu (110), Ag (100) sample sputtered and annealed to about 520℃. The Ag tip was electrochemically etched and in situ cleaned by a few sputter-anneal cycles. PDI molecules are dosed onto Au (111) and Cu (110) at room temperature to form chains and then cooled down to 12.5K for low temperature study. PDI molecules are dosed onto the clean Cu (110) and Ag (100) surfaces at 12.5 K for single-mole studies. H_2 molecules were introduced into UHV chamber for imaging on Cu (110) surface, as hydrogen molecules have limited residence time on the Cu (110) surface at 12.5 K, for the low H_2 coverage imaging, a background pressure of H_2 is kept at 5×10^{-10} Torr throughout the experiment to maintain a constant population of adsorbed molecules on the surface following an initial dose at 1×10^{-9} Torr for 5 min. For the high H_2 coverage imaging, a background pressure of H_2 is kept at 2×10^{-9} Torr. CO is evaporated onto the Ag (100) surface and picked up by the Ag tip to image the single PDI molecule. For all these experiments, a bias voltage is applied to the sample with the tip at virtual ground.

4.4 Results and Discussion

At room temperature, PDI molecules are evaporated onto Au (111) surface following reported recipes [8, 10, and 11]; Au-PDI chains are formed on the surface. Then the chains are cooled

`

down to 12.5K for imaging and absorb CO_2. The chains are consisted by alternating PDI molecule and Au atoms, the bigger dots are PDI molecules and the smaller ones are Au atoms (fig 4.1 A and B). Both PDI and Au has a ~2V peak in the dI/dV spectrum, showing the chain is a 1D conductor (fig 2.1C). CO_2 is evaporated onto the chain and IETS are performed on the CO_2, showing two modes at ~20mV and ~50mV. PDI molecules are also evaporated onto the Cu (110) surface at room temperature to form chains, the chains break after cooling down to 12.5K, possibly because Cu atom takes off the CN groups and sink into the Cu surface (fig 4.2 A and B). CO_2 still prefers the chains even the Cu atoms are missing (fig 4.2C). IETS are also performed on the CO_2, showing two modes at ~20mV and ~2.5mV (fig4.2D).

Single PDI molecules are evaporated onto the Cu (110) surface at 12.5K, at this temperature, the molecules freeze and chain structures are not formed. The STM tip and surface (or molecules absorbed on the surface) form a nanocavity and molecular H_2 can be trapped, the rotational and vibrational modes of the trapped H_2 can be characterized by STM IETS [17, 18]. After introducing 5×10^{-10} Torr H_2 into the UHV chamber, IETS spectra are performed on different points of the molecule to study the interaction between H_2 molecule and the PDI molecule. While the H_2 IETS spectrum on the background is nearly featureless, the H_2 IETS spectra on different points of the molecule clearly show strong features (fig 4.4C). Single molecules are imaged on the Cu (110) surface by H_2 topography and IETS imaging at this lower H_2 coverage. The topography image only show two dimples near the two N-C groups, same as the topography image without H_2(Fig 4.3A and B), but the H_2 IETS imaging clearly resolve the submolecular structure of the PDI molecule (fig 4.3 C). The two bright spots in fig4.3C (more clearly 3 and 5 in fig 4.4B, which is the same IETS image) are ~6Å apart, suggesting they are two N atoms in the PDI molecule, which are about 6Å away, Making the two weak spots near N

(1 and 6 in fig 4.4B) probably C atoms. From the point spectra in fig 4.4C, the two N (3 and 5) have very similar spectra; the two C (1 and 6) also have similar spectra, except the peak intensities are different. The spectrum on transition point 2 shows transitional features from the spectra on point 1(C) to point 3(N). H_2 IETS spectrum on the center of the molecule (point 4) is almost the same as on the BKGD, showing the center of the ring does not interact with H_2 at this coverage. Six spots nearby (7 and 9 are listed as examples here) can also trap H_2, the spectra on 7 and 9 are almost the same and they are similar to the spectra on the N sites (3 and 5). There are some gaps between N and the trapped state (point 8 with spectrum shown is an example here) which do not attract H_2. All the H_2 IETS spectra (except on BKGD, points 4 and 8, which do not attract H_2) show the ~40mV j=0⟶2 rotational mode, although the peak position and intensity are different. Different from the H_2 IETS spectra on MgP [5, 6] and 4T-BTD molecules [20], the v=0⟶1 vibrational peaks on the PDI molecule are strong. H_2 rotational and vibrational IETS images are taken at different biases, the image shown here (fig 4.3C or fig4.4B) is taken at the 5mV vibrational mode and shows most features of the molecule.

After the imaging and spectra at low H_2 coverage, more H_2 is introduced to the UHV chamber to do Scanning Tunneling Hydrogen Microscopy (STHM) [3] and H_2 IETS image. At this high H_2 coverage, three parts of the molecule (the benzene ring and two N-C groups) can be clearly resolved in the topography image when the tip is close (fig 4.5B), such submolecular details could not be resolved when the tip is far away (fig 4.5A). The tip-close topography image (fig 4.5B) also shows there is interaction between the PDI molecule and Cu (110) substrate. The H_2 IETS image at the -8.8mV H_2 vibrational mode shows more clearly the ring structure in the center, two N-C groups, and the interaction with the substrate (fig 4.5C and 4.6B). H_2 IETS spectra are also performed on different points of the molecule at this high H_2 coverage, generally

`

at the same tunneling set point the signals are stronger than the spectra on molecule at low H_2 coverage (fig4.4C), spectra on only one N-C group is shown (1, 2, 3 and 4 on fig 4.6B) since the spectra on the other group are symmetric. As seen in fig 4.C, spectrum on the Cu (110) background already shows strong IETS features at such high coverage, including the rotational modes and vibrational modes, showing the Cu surface starts to attract H_2 at high coverage. The H_2 rotational and vibrational modes are also observed in the center benzene ring of the molecule, although the signal is weaker than most points on the molecule and even the background. The points above and below the molecule (6 and 7) also have weaker H_2 signals than the background. The points on or near the N-C groups (1, 2 3 and 4) all show strong H_2 IETS signals, although the peak position and intensity are very different, showing strong H2 sensitivity over these N-C groups. Such high sensitivity is confirmed in the IETS images (fig 4.5C or 4.6B); very sharp transitions could be imaged, most notably around point 3 in fig4.6B. IETS images at different biases highlight different parts of the molecule (fig 4.7); while vibrational modes images highlight (fig 4.7A and C) the CN groups of the molecule, rotational modes also highlight the interactions around the molecule, especially between the CH groups and substrate (fig 4.7B and D).

Single PDI molecules are studied also studied with a CO terminated tip on the Ag (100) surface, CO is picked up by the Ag tip from substrate by scanning close and is confirmed by IETS spectra showing CO vibrational modes at ~4mV and ~19mV on the background. CO in the topography image looks like a protrusion instead of a dip (fig 4.8A); also indicating the CO on surface is imaged with a CO tip [4]. STM topography image of the PDI molecule when the CO tip is close show similar structure with H_2 imaging, the dip on the two N-C groups and the interaction between molecule and substrate (fig 4.8 B and D). These CO tip topography images

`

suggesting that the interaction features around CH groups (fig 4.8B, D and fig 4.5B) are not from the interaction with CO or H_2, but from the CH groups on the molecule and substrate, probably H bonds.

4.5 Conclusions

1, 4-Phenylene Diisocyanide (PDI) forms 1-D nanochains on Au (111) surface, STM-IETS is performed on the adsorbed CO_2. PDI also forms chains on Cu (110) surface, even though the chains break down at 12.5K, CO_2 still prefers to go to the chains and STM-IETS is performed. Single PDI molecules are studied on Cu (110) surface with H_2 imaging. At low H_2 coverage, while the STM topography image only shows two dimples which may be the N-C groups, the STM H_2 IETS image clearly shows the two N sites. At high H_2 coverage, the topography image already shows three parts of the molecule with interactions with the surface, the IETS image shows more details of the molecule and its interaction with the substrate, with better contrast and sharper transitions.

Acknowledgements

This work is supported by the National Science Foundation Center for Chemical Innovation at the Space-Time Limit (CaSTL) under Grant No. CHE-1414466, we thank S.W. Li, A. Yu, G. Czap, Z. Han and C. Xu for stimulating discussions.

`

Fig 4.1 Au-PDI chains on the Au (111) surface, (A) 112Å ×112Å STM topography image taken at V_B=1V, I_T=0.1nA, (B) 56Å ×56Å STM topography image taken at V_B=1V, I_T=0.1nA, (C) dI/dV spectra over the PDI and Au in the chain, the tunneling gap is set at V_B=2V, I_T=0.1nA, (D) IETS spectrum of the CO_2 adsorbs on the chain, the tunneling gap is set at V_B=-65mV, I_T=0.3nA.

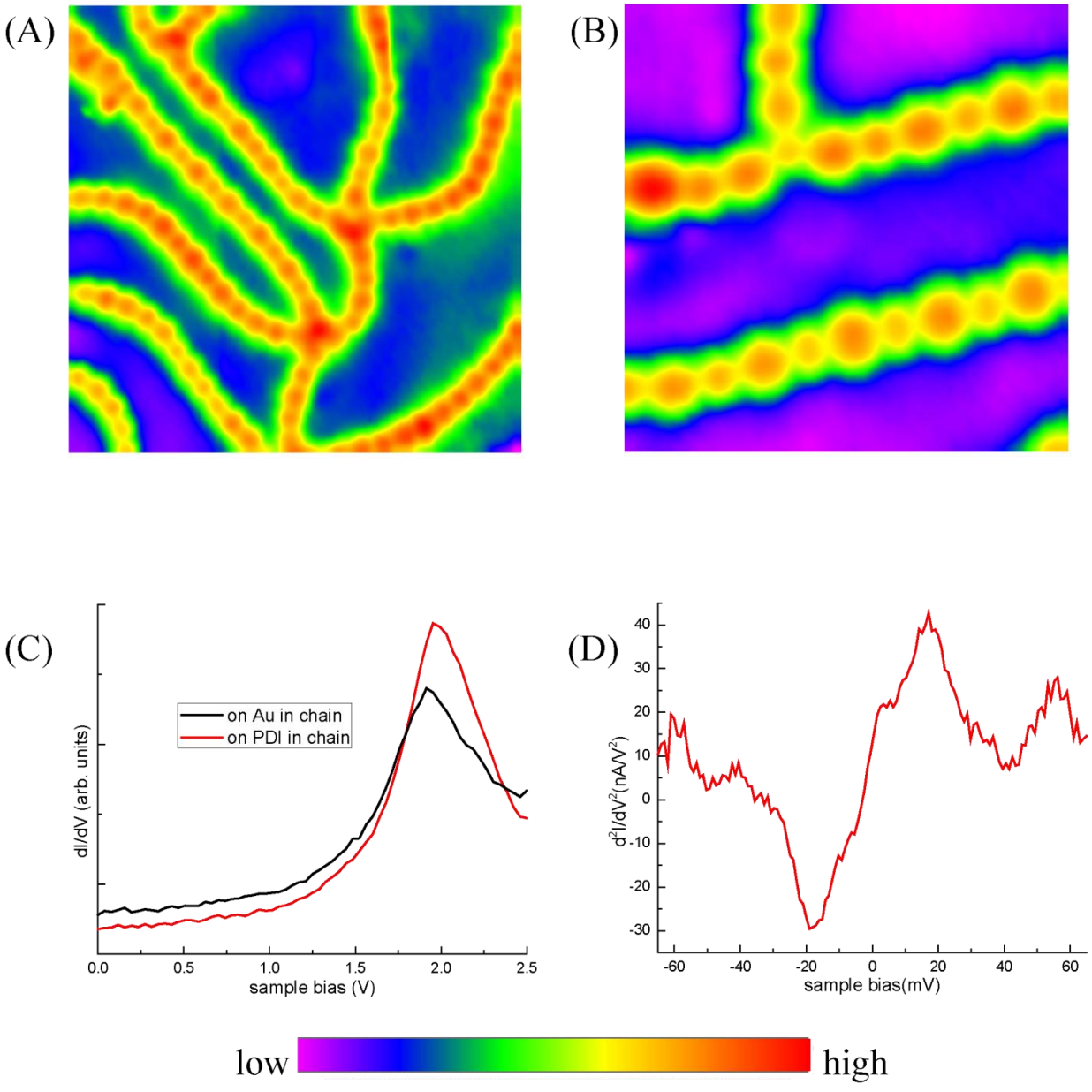
(A)
(B)
(C)
(D)
on Au in chain
on PDI in chain
dI/dV (arb. units)
sample bias (V)
0.0
0.5
1.0
1.5
2.0
2.5
d²I/dV²(nA/V²)
sample bias(mV)
40
30
20
10
0
-10
-20
-30
-60
-40
-20
0
20
40
60
low
high

`

Fig 4.2 Broken Cu-PDI chains on the Cu (110) surface, (A) 58Å ×58Å STM topography image taken at V_B=0.65V, I_T=0.15nA, (B) 29Å ×29Å STM topography image taken at V_B=-0.5V, I_T=0.20nA, (C) 58Å ×58Å STM topography image taken at V_B=65mV, I_T=0.10nA, CO_2 adsorbs on broken Cu-PDI chains on the Cu (110) surface, (D) IETS spectrum of the CO_2 adsorbs on the broken chain, the tunneling gap is set at V_B=65mV, I_T=0.20nA.

`

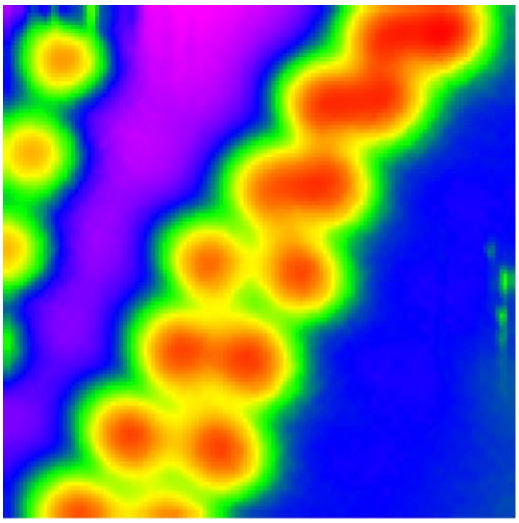

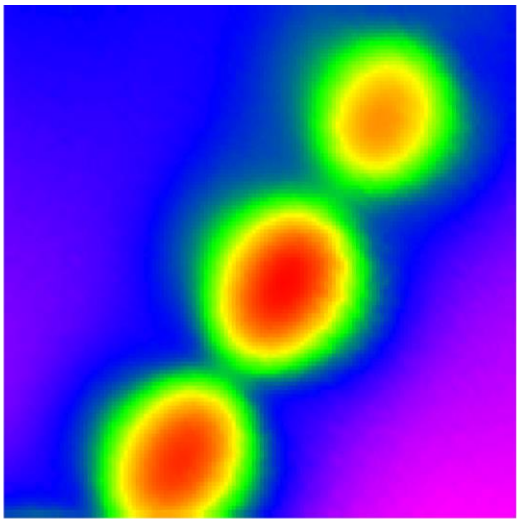

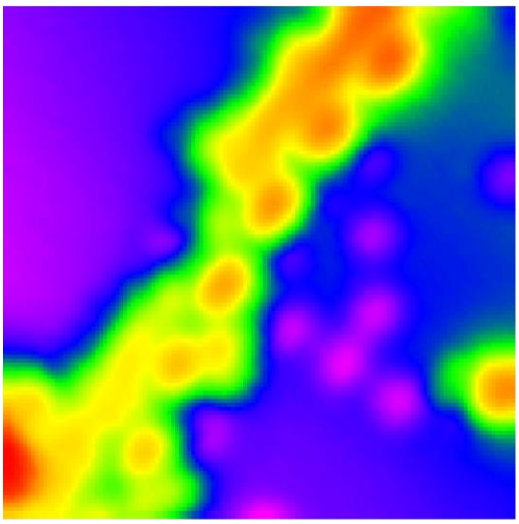

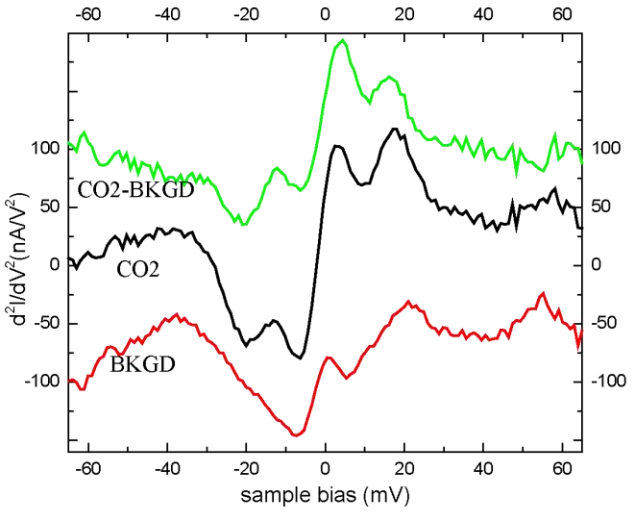
-60
-40
-20
0
20
40
60
100
50
0
-50
-100
CO2-BKGD
CO2
BKGD
d²I/dV²(nA/V²)
sample bias (mV)


low
high

`

Fig 4.3 STM topographic images and H_2 IETS image at low H_2 coverage, (A) 20Å×20 Å STM topography image taken at V_B=23.4mV, I_T=0.2nA, (B) 21.75Å×21.75 Å STM topography image taken at V_B=5mV, I_T=0.2nA, (C) 21.75Å×21.75 Å IETS image taken at V_B=5mV, I_T=0.2nA, (D) ball-stick model of single PDI molecule.

`

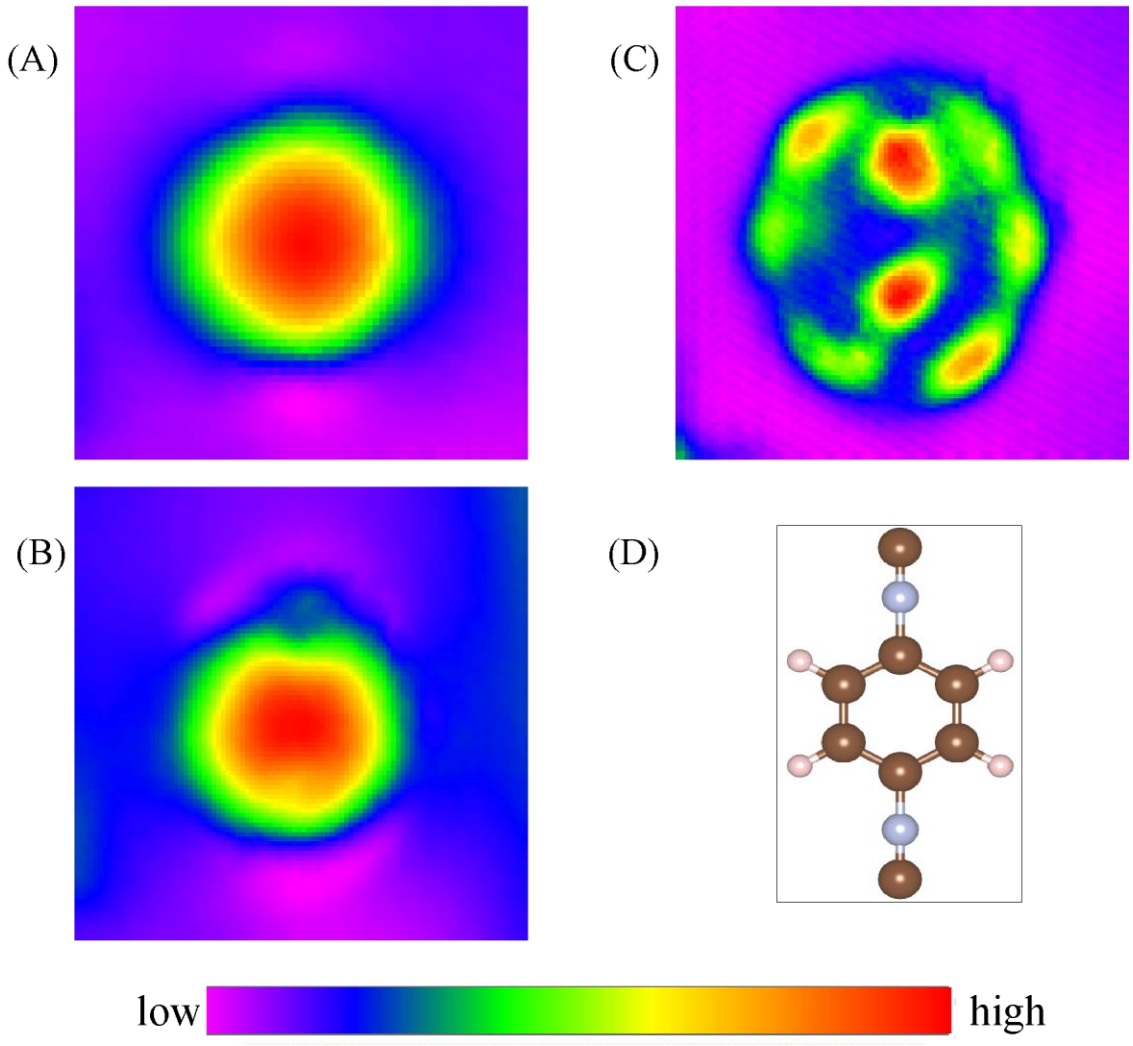
(A)
(C)
(B)
(D)
low
high

`

Fig 4.4 H_2 IETS spectra on different points of the molecule at low H_2 coverage, (A) 21.75Å×21.75 Å STM topography image taken at V_B=5mV, I_T=0.2nA, (B) 21.75Å×21.75 Å IETS image taken at V_B=5mV, I_T=0.2nA, (C) IETS spectra on different points of the molecule, the tunneling set point is at V_B=65mV, I_T=2.5nA.

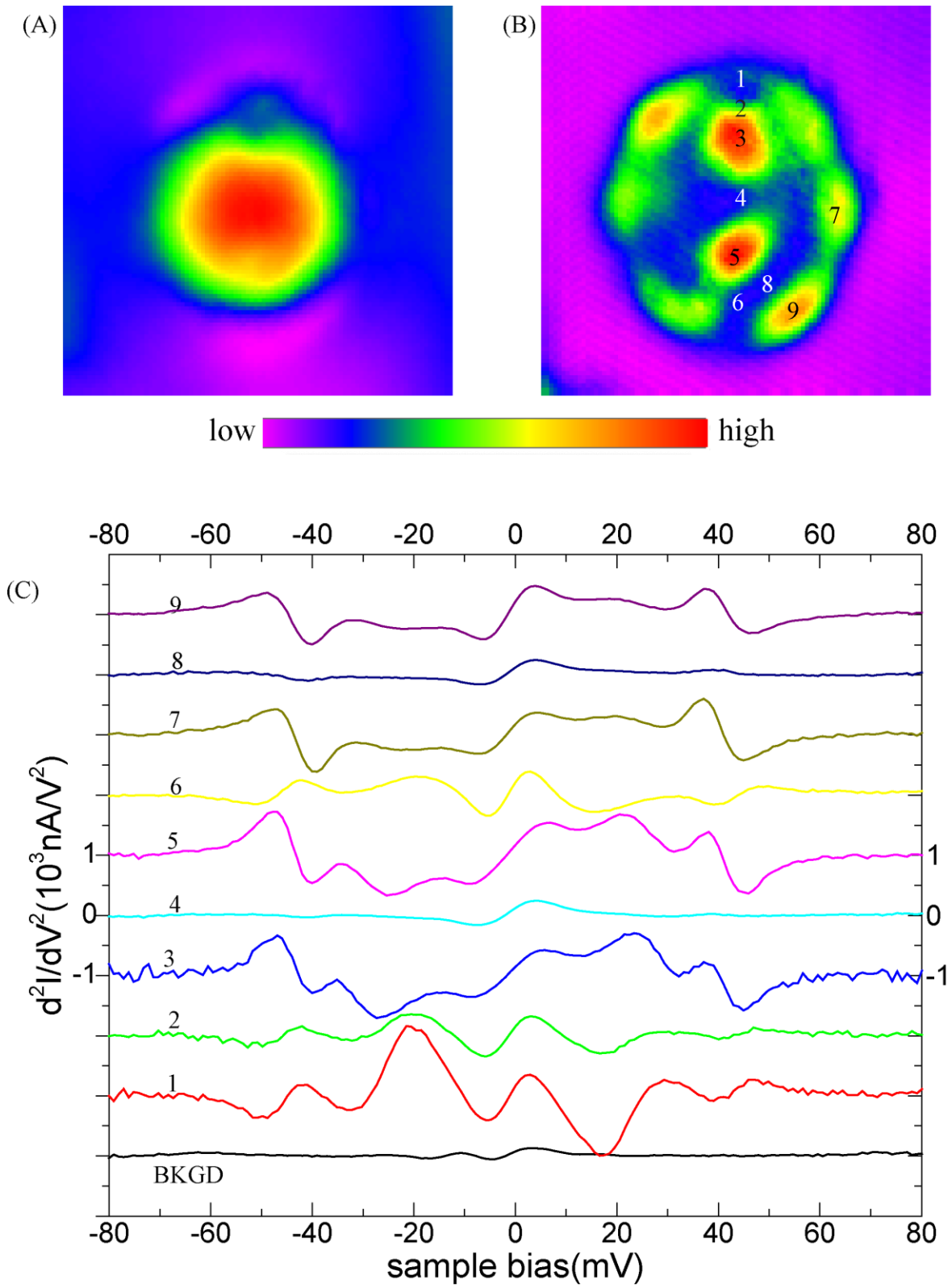
(A)
(B)
1
2
3
4
5
6
7
8
9
low
high
(C)
-80
-60
-40
-20
0
20
40
60
80
9
8
7
6
5
4
3
2
1
BKGD
d²I/dV²(10³nA/V²)
sample bias(mV)

`

Fig 4.5 STM topography images and H_2 IETS image at high H_2 coverage, (A) 17.5Å×17.5 Å STM topography image taken at V_B=65mV, I_T=0.15nA, (B) 17.5Å×17.5Å STM topography image taken at V_B=5mV, I_T=0.2nA, (C) 21.75Å×21.75 Å IETS image taken at V_B=-8.8mV, I_T=0.2nA, (D) ball-stick model of single PDI molecule.

`

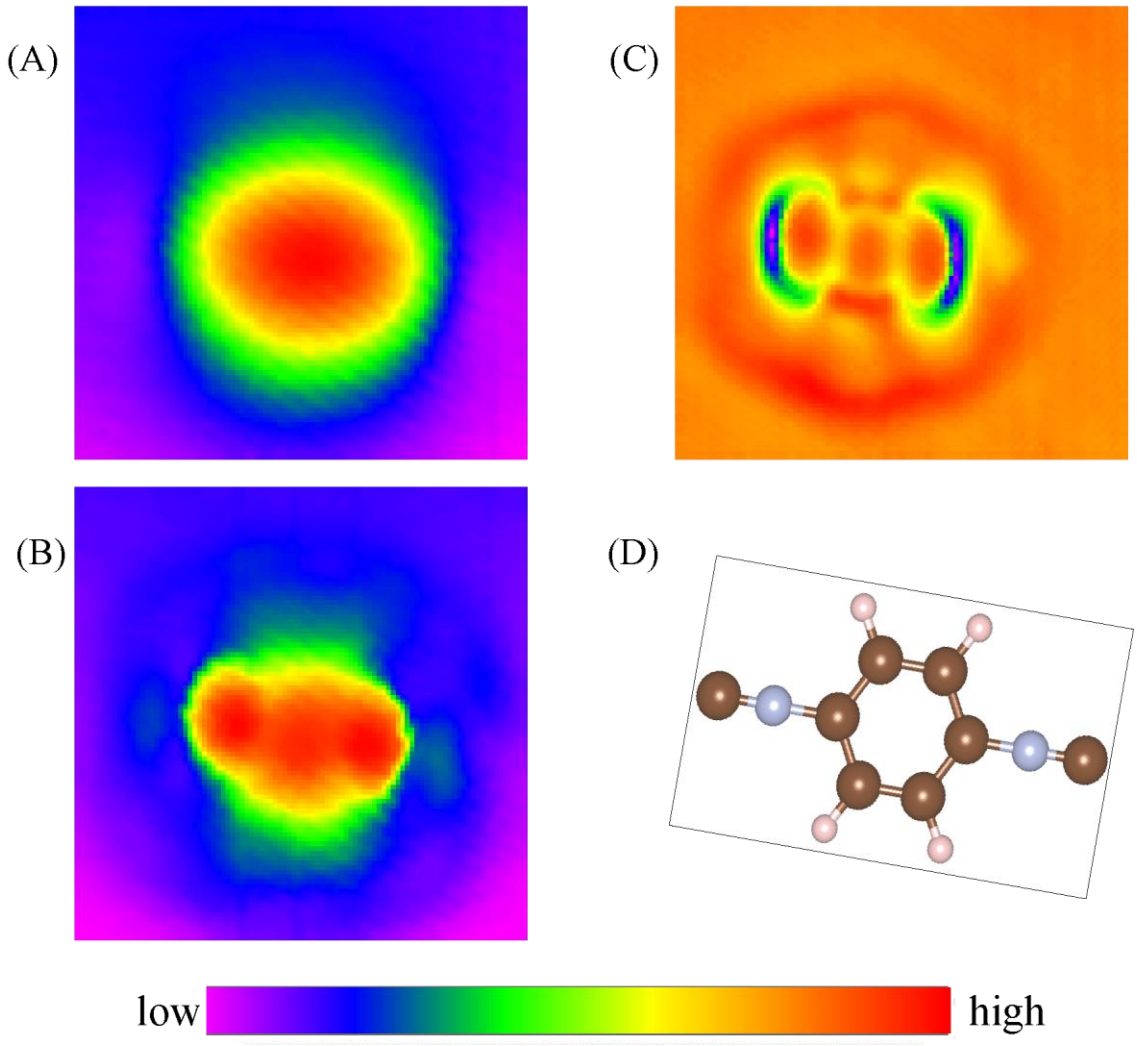
(A)
(C)
(B)
(D)
low
high

`

Fig 4.6 H_2 IETS spectra on different points of the molecule, (A) 21.75Å×21.75 Å STM topography image taken at V_B=-8.8mV, I_T=0.2nA (B) 21.75Å×21.75 Å IETS image taken at V_B=-8.8mV, I_T=0.2nA, (C) IETS spectra on different points of the molecule, the tunneling set point is at V_B=65mV, I_T=2.5nA.

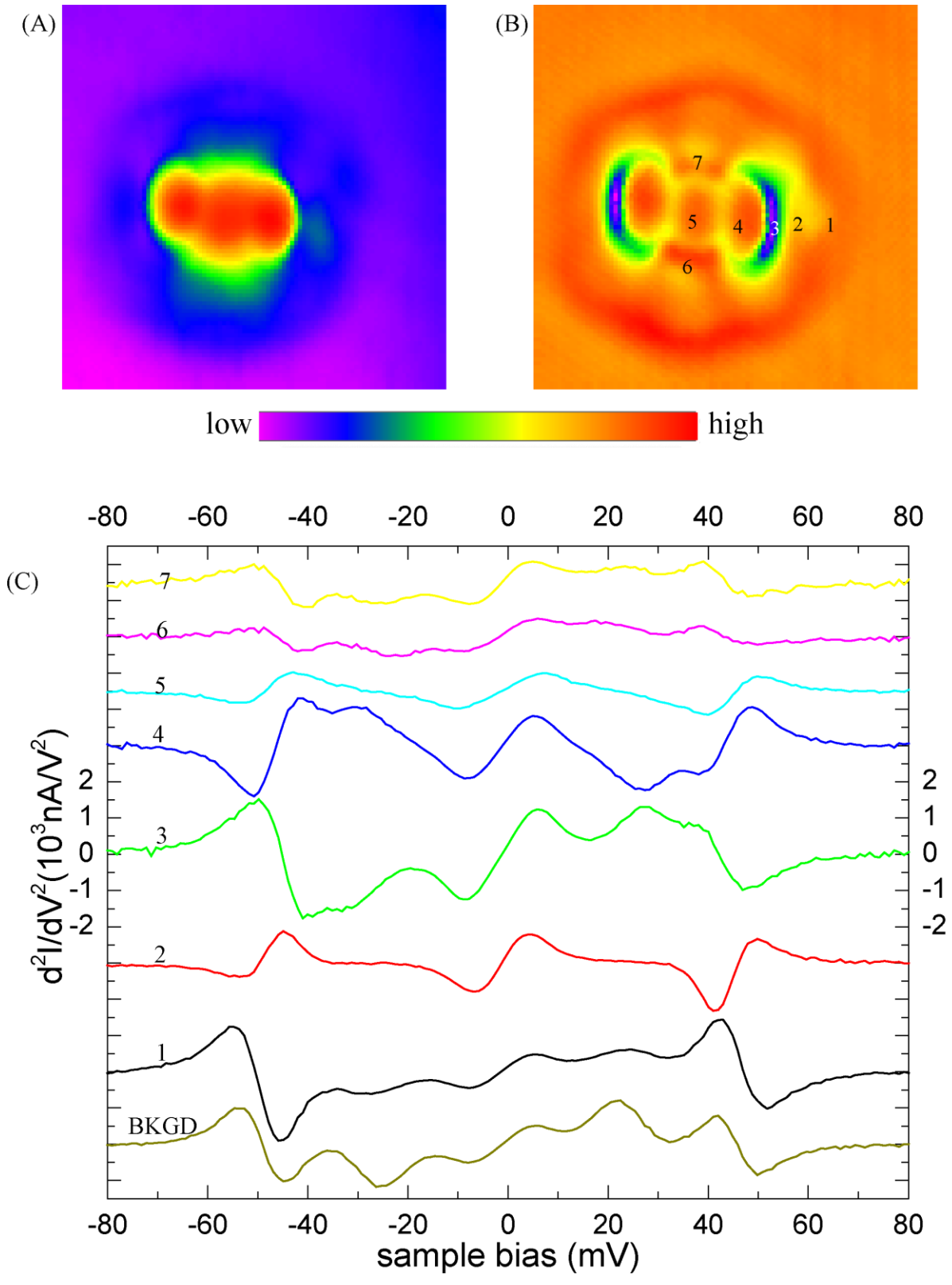
(A)
(B)
7
5
4
3
2
1
6
low
high
(C)
-80
-60
-40
-20
0
20
40
60
80
7
6
5
4
3
2
1
BKGD
2
1
0
-1
-2
d²I/dV²(10³nA/V²)
sample bias (mV)

`

Fig 4.7: H_2 IETS image at different setpoints, (A) 21.75Å×21.75 Å IETS image taken at V_B=5.1mV, I_T=0.2nA, (B) 21.75Å×21.75 Å IETS image taken at V_B=48.1mV, I_T=1.92nA, (C) 21.75Å×21.75 Å IETS image taken at V_B=-8.8mV, I_T=0.2nA, (D) 21.75Å×21.75 Å IETS image taken at V_B=39.1mV, I_T=1.5nA.

`

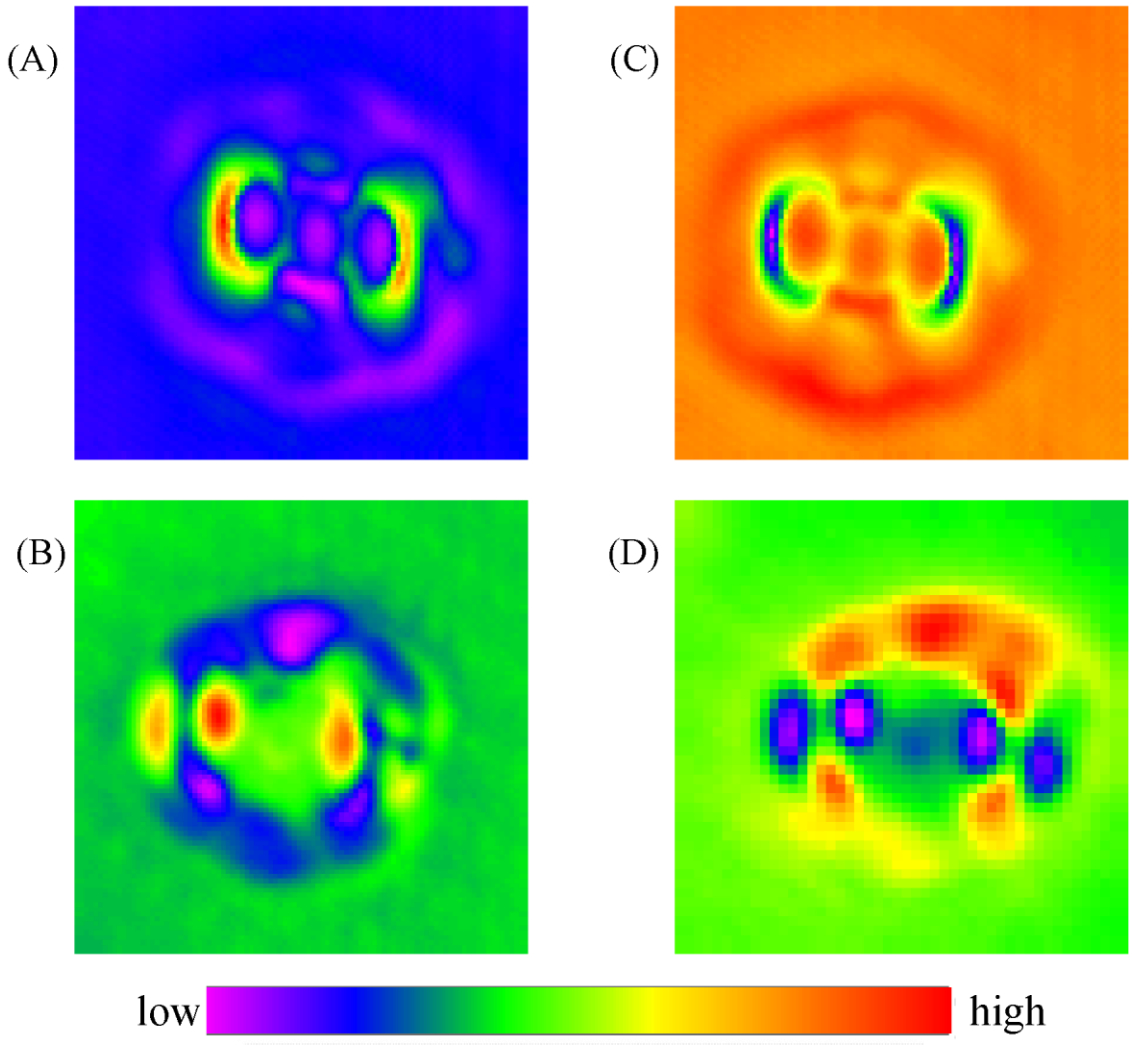
(A)
(C)
(B)
(D)
low
high

`

Fig 4.8: (A) 58Å×58 Å STM topography image taken at V_B=50mV, I_T=0.18nA, (B) 20Å×20Å IETS image taken at V_B=10mV, I_T=1.75nA, (C) 17Å×17Å IETS image taken at V_B=42.5mV, I_T=0.05nA, (D) 17Å×17 Å IETS image taken at V_B=-4.2mV, I_T=0.25nA.

`

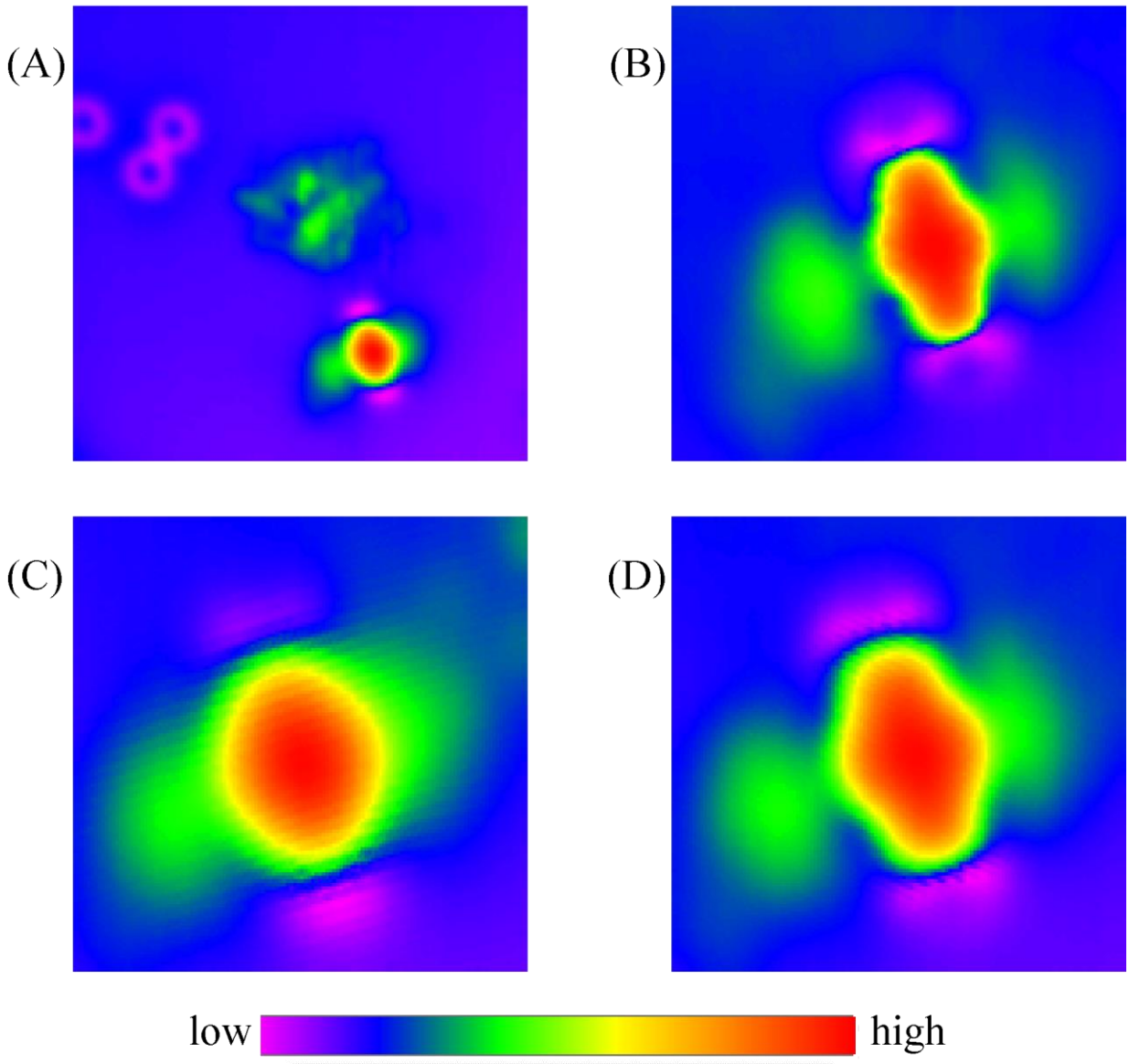
(A)
(B)
(C)
(D)
low
high

`

Bibliography

1. "Single-molecule Chemistry", W. Ho, *J. Chem. Phys.* **117**, 11033-11061 (2003).
2. "Single Molecule Vibrational Spectroscopy and Microscopy", B. C. Stipe, M. A. Rezaei, W. Ho, *Science* **262**, 218-220(1998).
3. "Direct Imaging of Intermolecular Bonds in Scanning Tunneling Microscopy", C. Weiss, C. Wagner, R. Temirov, and F. S. Tautz, *J. Am. Chem. Soc.* **132**, 11864 (2010).
4. "Real-Space Imaging of Molecular Structure and Chemical Bonding by Single-Molecule Inelastic Tunneling Probe", C. L. Chiang, C. Xu, Z. Han and W. Ho, *Science* **344**, 885-888(2014).
5. "Rotational Spectromicroscopy: Imaging the Orbital Interaction between Molecular Hydrogen and an Adsorbed Molecule", S. Li, D. Yuan, A. Yu, G. Czap, R. Wu and W. Ho, *Phys. Rev. Lett.* **114**, 206101 (2015).
6. "Single-Molecule Rotational and Vibrational Spectroscopy and Microscopy with the Scanning Tunneling Microscope", A. Yu, S. Li, G. Czap and W. Ho, *J. Phys. Chem. C*, **119**, 14737-14741 (2015).
7. "The Chemical Structure of a Molecule Resolved by Atomic Force Microscopy", L. Gross, F. Mohn, N. Moll, P. Liljeroth and G. Meyer, *Science* **325**, 1110-1114(2009).
8. "Creation of Low-Coordination Gold Sites on Au (111) Surface by 1, 4-Phenylene Diisocyanide Adsorption", J. Boscoboinik, J. Kestell, M. Garvey, M, Weinert and W. T. Tysoe, *Top Catal* **54**, 20-25 (2011).
9. "Understanding and Controlling the 1,4-Phenylene Diisocyanide-Gold Oligomer Formation Pathways", M. Garvey, J. Kestell, R. Abuflaha, D. W. Bennett, G. Henkelman and W. T. Tysoe, *J. Phys. Chem. C.* **118**, 20809-20907 (2014).

`

10. “Adsorption Structures and Electronic Properties of 1, 4-Phenylene Diisocyanide on the Au (111) Surface”, J. Zhou, D. Acharya, N. Camillone III, P. Sutter and M. G. White, *J. Phys. Chem. C.* **115**, 21151-21160 (2011).
11. “Self-Catalyzed Carbon Dioxide Adsorption by Metal-Organic Chains on Gold Surfaces”, M. Feng, H. Sun, J. Zhao, and H. Petek, *ACS Nano* **8**, 8644-8653(2014).
12. W. Cao, C. J. Patel, M. Feng, S. Tan, H. Petek and W. Ho, to be published.
13. S. Tan, M. Feng and H. Petek, to be published.
14. “Electronic Transport through Metal-1,4-Phenylene Diisocyanide-Metal Junctions”, J. Chen, L.C. Calvet, M.A. Reed, D.W. Carr, D.S. Grubisha and D.W. Bennett, *Chem. Phys.Lett.* **313**, 741-748 (1999).
15. “Plasmonic Effects of Phenylenediisocyanides Linked at Interparticle Junctions of Metal Nanoparticles”, E. López-Tobar, K. Hara, I. Lzquierdo-Lorenzo, and S. Sanchez-Cortes, *J. Phys. Chem. C.* **119**, 599-609 (2015).
16. “Electronic Transport Calculations for Self-Assembled Monolayers of 1,4-Phenylene Diisocyanide on Au(111) surface”, R. Dahlke and U. Schollwöck, *Phys. Rev. B.* **69**, 085324 (2004).
17. “Rotational and Vibrational Excitations of a Hydrogen Molecule Trapped within a Nanocavity of Tunable Dimension”, S. Li, A. Yu, F. Toledo, Z. Han, H. Wang, H. Y. He, R. Wu and W. Ho, *Phys. Rev. Lett.* **111**, 146102 (2013).
18. “Distinction of Nuclear Spin States with the Scanning Tunneling Microscope”, F. D. Natterer, F. Patthey and H. Brune, *Phys. Rev. Lett.* **111**, 175303 (2013).

`

19. “A Variable-temperature Scanning Tunneling Microscope Capable of Single-molecule Vibrational Spectroscopy”, B. C. Stipe, M. A. Rezaei, W. Ho, *Rev. Sci. Instrum*. **70**, 137−143 (1999).

20. W. Cao, C. J. Patel, G. C. Welch, G. C. Bazan and W. Ho, to be published.

`

Chapter 5

Exploration of New Oxide Surfaces and Study of Molecules in Various Chemical Environments

5.1 Abstract

Molecules on oxide surfaces are particularly challenging to characterize due to limitation on the amount of current that can be used due to the weak adsorption energy. If too much tunneling current is used or the tunneling gap is too small, the molecule can be perturbed and either move or desorb from the surface. For STM, the oxide needs to be thin (< 10 Å) and is grown on a metal substrate by oxidation. Still the thin oxide provides electronic decoupling from the underlying metal substrate that sharpens the electronic states of the molecule. Thus it is possible to detect molecular orbitals and image their spatial distribution. An effort was spent to get partially oxidized (Al_2O_3) on the clean NiAl (110) surface, with about half oxide coverage and large Al_2O_3 islands, C_{60}, azulene, alizarin molecules were studied on this surface. A monolayer of CuO has been grown on Cu (110) surface, Cu/CuO stripe structure is also formed, allow the simultaneous investigation of molecules on both metal and oxide surfaces, C_{60} and CO molecules are studied on this surface.

5.2Introduction

Many metals found in nature are covered with an oxide. Oxides are known to exhibit different chemical and physical properties, as well as different composition, stoichiometry, and structure.

`

In interfacial electron transfer, oxides provide electronic isolation of the metal substrate and lowest lying conduction band that can accept photogenerated electrons from the molecules. For these reasons, it is desirable to investigate different oxides.

5.2.1 Al_2O_3/NiAl (110)

NiAl has simple cubic crystal structure, with Ni sits in the corners and Al sits in the center (CsCl prototype). It has good physical properties (low density: 5.85g cm^{-3}, high melting point: 1638C, high thermal conductivity, etc.) to be a material in aerospace industry. But its mechanical properties (lack of high fracture toughness and high temperature strength) limited its use now [1, 2]. Since the first report of the formation of ultrathin well-ordered Al_2O_3 layer (5Å) by oxidation of NiAl [3], it plays a key role in many technologies, like serving as stable supports for metal clusters [4] and an STM decoupling layer [5]. However, the microscopic structure of this thin film is still not clear. In the first paper of Freund, they use different electronic spectroscopy technologies to investigate of the structure of the thin film. Their LEED data shows that Al_2O_3 thin film contains distorted hexagonal oxygen layers and the oxygen-oxygen spacing is larger than that of bulk Al_2O_3. Their XPS and AES data show that the thickness of the film is 5Å; the thickness is compatible with two bilayers consisting of an aluminum layer and a quasi-hexagonal oxygen layer. Their EELS data suggest the structure is mostly likely similar to α-Al_2O_3 (0001) or γ-Al_2O_3 (111) [3]. There is no evidence showing the Ni-O interactions (NiO or $NiAl_2O_4$) or Ni existing in the Al_2O_3–NiAl interface, the Ni atoms dissolved into the bulk NiAl during annealing process at around 1250K (the diffusion coefficient is high enough at this temperature for Ni diffuse into bulk). The fact that the Al_2O_3 layer is chemically inert to most molecules up to 800K leads to the presumption that the thin film is oxygen terminated since electronic structure of O^{2-} is near to that of rare gas, so that the sequence of the layer is NiAl-Al-

`

O-Al-O. Later, this group took out the Al_2O_3/NiAl sample from the UHV chamber and studied with TEM, the data supported the γ-Al_2O_3 (111) structure [6].

Stierle et al. reported their detailed study of the Al_2O_3/NiAl structure using an extended surface x-ray diffraction (SXRD), which allows them to derive an atomically resolved structure model. The distorted double layer of hexagonal O ions act as building blocks for the film and the Al ions host on distorted octahedral or tetrahedral sites. Uncoordinated Al ions are located in the oxide/metal interface to fulfill the stoichiometry. The resulting structure is closely related to bulk κ- Al_2O_3, which was shown both in theory and experiment before. They also show the atomic positions within the structure [7]. Later, Kresse et al. found that the short bond lengths (Al-Al 2.08 Å, Al-O 1.51 Å) in the structure that Stierle reported are unstable in their ab initio calculations. Since they observed square features in STM image, they explained them by a square arrangement of O atoms. The topmost Al atoms are pyramidally and tetrahedrally coordinated. The stacking consequence of the thin film is 4($Al_4O_6Al_6O_7$) and the stoichiometry is $Al_{10}O_{13}$, different from commonly Al_2O_3. The oxide unit cell covers 16 NiAl substrate unit cell. They propose the same building blocks can be found on surfaces of bulk oxides [8].

Researchers are also interested in the grain boundary structure of the thin Al_2O_3 film. The Freund group studied the structure with STM to determine the atomic structure of the antiphase domain boundaries of the thin Al_2O_3 film, APDB result from the insertion of an oxygen row but do not induce change in the geometric height, the apparent corrugation of APDB in STM images at certain biases must arises from the electronic properties of these dislocations [9]. Combining STM images and DFT calculations, Kresse et al. derived a model of APDB of Al_2O_3/NiAl. It indicates that the structure is O deficient; two Al 3p electrons fail to find the corresponding empty O conduction band states, the O-deficient domain boundary acts as a native electron

`

donor. By transferring these electrons to the NiAl support, an insulating surface layer will be restored [10].

5.2.2 CuO/Cu (110)

Molecular Oxygen is long-time known to dissociatively chemisorb on the Cu (110) surface and forms the 2×1 structure at O coverage of 0.5 monolayer [11]. Different techniques including EELS, LEIS, photoemission, XRD, He diffraction, etc. have been used to study the structure, all these studies conclude that O chemisorbed on the long bridge site (along the <100> direction), but the detailed atomic geometry remains controversial for 20 years, based on different experiments, "buckled-row model" and "missing-row model" have been suggested [12, 14]. In early 1990's, with the STM experiments of nucleation, structure and growth of p(2×1)O-Cu(110), it's clear that this new phase is formed by reaction of chemisorbed O atoms with the Cu atoms evaporated from the step edges and diffused across terraces, the structure is an "added-row" type [12, 13, 14]. The oxygen-induced p (2×1) O-Cu (110) has been attracted much interest for the past two decades after the structure gets clear. One great advantage of this surface over Al_2O_3/NiAl(110) is the much smaller unit cell and the surface atoms can be imaged, thus the clusters, molecules and atoms on this surface has a more uniform and well-defined chemical environment surrounded. For STM experiments, it's also served as a magnetic insulator [15] and one dimensional substrate [16].

Besides the 2×1 structure, there are some other kinds of chemisorbed O induced reconstruction, most notably c (6×2) O [17].

5.3 Experiments and Discussion

The aluminum oxide and CuO are formed and different molecules are studied on the oxide surfaces with the homemade STM.

`

The preparation of NiAl (110) surface and aluminum oxide patches is modified from previous procedures [5]. The sample holders are modified, adding sapphire hemispheres and rings between sample holder and NiAl sample [18], enabling the NiAl sample annealed at higher temperature ~1200℃, at such a high temperature, sputtering is not necessary to get a clean metal surface. Partial crystalized oxide patches are formed on a clean NiAl(110) surface by 240L oxidation (120s at 2×10^{-6} torr) at ~530℃ followed by annealing at 1050℃ for 7 mins. Furthermore, full crystalized aluminum oxide surface can be formed by 550L oxidation at ~530℃ (275s at 2×10^{-6} torr) followed by annealing 1050℃ for 7 mins (fig 5.1).

The Cu (110) surface is cleaned by sputter (0.5kV Ne beam) anneal (480℃) cycles, some defects still remain on the surface (fig5.5 A). The p (2×1) O-Cu (110) is formed by 3L oxidation (150s at 2×10^{-8} torr) at ~300℃. The oxide looks uniform without any defects (fig 5.5 B and fig 5.5 C). Cu/CuO stripes can also be formed by smaller amount O_2 oxidation or annealing the full oxide surface, but the metal looks kind of amorphous. Also, the Cu stripe + CuO stripe width is limited to 6~14nm [19], without the big terraces, molecules prefer to absorb on metal or edge between Cu and CuO (fig 5.7 B).

Electrochemically etched Ag tips which are in-situ cleaned before the experiments are used in these experiments.

5.3.1 Molecules on Al_2O_3/NiAl (110)

C_{60} is a well-studied molecule with vibronic features [20] and can be superconductor with alkali metal doped [22]. In our experiments, C_{60} is evaporated onto the Al_2O_3/NiAl (110) surface at room temperature, all molecules adsorb on NiAl at this temperature even though the molecules also go to oxide at 10K [20, 21]. A full oxide surface is formed to get the molecules onto the oxide (fig 5.1). The C_{60} layer looks different on metal and on the oxide (fig 5.1 A, B and C), the

`

plan was to study the life time of the vibronic states of the C_{60} layer by shining fs laser [20]. K was also doped for study of superconductivity [22]. For all these experiments, L He is needed to cool the molecules down to 10K; however, they were not possible given the shortage of L He at the time these experiments were performed.

Azulene is a molecule with unique electronic and photoelectric properties [23]. With 193 nm photon absorption, the azulene molecules will first convert to its isomer naphthanlene and then dissociate to smaller molecules [24]. Here, we shine 220nm fs laser into the STM junction, multiphoton at this energy can also covert the molecule to naphthanlene and dissociate. Fig 5.3 (A) shows the azulene molecules look uniform before shining the 220nm fs laser beam, after shining the laser, smaller species appears as shown in fig 5.3(B), probably due to photo isomerization and photo dissociation. Smaller species also show up on the oxide after shining fs laser as shown in fig 5.3(C) and fig 5.3(D). The goal next will be studying the photochemistry at single molecule level and characterizing the dissociated products with a CO tip at 10K.

Alizarin (1, 2-dihydroxyanthraquinone) is an organic red dye that is used for dying textile fabrics and is an abundant material for dye sensitized solar cells. The molecules are thermally evaporated onto the Al_2O_3/NiAl (110) surface at 10K. Fig 5.4 shows the STM topography images and dI/dV spectra of three molecules on the oxide, the topography images show the LUMO geometry when scanned near the LUMO peak, the dI/dV spectrum from 0 to 1.6V show the LUMO peak(s) around 1V, however, only the molecule on the grain boundary shows the HOMO peak. Molecule 2 disappears after taking the spectrum. More molecules need to be studied to confirm these data. The ultimate goal of this project is to study the electron transfer between the molecule and TiO_2. Also the alizarin molecule may stand up on the surface for fs laser simulated Raman experiments [25].

`

5.3.2 Molecules on CuO/Cu (110)

CO is evaporated onto the CuO/Cu (110) surface at 13.5K, CO prefers to go to the metal surface, given the metal surface is kind of amorphous, it's hard to tell individual CO molecules apart and some CO molecules do not look round (fig 5.7 A and B). However CO looks big protrusions on CuO surface and they form 1D chain (fig 5.5 B and D). The hindered rotational mode of CO on CuO has slight blue shift [26]; it's also possible to pick up CO from the oxide. However, it's easy to see H_2 signal on the CuO surface without introducing any H_2 into the UHV chamber. With such strong H_2 IETS background, it's hard to see IETS modes from other molecules like CO, NO or O_2.

C_{60} is also thermally evaporated onto the CuO/Cu (110) surface at room temperature, different from the layers that C_{60} forms on Al_2O_3/NiAl (110) (fig 5.2), they form clusters on CuO instead (fig 5.6A). Mg is thermally evaporated onto the C_{60}/CuO surface; Mg prefers the C_{60} clusters than the CuO. Individual Mg atoms could be imaged on the C60 clusters if the coverage is low (fig 5.7 B and C). With more Mg evaporated onto the surface, the Mg fully covers around the C_{60} clusters instead of adsorbing on CuO. MgC_{60} is a semiconductor used in solar cell [27]; investigating the number and site dependence of dosed Mg on C_{60} upon electronic structure may help improve the structure, furthermore, time-resolved study of charge transfer could be performed by combining fs laser with STM.

4T-BTD and alizarin are also evaporated onto the Cu/CuO stripes, the molecules prefers the metal or the edge.

`

5.4 Conclusions

Large aluminum oxide islands are formed on NiAl (110) surface by modifying previous recipes. CuO is formed on Cu (110) surface with well-defined structure. STM imaging and spectroscopy are performed on molecules (including C_{60}, azulene, alizarin and CO) adsorbed on Al_2O_3 and CuO surfaces. The thin oxide provides electronic decoupling from the underlying metal substrate that sharpens the electronic states of the molecule, the oxide can also elongate the lifetime of excited states of adsorbed molecules.

Acknowledgements

This work is supported by the National Science Foundation Center for Chemical Innovation at the Space-Time Limit (CaSTL) under Grant No. CHE-1414466. We thank M. Mecartney, F. Toledo and Z. Han for stimulating discussions.

`

Fig 5.1: partial and full oxide at room temperature, (A) 2000Å×2000Å STM topography images of partial oxide on NiAl (110) surface, V_B=2V, I_T= 0.10nA, oxide is on the left and metal is on the right, the lines are grain boundaries, (B) 2000Å×2000Å STM topography images of partial oxide on NiAl (110) surface, V_B=2V, I_T= 0.10nA, oxide is in the middle and the two sides are metal, (C) 2000Å×2000Å STM topography images of full oxide on NiAl (110) surface, V_B=3V, I_T= 0.10nA, (D) 2000Å×2000Å STM topography images of full oxide on NiAl (110) surface, V_B=3V, I_T= 0.10nA.

`

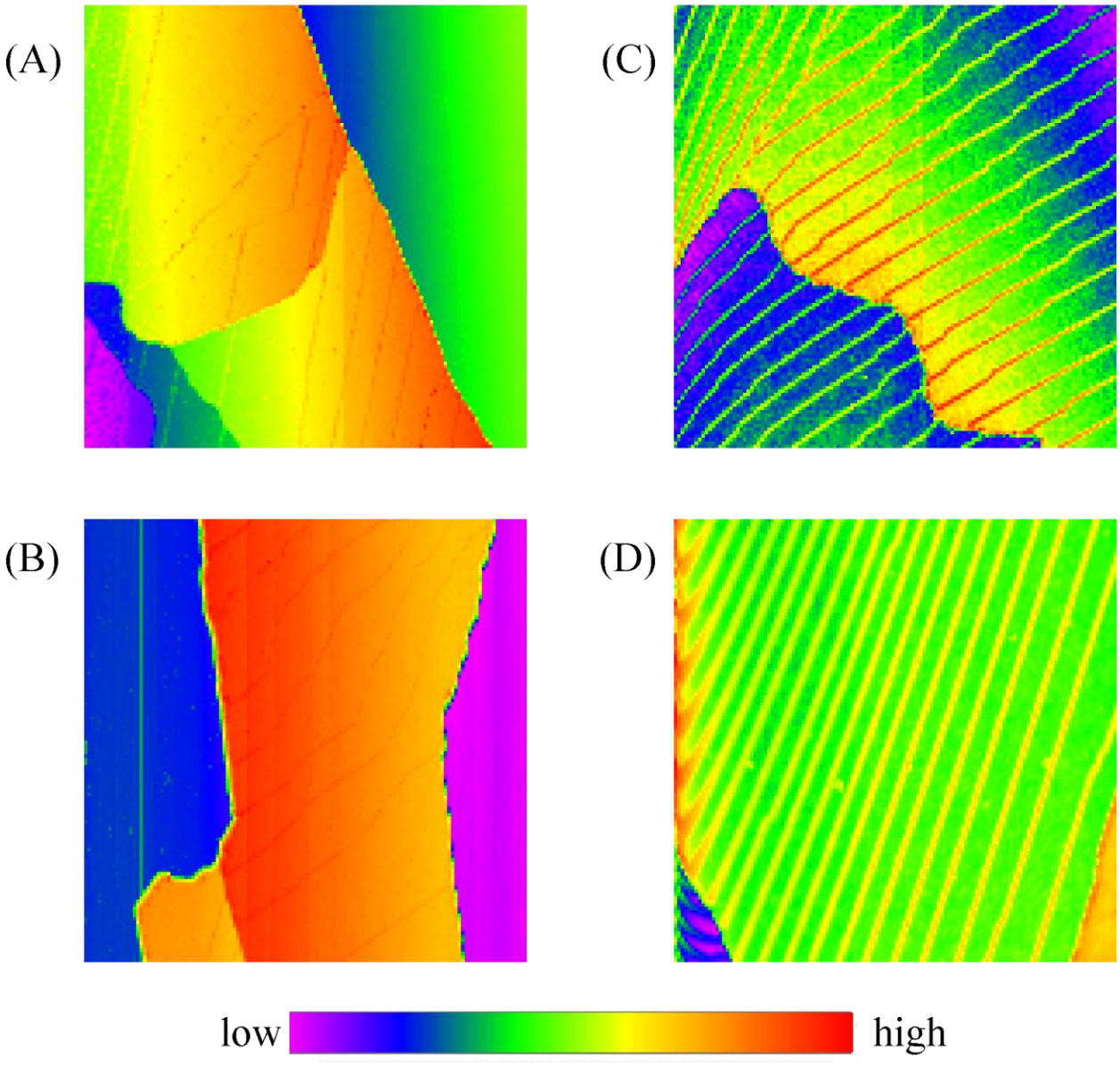
(A)
(C)
(B)
(D)
low
high

`

Fig 5.2: STM topography images of C_{60} adsorbed on Al_2O_3/NiAl (110), the C_{60} is thermally evaporated onto the surface at room temperature and the experiments are performed at 84K, all images are 125Å×125Å at V_B=2.5V, I_T= 0.10nA, (A) C_{60} layer on metal, (B) C_{60} layer on oxide (C) irregular layer on oxide, (D) K on C_{60} layer on oxide.

`

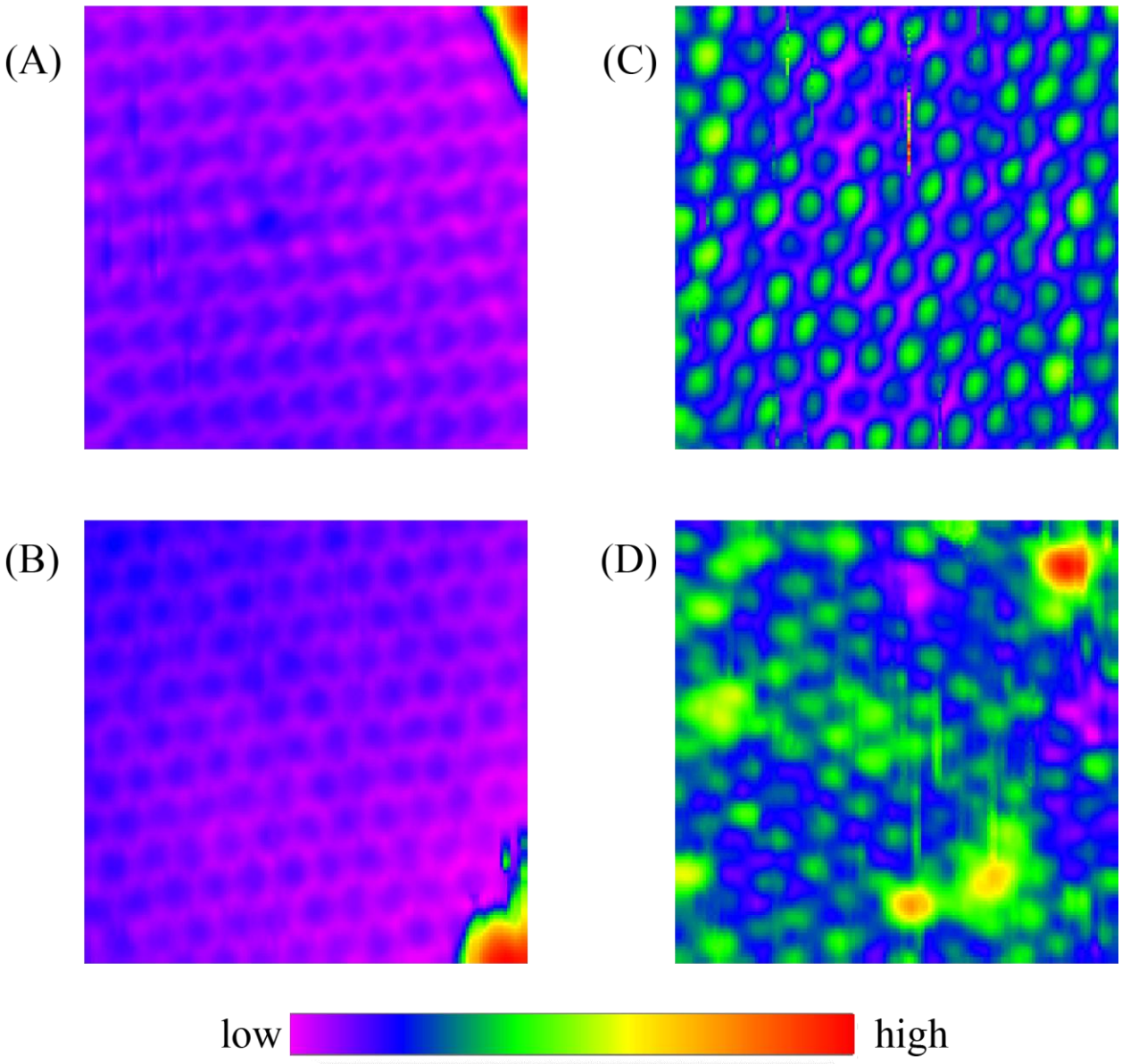
(A)
(C)
(B)
(D)
low
high

`

Fig 5.3: STM topography images of azulene on Al_2O_3 and NiAl(110) before and after 220nm fs laser irradiation, all the images are 250Å×250Å, (A) on NiAl before laser irradiation, V_B=1.00V, I_T= 0.10nA, (B) on NiAl after laser irradiation, V_B=1.50V, I_T= 0.10nA, (C) on oxide before laser irradiation, V_B=1.50V, I_T= 0.10nA, (D) on oxide after laser irradiation, V_B=1.50V, I_T= 0.10nA.

`

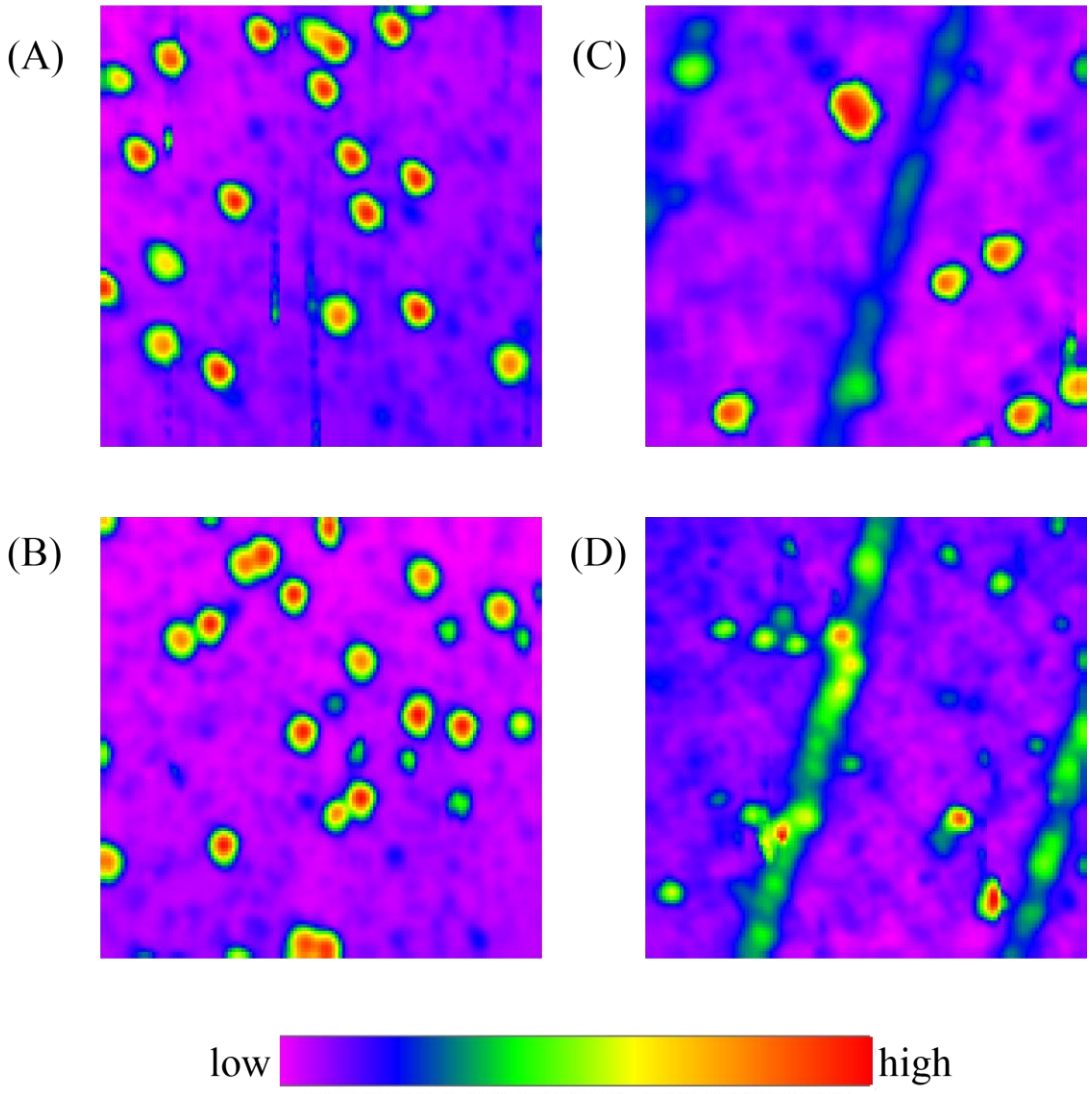
(A)
(C)
(B)
(D)
low
high

`

Fig 5.4: STM topography images and spectroscopy of alizarin on Al_2O_3 at 13.5K, (A) 87Å×87Å STM topography images of three alizarin molecules on Al_2O_3/NiAl, V_B=1.5V, I_T= 0.10nA, (B) 87Å×87Å STM topography images of two alizarin molecules on Al_2O_3/NiAl, V_B=1.5V, I_T= 0.10nA, molecule 2 disappear during spectroscopy, (C) dI/dV spectroscopy of the molecules from 0V to 1.6V, the tunneling gap is set at V_B=1.5V, I_T= 0.10nA, (D) dI/dV spectroscopy of the molecules from -1.6V to 0V, the tunneling gap is set at V_B=1.5V, I_T= 0.10nA.

`

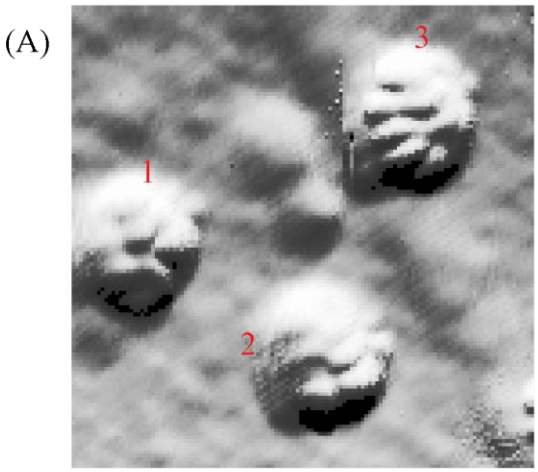
(A)
1
2
3

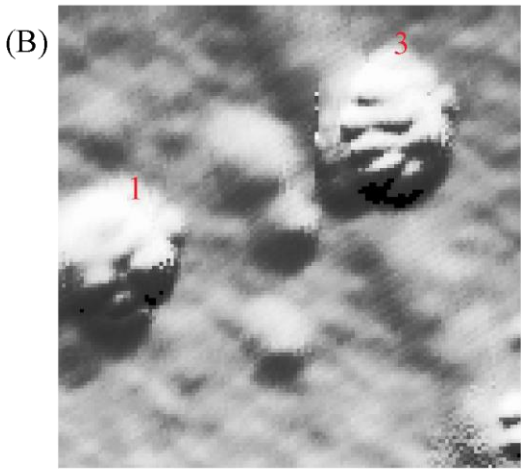
(B)
1
3

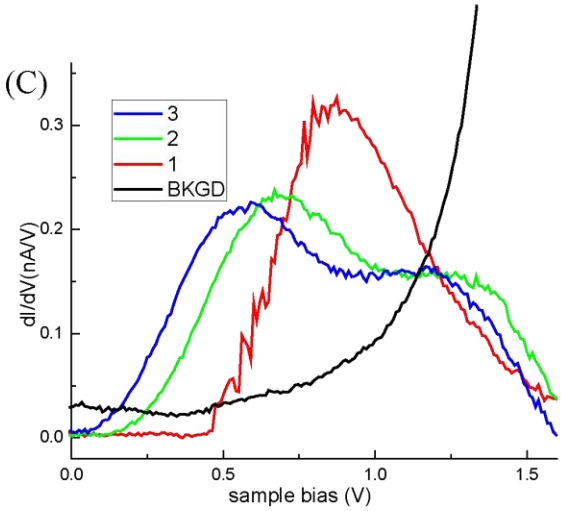
(C)
3
2
1
BKGD
dI/dV(nA/V)
sample bias (V)
0.0
0.1
0.2
0.3
0.5
1.0
1.5

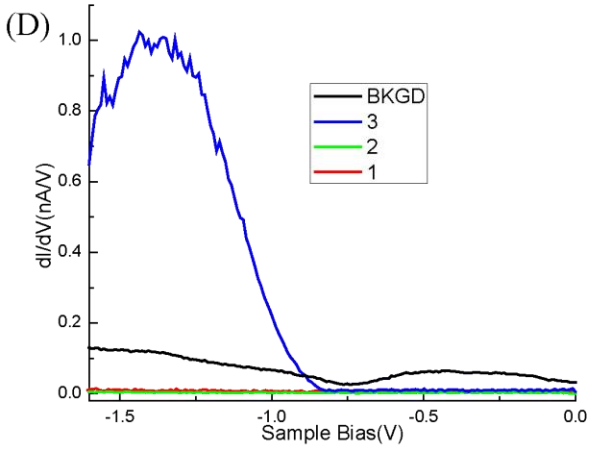
(D)
BKGD
3
2
1
dI/dV(nA/V)
Sample Bias(V)
0.0
0.2
0.4
0.6
0.8
1.0
-1.5
-1.0
-0.5
0.0

`

Fig 5.5: (A) 500Å ×500Å STM topography image taken at V_B=-3V, I_T=0.12nA on Cu (110) at room temperature, (B) 58Å ×58Å STM topography image taken at V_B=0.1V, I_T=0.1nA on CuO at 12.5K, with a CO on the surface, (C) 17.5Å ×17.5Å STM topography image taken at V_B=0.5V, I_T=0.8nA on CuO at 12.5K, (D) 58Å ×58Å STM topography image taken at V_B=-0.5V, I_T=0.1nA of CO chains on CuO at 12.5K.

`

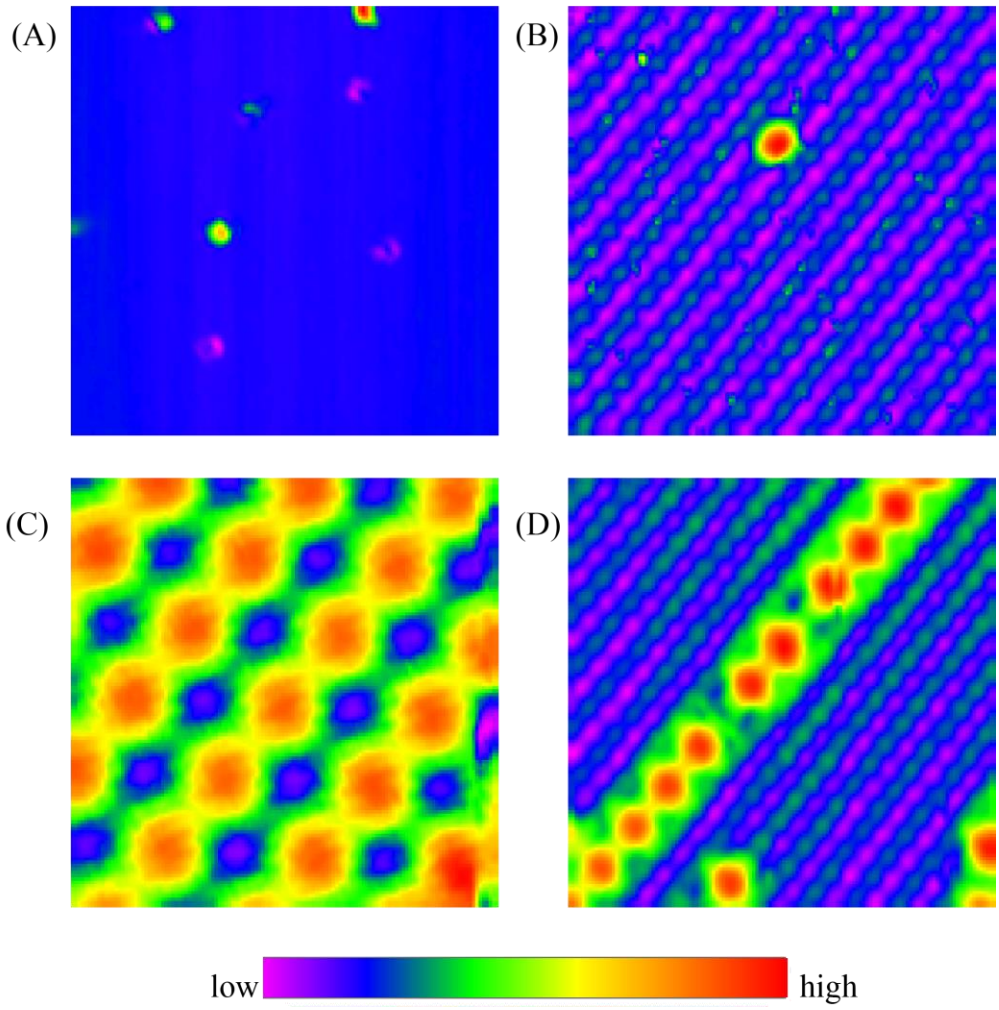
(A)
(B)
(C)
(D)
low
high

`

Fig 5.6: STM topography image of C_{60} and MgC_{60} on CuO/Cu(110) surface, (A) 500Å ×500Å STM topography image taken at V_B=2.05V, I_T=0.12nA on CuO at room temperature, the clusters are formed by C_{60}, which are thermally evaporated onto the surface, (B) 1000Å ×1000Å STM topography image taken at V_B=2.05V, I_T=0.12nA on CuO at room temperature, with Mg evaporated on C_{60}/CuO, the individual dots are Mg, (C) 500Å ×500Å STM topography image taken at V_B=2.05V, I_T=0.13nA with Mg on C_{60}/CuO at room temperature, (D) 250Å ×250Å STM topography image taken at V_B=1.08V, I_T=0.12nA with more Mg on C_{60}/CuO.

`

(A)

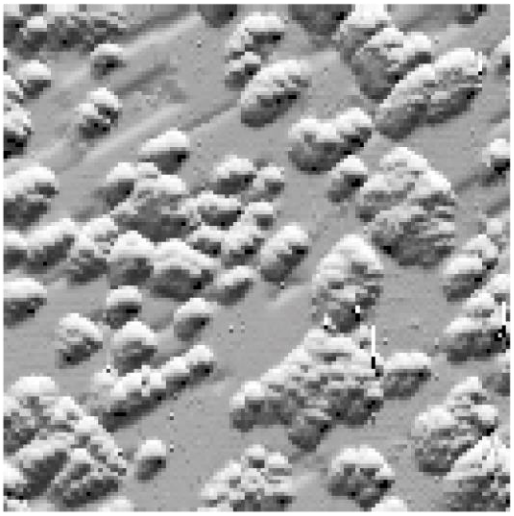

(B)

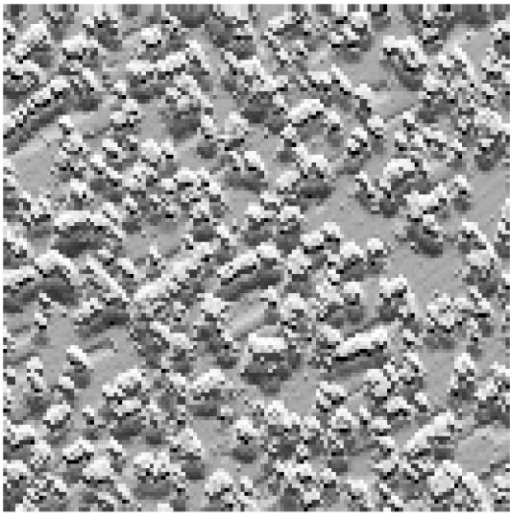

(C)

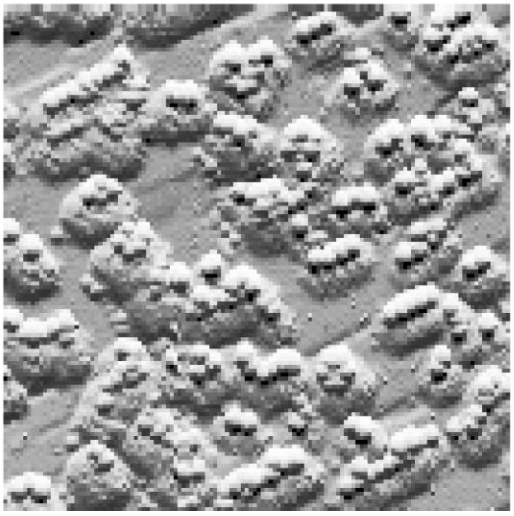

(D)

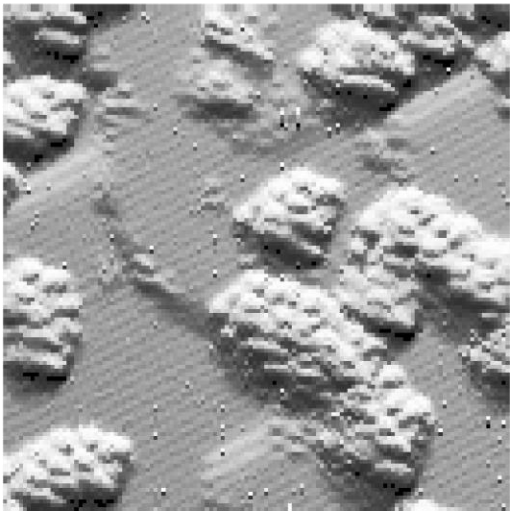

`

Fig 5.7: (A) 464Å ×464Å STM topography image taken at V_B=0.6V, I_T=0.1nA on CuO/Cu at 13.5K, (B) 116Å ×116Å STM topography image taken at V_B=0.6V, I_T=0.1nA on CuO/Cu at 13.5K, (C) 81Å ×81Å STM topography image taken at V_B=37mV, I_T=0.5nA on CuO/Cu at 13.5K, (D) 81Å ×81Å STM topography image taken at V_B=37mV, I_T=0.5nA on CuO/Cu at 13.5K.

`

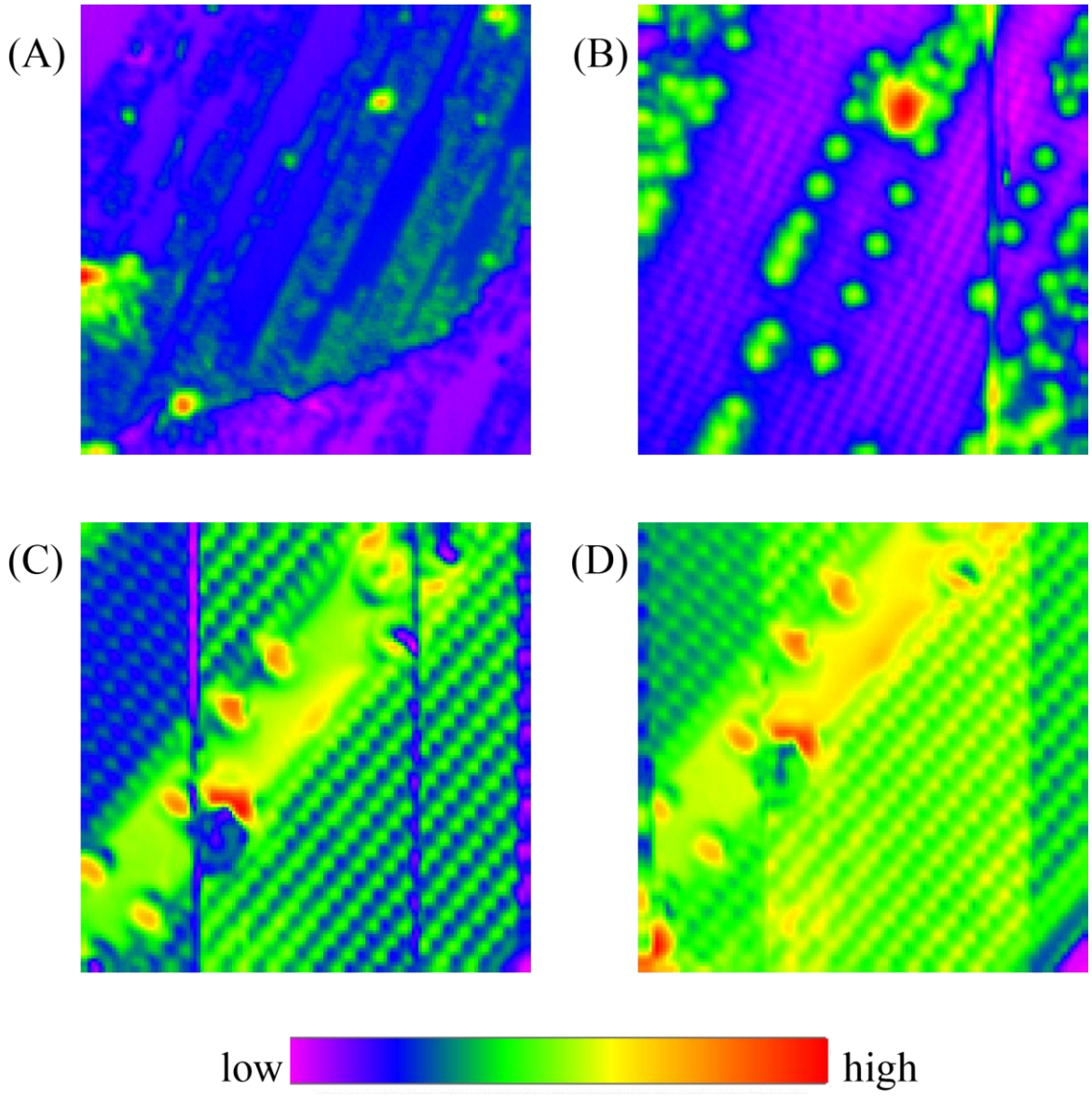
(A)
(B)
(C)
(D)
low
high

`

Bibliography

1. "NiAl and Its Alloys", D. B. Miracle and R. Darolia (Ch. 3); pp. 53–72 in Intermetallic Compounds, Vol. 2. Edited by J. H. Westbrook and R. L. Fleischer. Wiley, New York, 1994.
2. "Toughening and Strengthening of NiAl with Al_2O_3 by the Addition of ZrO_2 (3Y)", A. Kitaoka, K. Hirota et al. *J. Am. Ceram. Soc.* **83**, 1311-1313 (2000).
3. "Formation of a well-ordered aluminum oxide overlayer by oxidation of NiAl (110)", R.M. Jaeger, H.-J. Freund, H. Ibach et al, *Surf. Sci.* **259**, 235-252 (1991).
4. "Inflence of the metal substrate on the adsorption properties of thin oxide layers Au atoms on a thin alumina film on NiAl (110)", M. Kulawik, N. Nilius, and H.-J. Freund, *Phys. Rev. Lett.* **96**, 036103 (2006)
5. "Vibrationally Resolved Fluorescence Excited with Submolecular Precision", X. H. Qiu, G. V. Nazin, W. Ho, *Science* **299**, 542-546(2003).
6. "Transmission Electron Microscopic investigation of an ordered Al_2O_3 film on NiAl", M. Klimekov, H.-J. Freund et al, *Surf. Sci.* **385**, 66-76 (1997).
7. "X-ray Diffraction Study of the Ultrathin Al_2O_3 Layer on NiAl (110)", A.Stierle, F. Renner, et al, *Science* **303**, 1652-1656(2004).
8. "Structure of the Ultrathin Aluminum Oxide Film on NiAl(110)" G. Kresse et al, *Science* **308**, 1440-1442 (2005).
9. "Atomic Structure of Antiphase Domain Boundaries of a Thin Al_2O_3 Film on NiAl(110)", M. Kulawik, H.-J. Freund et al, *Phys. Rev. Lett.* **91**, 256101 (2003).
10. "Oxygen-deficient line defects in an ultrasthin aluminum oxide film", M. Schmid, G. Kresse et al, *Phys. Rev. Lett.* **97**, 046101 (2006).

`

11. “Untersuchung von oberflächenreaktionen mittelsbeugung langsamer elektronen (LEED): I. Wechselwirkung von O_2 und N_2O mit (110)-, (111) - und (100)-Kupfer-Oberflächen”, G. Ertl, *Surf. Sci.* **6**, 208-232 (1967).
12. “Oxygen Chemisorption on Cu (110): An Atomic View by Scanning Tunneling Microscopy”, F.M. Chua, Y. Kuk and P.J. Silverman, *Phys. Rev. Lett.* **63**, 386-389 (1989).
13. “Novel Mechanism for the formation of Chemisorption Phases: The (2×1)O-Cu(110) “Added-Row” Reconstruction”, D.J. Coulman, J. Wintterlin, R.J. Behm, and G. Ertl, *Phys. Rev. Lett.* **64**, 1761-1764 (1990).
14. “Surface Reconstruction of Cu(110) Induced by Oxygen Chmisorption ”, F. Jensen, F. Besenbacher, E. Lægsgaard, and I. Stensgaard, *Phys. Rev. B.* **41**, 10233-10236 (1990).
15. “Adsorption-Induced Switching of Magnetic Anisotropy in a Single Iron(II) Phthalocyanine Molecule on an Oxidized Cu(110) Surface”, N. Tsukahara, M. Kawai et al, *Phys. Rev. Lett.* **102**, 167203 (2009).
16. “Orthogonal Interactions of CO Molecules on a One-Dimensional Substrate”, M. Feng, H. Petek et al, *ACS Nano* **5**, 8877-8883(2011).
17. “An STM Investigation of Cu(110)-c(6×2)O System”, D. Coulman, J. Wintterlin, J. V. Barth and G. Ertl, *Surf. Sci.* **240**, 151-162 (1990).
18. Freddy Toledo, PhD thesis, UC Irvine, 2013.
19. “Long-Range Spatial Self-Organization in the Adsorbate-Induced Restructuring of Surfaces: Cu{110}-(2×1)O”, K. Kern, H. Niehus, A. Schatz, P. Zeppenfeld, J. Goerge and G. Comsa, *Phys. Rev. Lett.* **67**, 855-858 (1991).
20. “Vibronic States in Single Molecules: C_{60} and C_{70} on ultrathin Al_2O_3 Films”, N. Liu, N.A. Pradhan and W. Ho, *J. Chem. Phys* **120**, 11371-11375 (2004).

`

21. “Tuning the Bipolar Conductance of a Alkali-Doped C_{60} Layer Sandwiched between Two Tunneling Barriers”, N. A. Pradhan, N. Liu, C. Silien, and W. Ho, *Nano Lett.* **5**, 55-59(2005).

22. “Superconductivity in Alkali-doped C_{60}”, A. P. Ramirez, *Physica C* **514**, 166-172(2015).

23. “Colorful Azulene and Its Equally Colorful Derivatives”, R. S. H. Liu, *J. Chem. Edu* **79**, 183-185 (2002).

24. “Photodissociation Dynamics of Azulene”, M-F. Lin, C-L. Huang, Y. T. Li and C-K. Ni, *J. Chem. Phys.* **119**, 2032-2036 (2003).

25. Original data from Peter Lu’s Group at Bowling Green State University, OH.

26. Original data from H. G. Zhang and H. K. Lee.

27. “Mg-doped C60 Thin Film as Improved n-type Organic Semiconductor for a Solar Cell”, M. Chikamatsu, T. Taima, Y. Yoshida, K. Saito and K. Yase, *Appl. Phys. Lett.* **84**, 127-129 (2004).

`

Chapter 6

Imaging and Electronic Spectrum of Fe Nanoclusters on Al_2O_3/NiAl (110) at Various Temperatures with a Laser-STM

6.1 Abstract

Fe nanoclusters are grown by thermally evaporating Fe onto Al_2O_3/NiAl (110) surface at room temperature and ~84K. At room temperature, Fe prefers to absorb on the NiAl (110) surface and can grow into islands/films with enough coverage on metal, sparse Fe nanoclusters are grown on the oxide. At 84K, Fe grows into size-limited nanoclusters on both Al_2O_3 and NiAl (110) surface; still with less coverage on oxide. The nanoclusters on oxides are bigger than the ones on metal, with increasing Fe coverage, the number of nanoclusters on both metal and oxide will increase instead of forming islands/thin films on NiAl (110), DC and RF spectroscopy are performed on the nanoclusters on Al_2O_3 and NiAl (110) at 84K. Furthermore, the nanoclusters are annealed to form larger ones, the larger clusters are cooled down to ~21K and dI/dV spectroscopy is performed on the clusters.

6.2 Introduction

Metal films and particles on oxide surfaces are of great importance in many technological applications including heterogeneous catalysis [1, 2], spintronic devices [3] and photovoltaic devices [4]. In this work we focus on the creation of small iron clusters on a thin oxide film serving as a model system to investigate the catalytic, magnetic and optical properties of

`

nanosized metallic particles on an insulating substrate. Fe nanoclusters on oxide have been proposed to have potential applications such as catalysis [3] and spintronics [4].

The Scanning Tunneling Microscope (STM) has been a powerful tool to study nanoscience by imaging and electronic spectroscopy [5]. Different metal nanoclusters adsorb on thin oxide film grown on metal substrates can be studied with a STM [1]. Fe clusters adsorb on MgO thin film grown on Ag (100) [6] and alumina thin film grown on Ni_3Al (111) [7, 8] have been characterized with STM imaging. Theoretical studies are also carried out to study the magnetic properties [9] and catalytic behaviors [2] of Fe clusters supported on oxide. However, electronic properties of the Fe nanoclusters have only been studied on the metal Au (111) surface [10], but not on the oxide surfaces. Nanoclusters on oxide surfaces are particularly challenging to characterize the electronic properties due to limitation on the amount of current. Electronic properties of single atoms and molecules have been characterized on 5Å alumina thin film grown on NiAl (110) surface [11, 12]. In this work, electronic properties of Fe nanoclusters on oxide Al_2O_3/NiAl (110) are studied at 84K and 21K.

6.3 Experiment

The experiments were performed using a home-built STM operating at various temperatures from 21K to room temperature and a base pressure of 3×10^{-11} Torr [13]. The preparation of NiAl (110) surface and aluminum oxide patches is modified from previous procedures [11, 12], the NiAl sample was annealed at higher temperature ~1200℃, the partial crystalized oxide patches are formed on a clean NiAl(110) surface by 240L oxidation (120s at 2×10^{-6} torr) at ~530℃ followed by annealing at 1050℃ for 7 minutes. The Ag tip was electrochemically etched and in-situ cleaned before experiments. The Fe is thermally evaporated onto the surface at room

`

temperature or 84K and forms nanoclusters on the oxide. Electronic properties are studied by performing dI/dV spectrum on the nanoclusters. Moreover, with 220nm laser shining into the junction, DC dI/dV spectroscopy and RF dI/dV spectroscopy with double lock-in technique are also performed. The nanoclusters grown on the surface at room temperature are annealed to ~600C to get bigger size nanoclusters; the bigger nanoclusters are cooled to 21K to perform electronic properties studies.

6.4 Results and Discussion

For comparison, Fe clusters and thin films on NiAl (110) metal surface are also studied. Fe is evaporated onto the clean NiAl (110) surface (fig 6.1 A) at room temperature. At small coverage, the Fe will first saturate on the step edges, and then small clusters are grown on the terraces (fig 6.1 B). With enough coverage, layers of Fe films are grown from step edges (fig 6.1 C and D). For the partial 5Å oxide crystalized patches covered Al_2O_3/NiAl (110) surface, Fe prefers to absorb on the NiAl (110) surface and grown into islands, sparse Fe nanocluster could be found on the oxide with enough dosage.

With the Al_2O_3/NiAl (110) surface cooled down to 84K, Fe grows into size-limited nanoclusters on both oxide and metal; more clusters could be found on the metal. The size of the Fe nanoclusters are different on the metal (~2nm) from the ones on oxide (~3nm) (fig 6.3 A and B). Different from the layers or islands of Fe film grown on NiAl (110) at room temperature, more Fe nanoclusters are grown on both oxide and metal if more Fe is dosed (fig 6.3C). A dimer of Fe clusters on oxide is shown if fig 6.3 D, the clusters are even more crowded on the metal.

Electronic properties of the clusters are measured by performing dI/dV spectroscopy with the lock-in technique. From the dI/dV spectrum on the Fe nanocluster in fig 6.4A on NiAl (110),

`

the cluster has a peak at 2.2V (fig 6.4B). With 220nm fs laser shining into the junction, DC dI/dV spectroscopy is performed, the 2.2V peak slightly shifts to ~2.3V. On the negative bias side, the dI/dV signal is dominated by the photoemission from sample to tip. The dI/dV signal in and out of tunneling on both Fe nanocluster and NiAl (110) background is measured (fig 6.4C). All the spectra have two peaks around ~-0.8V and 0.5V, with slightly different peak position and intensity especially for the -0.8V peak. Furthermore, the DC and ~80MHz laser induced RF signal can be separated by using an external bias tee, the RF signal is fed into a 200MHz lock-in, the output of 200 MHz lock-in amplifier is fed into a second lock-in amplifier that detects a lower frequency signal generated by modulating the sample bias, for dI/dV and d^2I/dV^2 spectroscopy. The dI_{RF}/dV spectrum on the Fe nanocluster at tunneling has ~1V peak, very similar to the background dI_{RF}/dV at tunneling. While the noise spectrum without laser is without any peaks and the ~1V peak on dI_{RF}/dV spectra out of tunneling (on cluster and background) are less obvious.

Same measurements are performed on nanoclusters deposited on oxide (fig 6.5), the dI/dV spectrum on the oxide background has no peaks from -2V to 2V since the oxide film has a band gap at this range (fig 6.5B). Besides the peak at 2.2V, two other peaks at 1.2V and -1.1V on the nanocluster are also observed (fig 6.5B and fig 6.5D). With 220nm fs laser in the junction, the 2.2V peak shifts to 2.3V, suggesting possible laser induced effects on the electronic states of the nanocluster. The dI_{RF}/dV spectra on the nanocluster and the oxide background are noisier than the ones on metal NiAl (110), the DC dI/dV with laser on is also dominated by photoemission, the peak position is similar to NiAl, but not so sharp.

To get bigger size nanoclusters, the clusters deposited at RT are annealed to 600℃. Fe islands are grown on metal even at small coverage, the clusters on oxide are grown bigger to

`

~4nm on oxide, during annealing, some clusters diffuse to grain boundaries so more clusters can be found there (fig 6.6). The annealed sample is cooled to 21K and electronic properties of Fe clusters on oxide are studied (fig 6.7). Fig 6.7A shows one cluster has peaks at ~2.2V, ~1.2V and ~-1.1V; while there are no peaks on the other cluster. Fig 6.7B shows the electronic spectra on different points of the dimer, the peak energy and intensity vary on different points.

6.5 Conclusions

In conclusion, Fe clusters are formed and investigated on Al2O3/NiAl (110) surface with STM. Fe thin films are formed on metal surface at room temperature while sparse cluster can be formed on oxide. At 84K, clusters are both formed on oxide and metal surfaces. Bigger Fe cluster can be formed by annealing the sample to high temperature. Electronic properties are studied at 84K and 21K, DC and RF dI/dV spectra are also studied with 220nm fs laser in junction. For most of the Fe clusters formed and investigated at 84K, there is a DC dI/dV peak around ~2V. For most of the bigger clusters investigated at ~20K, other states besides the 2V are observed. With laser shining, a small shift of 2V peak in DC dI/dV spectra is detected; suggesting some laser induced effect on electronic states. DC dI/dV spectra on the negative bias with laser shining are dominated by the photoemission from sample to tip. RF dI/dV spectra with the double lock-in technique are noisy although some differences on nanocluster and background are recorded.

`

Acknowledgements

This work is supported by the National Science Foundation Center for Chemical Innovation at the Space-Time Limit (CaSTL) under Grant No. CHE-1414466, we thank M. Mecartney and R. Ragan for stimulating discussions.

`

Fig 6.1: Fe nanocluster and films on NiAl(110) at room temperature, (A) 1000Å×1000Å STM topography image taken at V_B=2.0V, I_T=0.11nA, (B) 2000Å×2000Å STM topography image taken at V_B=2.05V, I_T=0.11nA, (C) 1000Å×1000Å STM topography image taken at V_B=2.05V, I_T=0.11nA, (D) 250Å×250Å STM topography image taken at V_B=1.08V, I_T=0.13nA.

`

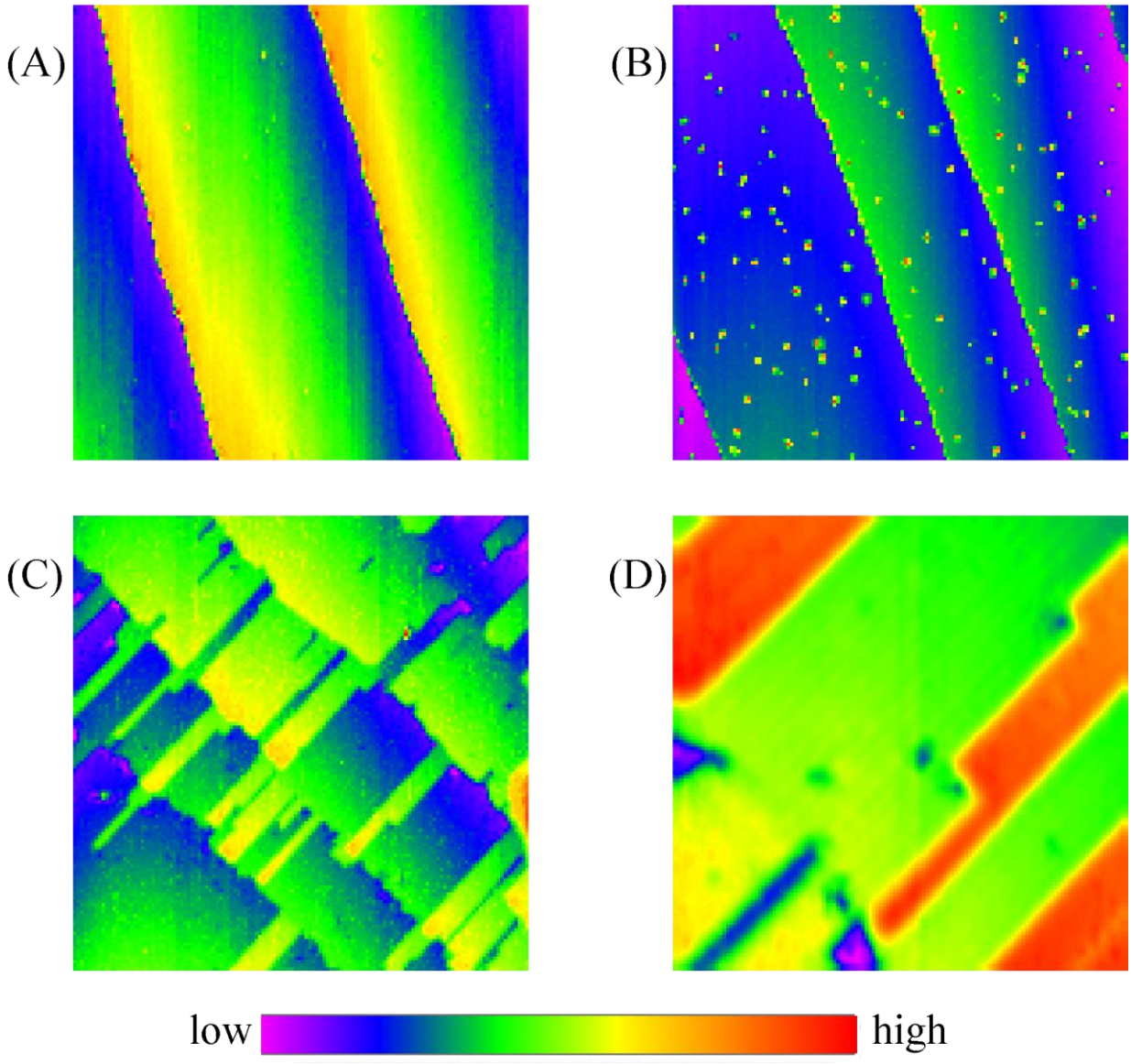
(A)
(B)
(C)
(D)
low
high

`

Fig 6.2: Fe clusters and islands on Al_2O_3/NiAl (110) surface at room temperature, (A) 4000Å×4000Å STM topography image taken at V_B=2.0V, I_T=0.10nA, (B) 2000Å×2000Å STM topography image taken at V_B=2.05V, I_T=0.10nA, (C) 1000Å×1000Å STM topography image taken at V_B=2.05V, I_T=0.10nA, (D) 1000Å×1000Å STM topography image taken at V_B=2.05V, I_T=0.10nA.

`

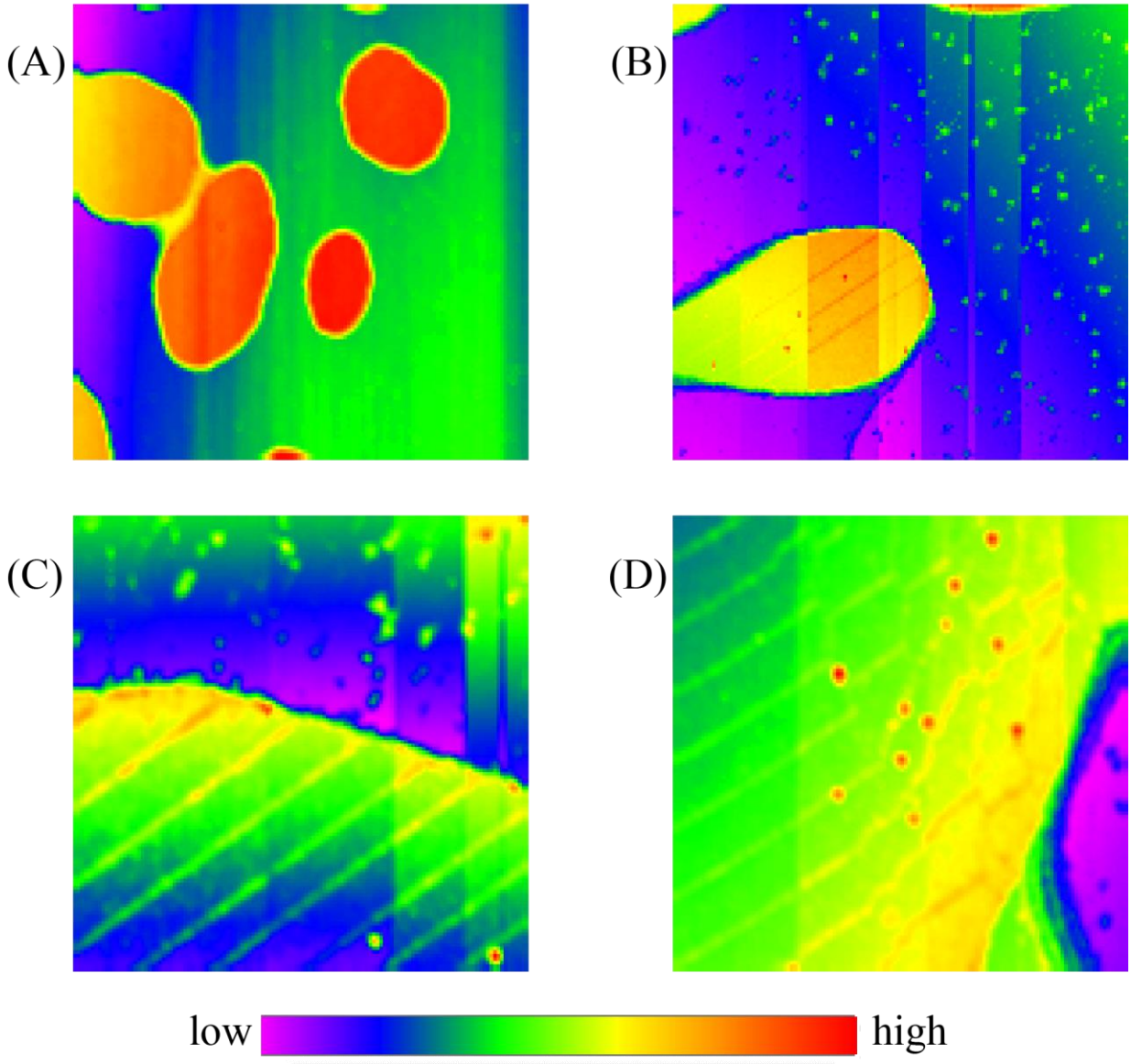
(A)
(B)
(C)
(D)
low
high

`

Fig 6.3: Fe clusters on Al_2O_3/NiAl (110) at 84K, (A) 250Å×250Å STM topography image taken at V_B=1.08V, I_T=0.10nA, (B) 250Å×250Å STM topography image taken at V_B=2.00V, I_T=0.10nA, (C) 250Å×250Å STM topography image taken at V_B=2.50V, I_T=0.12nA, (D) 62Å×62Å STM topography image taken at V_B=2.00V, I_T=0.10nA.

`

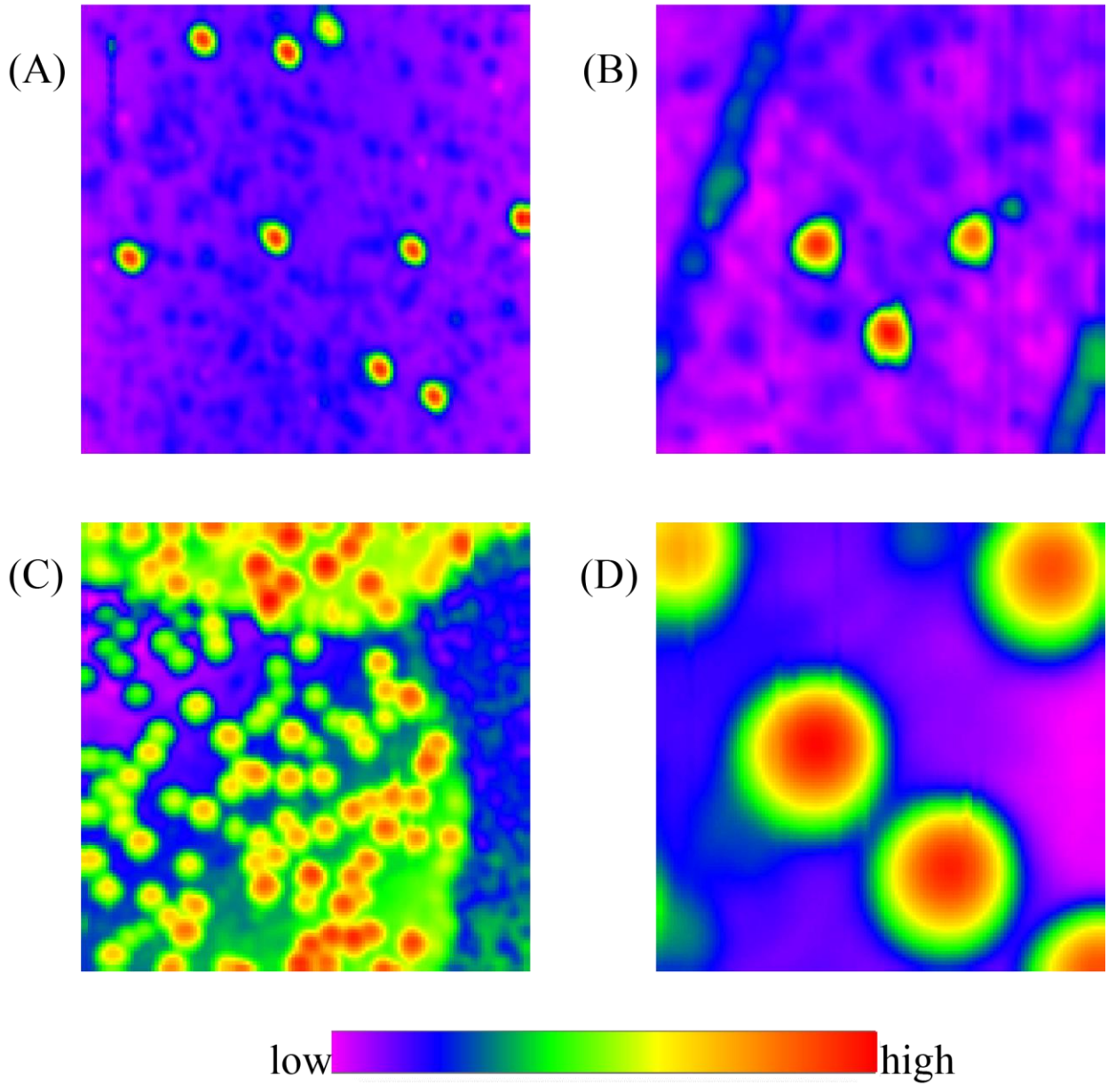
(A)
(B)
(C)
(D)
low
high

`

Fig 6.4: Spectroscopy of Fe cluster on NiAl (110) at 84K, (A) 60Å×60Å STM topography image taken at V_B=2.50V, I_T=0.10nA of a 2~3nm Fe cluster on NiAl, (B) dI/dV of the NiAl BKGD and the Fe nanocluster, the red curve shows the dI/dV with 220nm fs laser in junction, the negative bias side is dominated by photoemission, (C) dI_{DC}/dV on the nanocluster and NiAl at tunneling and out of tunneling, the photoemission at negative bias dominates the signal, with double peaks around 0V, the peak position slightly varies, (D) dI_{RF}/dV with the double lock-in technique. The tunneling set point for all the spectrum is at (2.5V, 0.1nA).

`

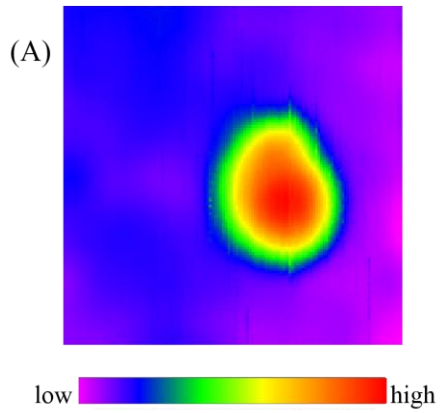
(A)
low
high

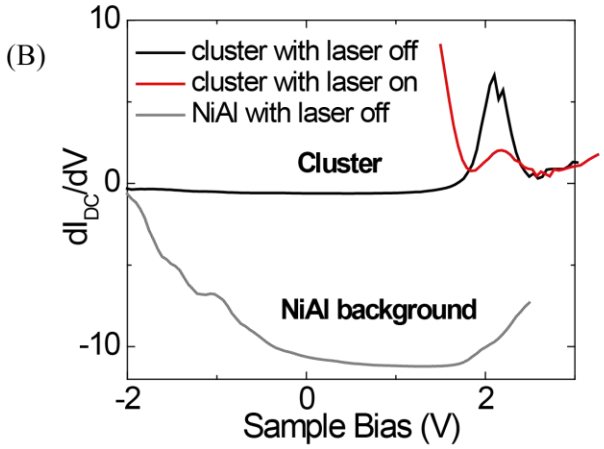
(B)
cluster with laser off
cluster with laser on
NiAl with laser off
Cluster
NiAl background
dI_DC/dV
Sample Bias (V)

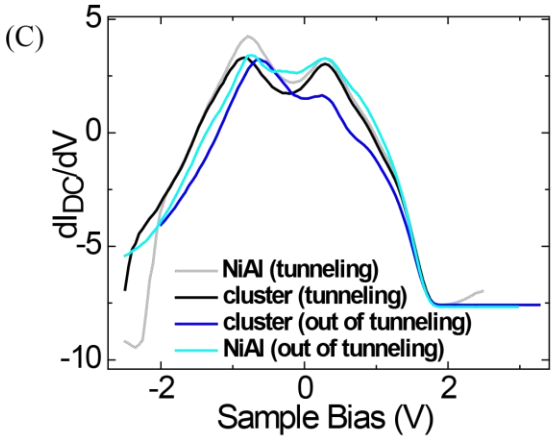
(C)
NiAl (tunneling)
cluster (tunneling)
cluster (out of tunneling)
NiAl (out of tunneling)
dI_DC/dV
Sample Bias (V)

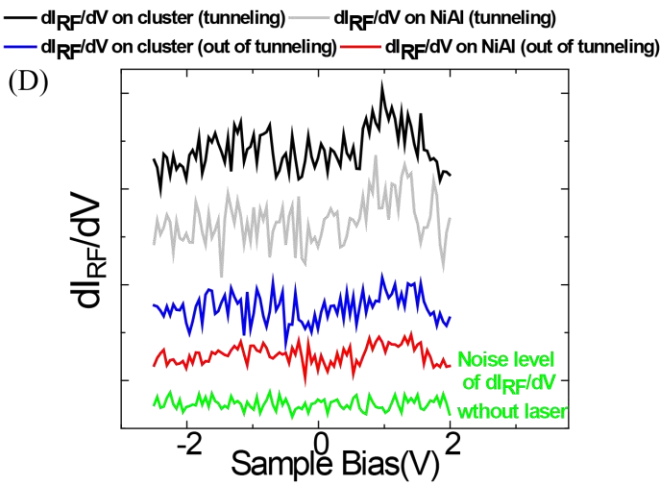
dI_RF/dV on cluster (tunneling)
dI_RF/dV on NiAl (tunneling)
dI_RF/dV on cluster (out of tunneling)
dI_RF/dV on NiAl (out of tunneling)
(D)
Noise level of dI_RF/dV wthout laser
dI_RF/dV
Sample Bias(V)

`

Fig 6.5: Spectroscopy of Fe cluster on Al_2O_3 at 84K, (A) 125Å×125Å STM topography image taken at V_B=3.00V, I_T=0.10nA of a 3~4nm Fe cluster on Al_2O_3/NiAl, (B) dI/dV of the Al_2O_3 BKGD and the Fe nanocluster, the red curve shows the dI/dV with 220nm fs laser in junction, the negative bias side is dominated by photoemission, (C) dI_{DC}/dV on the nanocluster with and without the 220nm in junction, showing the peak shifts from 2.2V to 2.3V with laser, (D) dI_{RF}/dV with the double lock-in technique, the whole dI_{DC}/dV on the nanocluster with laser is also shown for comparison. The tunneling set point for all the spectrum is at (3V, 0.1nA).

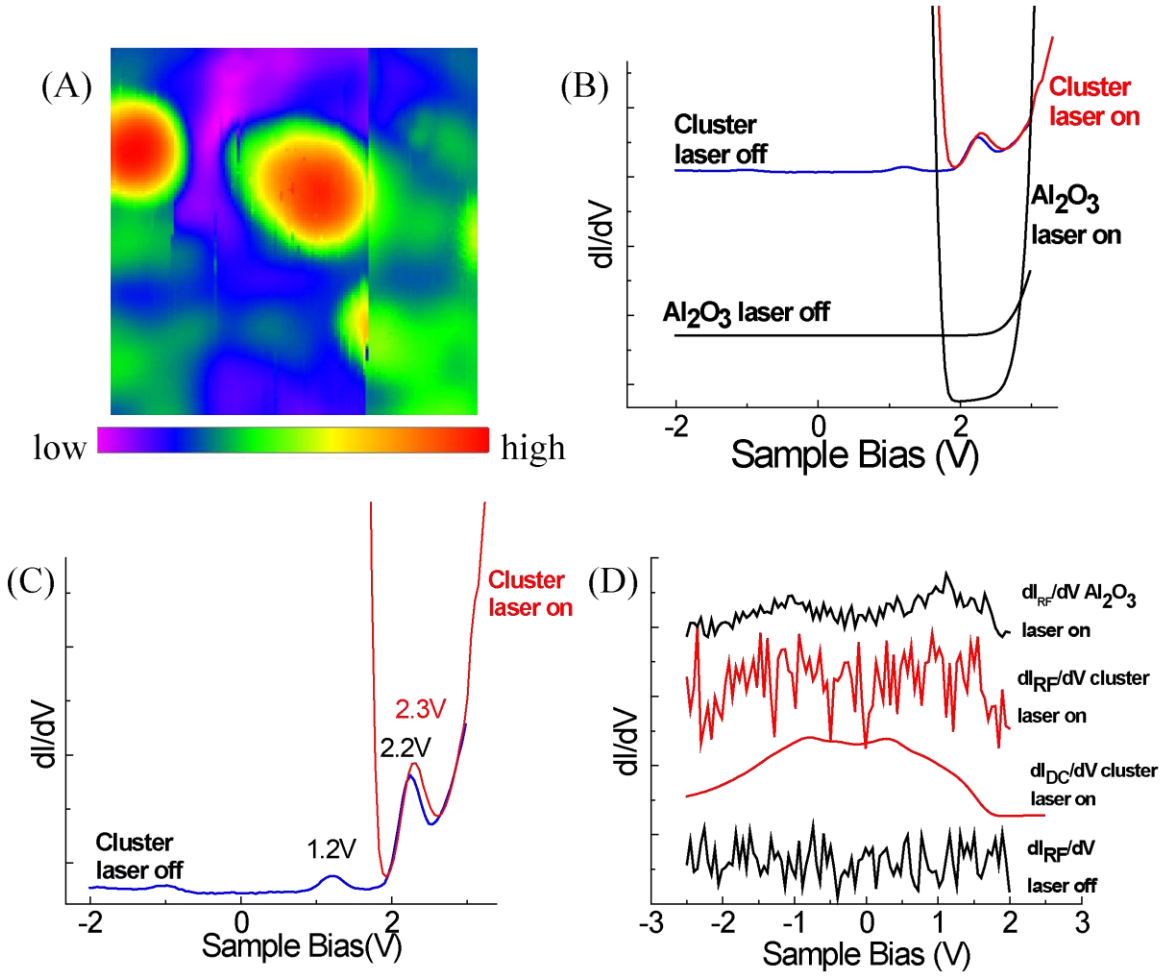
(A)
low
high
(B)
Cluster
laser off
Cluster
laser on
Al2O3
laser on
Al2O3 laser off
dI/dV
-2
0
2
Sample Bias (V)
(C)
Cluster
laser on
2.3V
2.2V
1.2V
Cluster
laser off
dI/dV
-2
0
2
Sample Bias(V)
(D)
dIRF/dV Al2O3
laser on
dIRF/dV cluster
laser on
dIDC/dV cluster
laser on
dIRF/dV
laser off
dI/dV
-3
-2
-1
0
1
2
3
Sample Bias (V)

`

Fig 6.6: Fe nanoclusters and islands after annealing to 600℃,(A) 2000Å×2000Å STM topography image taken at V_B=3.01V, I_T=0.10nA, (B) 1000Å×1000Å STM topography image taken at V_B=3.01V, I_T=0.10nA, (C) 500Å×500Å STM topography image taken at V_B=3.01V, I_T=0.10nA, (D) 250Å×250Å STM topography image taken at V_B=3.01V, I_T=0.10nA.

`

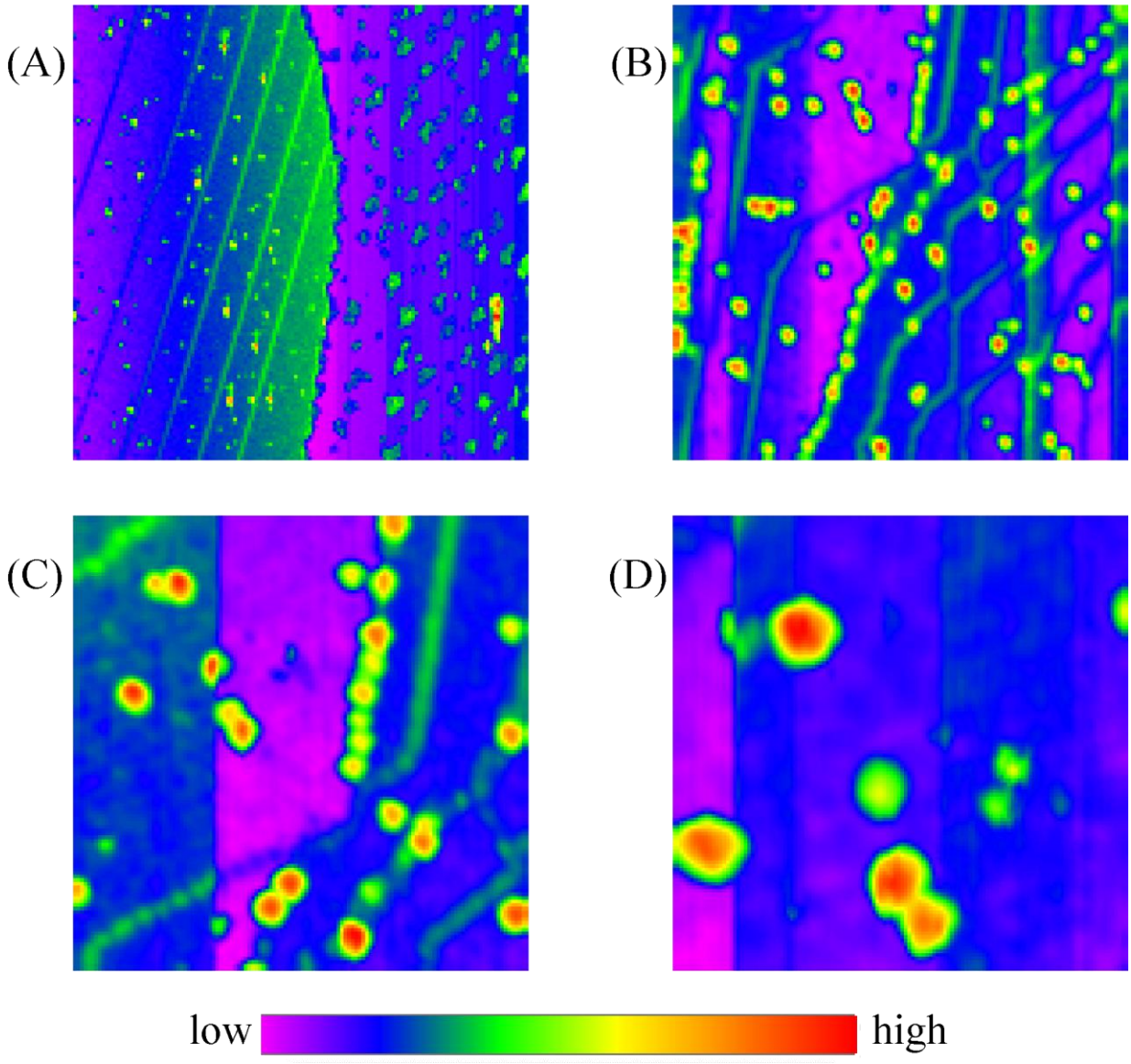
(A)
(B)
(C)
(D)
low
high

`

Fig 6.7: Spectroscopy of the annealed clusters at 21K, (A) 140Å×140Å STM topography image taken at V_B=3.00V, I_T=0.10nA of two Fe cluster on Al_2O_3, (B) dI/dV of the Al_2O_3 BKGD and the two Fe nanoclusters in (A), the tunneling set point is at V_B=3.00V, I_T=0.10nA, (C) 70Å×70Å STM topography image taken at V_B=2.50V, I_T=0.12nA of Fe cluster dimer on Al_2O_3, (D) dI/dV of different points on the dimer in (C), the tunneling set point is at V_B=2.50V, I_T=0.12nA.

`

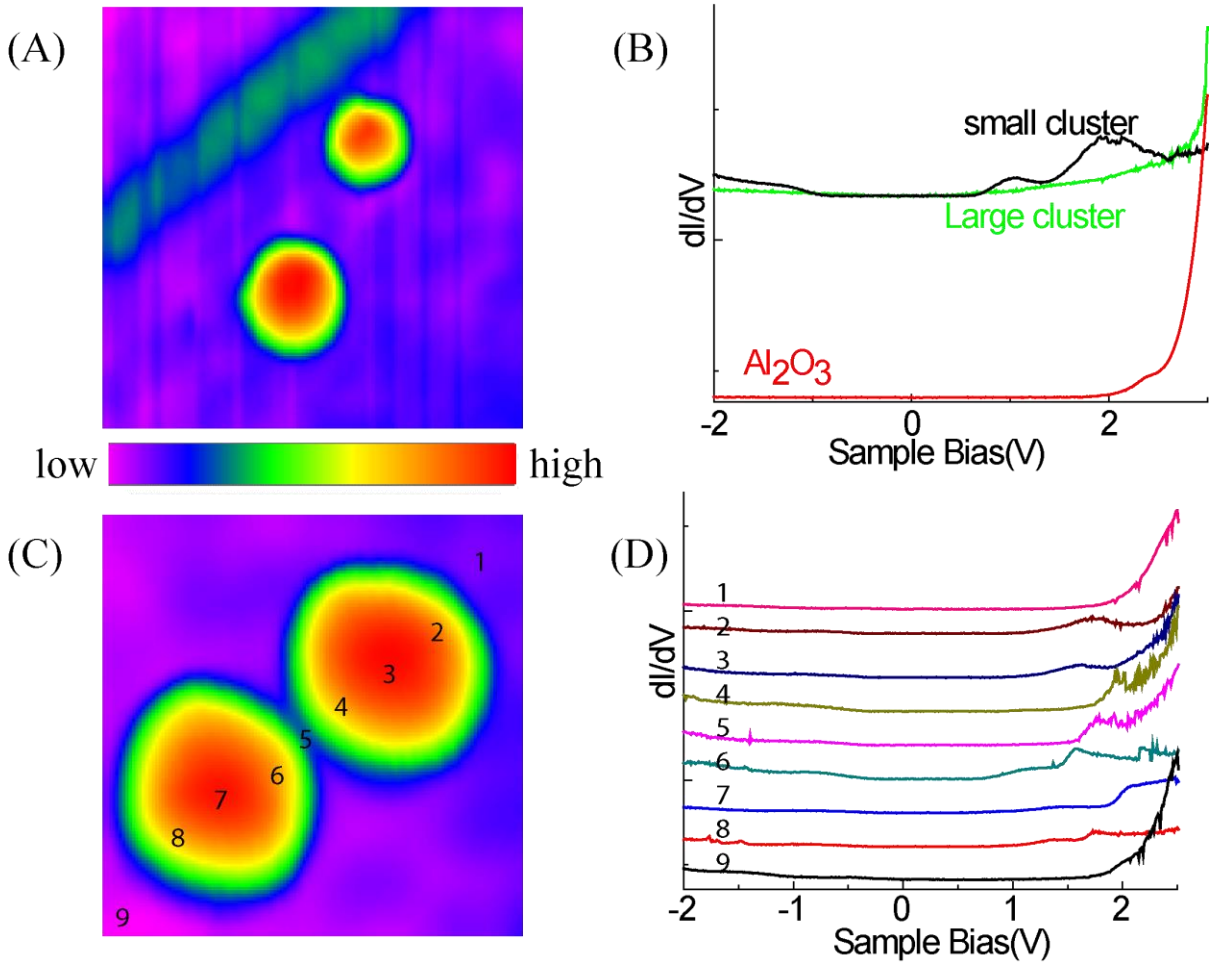
(A)
low
high
(B)
small cluster
Large cluster
Al_2O_3
dI/dV
-2
0
2
Sample Bias(V)
(C)
1
2
3
4
5
6
7
8
9
(D)
dI/dV
-2
-1
0
1
2
Sample Bias(V)

`

Bibliography

1. "Oxide Ultra-thin Films on Metals: New Materials for the Design of Supported Metal Catalysts", H-J. Freund and G. Pacchioni, *Chem. Soc. Rev.* **37**, 2224-2242 (2008).
2. "Nitrogen Fixation at Passivated Fe Nanoclusters Supported by an Oxide Surface: Identification of Viable Reaction Routes Using Density Functional Calculations", Ž. Šljivančanin, H. Brune and A. Pasquarello, *Phys. Rev. B.* **80**, 075407 (2009).
3. "Spintronics: A Spin-Based Electronics Vision for the Future." S. A. Wolf *et al*, *Science* **294**, 1488-1495 (2001).
4. "Plasmon-Induced Hot-Electron Generation at Nanoparticle/Metal-Oxide Interfaces for Photovoltaic and Photocatalytic Devices", C. Clavero, *Nat. Photon.* **8**, 95-103 (2014).
5. "Single-molecule Chemistry", W. Ho, *J. Chem. Phys.* **117**, 11033-11061 (2003).
6. "Structure and Electronic Properties and Fe Nanostructures on MgO(001), P. Luches *et al*, *Surface Science.* **601**, 3902-3906 (2007).
7. "Nucleation of Ordered Fe Islands on Al_2O_3/Ni_3Al (111)", A. Lehnert *et al*, *Surface Science.* **600**, 1804-1808 (2006).
8. "Highly Ordered Pd, Fe and Co clusters on Alumina on Ni_3Al (111)", A. Buchsbaum *et al*, *Phys. Rev. B.* **81**, 115420 (2010).
9. "Supported Fe Nanoclusters: Evolution of Magnetic Properties with Cluster Size", Ž. Šljivančanin and A. Pasquarello, *Phys. Rev. Lett.* **90**, 247202 (2003).
10. "Electronic Properties of Fe clusters on a Au (111) Surface", A. Delga *et al*, *Phys. Rev. B.* **84**, 035416 (2011).
11. "Influence of a Heterogeneous Al_2O_3 Surface on the Electronic Properties of Single Pd Atoms", N. Nilius, T. M. Wallis, and W. Ho, *Phys. Rev. Lett.* **90**, 046808 (2003).

`

12. “Vibrationally Resolved Fluorescence Excited with Submolecular Precision”, X. H. Qiu, G. V. Nazin, W. Ho, *Science* 299, 542-546(2003).

13. “A Variable-temperature Scanning Tunneling Microscope Capable of Single-molecule Vibrational Spectroscopy”, B. C. Stipe, M. A. Rezaei, W. Ho, *Rev. Sci. Instrum*. **70**, 137−143 (1999).

`

Chapter 7

Concluding Remarks and Future Prospects

7.1 Concluding Remarks

Two important molecules are extensively studied in this dissertation with STM at sub Å resolution by probing with H_2 or a CO terminated tip. The molecular orbital of 4, 7-Di ([2, 20-bithiophen]-5-yl) benzo[c] [1, 2, 5] thiadiazole (4T-BTD) with intramolecular donor-acceptor-donor sites is probed with the electronic state dI/dV imaging and H_2 rotational and vibrational spectromicroscopy. H_2 rotational spectromicroscopy on the 4T-BTD molecule shows the sub Å detailed LUMO structure of the molecule. Understanding the properties of the conjugated building blocks like 4T-BTD will help building blocks to extended semiconducting molecules with predictable properties. 1, 4-Phenylene Diisocyanide (PDI) is probed by imaging with a CO-terminated tip and H_2. At low H_2 coverage the STM H_2 vibrational spectromicroscopy clearly shows the two N sites; at high H_2 coverage, the topography image already shows three parts of the molecule with interactions with the surface, the H_2 vibrational spectromicroscopy shows more details of the molecule and its interaction with the substrate. Topography image with a CO-tip also shows different parts of the molecule and the interaction with the substrate. PDI can self-assemble on noble metal surfaces to form nanostructures, which could have potential applications in molecular electronics and catalysis.

Further combination of a RF-STM with a tunable femtosecond laser enables the investigation of light-molecule interactions. In this dissertation, efforts are spent to setup a new tunable fs laser (220 nm~1040 nm) to couple with the RF-STM. The wavelength of a MaiTai

`

Deepsee (690~1040) is extended by a harmonic generator to generate the 2^{nd}, 3^{rd} and 4^{th} harmonics. The 2^{nd}, 3^{rd} and 4^{th} harmonic can be applied for photon induced chemistry or photoemission, the 2^{nd} harmonic or 3^{rd} harmonic can also be used to perform pump-probe time resolved study by overlapping with the fundamental. The fundamental and fundamental (1+1), fundamental and 2^{nd} harmonic (1+2), fundamental and 3^{rd} harmonic (1+3) are aligned to overlap on the diagnostic path on the optical table. Only fundamental and fundamental can be routinely aligned to overlap in the STM junction, the UHV in-situ lens change the spatial and temporal overlap of different color beams.

The effects of the femtosecond laser are followed by detecting photo induced electron emission and photochemistry. 4^{th} harmonic UV laser beam induced DC and RF photocurrent has been detected out of tunneling, multiphoton current induced by two overlapped fundamental beams is also detected. The signal is too noisy to be detected at tunneling; a new double lock-in technique is applied to detect the weak laser-induced signal in the tunneling regime. To sharpen the energy width and increase the lifetime of the excited states of molecules, thin aluminum oxide and copper oxide are grown on metal surfaces to provide electronic isolation of the metal substrate and adsorbed molecules. Different molecules are studied on the oxide. Metal nanoclusters are grown on metal and oxide to improve laser-induced signal through plasmonic enhancements.

7.2 Future Prospects

7.2.1 Fabricated Tip

To detect the laser induced signal in the tunneling regime, the current STM4 configuration with the in situ UHV cryogenic RF amplifier is not sensitive enough. It has been shown by using the

`

fabricated grating on a Au tip, much greater plasmonic enhancement are achieved to get the photoinduced current in the nA range [1]. For more plasmonic enhancements, a fabricated Ag, Au or Cu tip can be used in the laser-STM experiments. Combining the fabricated tip, cryogenic RF amplifier and the double-lock in technique, there is a good chance to detect the photoindcued current in the tunneling regime and successfully perform the long time pursued spatially resolved lifetime measurement with a laser STM. To get the two different color laser beams aligned in the STM junction for time resolved experiments, one way is to use parabolic mirror outside of the UHV chamber for better simulation on the optical table, although the beam size in the junction will become bigger given the longer focal length [2]. An electron analyzer could also enhance the sensitivity to detect photoinduced electrons [2].

7.2.2 Designed Molecules

Preliminary data in this dissertation shows the possible photoisomerization and phtodissociation of the azulene molecules with big laser power shining into the junction out of tunneling. Coworkers in the Ho Group already got sub-Å structural and molecular orbital images with H_2 and CO terminated tip [3]. With the new grating tips, plasmonic enhancement would induce photoisomerization and dissociation, one molecule at a time. With the H_2 and CO terminated tip imaging, one should be able to image the sub-Å structure of the naphthalene after isomerization and the smaller molecules after dissociation. The molecular orbital of 4T-BTD molecule is extensively investigated in this dissertation; the life time of the excited state of this molecule could be further investigated with the laser STM. Alizarin molecules may stand up on metal and oxide surfaces, which could be used for the proposed fs-stimulated Raman experiments [4]. CO_2 and CO_2^- adsorbed on Au-PDI chains could be further investigated by STM-IETS.

`

7.2.3 Oxide Surfaces

Aluminum oxide on NiAl(110) and copper oxide on Cu(110) are investigated in this dissertation. Aluminum oxide has a large band gap, could be used as an insulator to study single molecules. Although copper oxide on Cu(110) is not a good electric insulator, it has been proved to be a magnetic insulator [5], the magnetic properties of small molecules like NO and large magnetic organic molecules can be probed on this well-defined oxide, a Cu tip instead of Ag tip might be more stable on the CuO surface. Other insulating surfaces can also be investigated, especially the ones with various thicknesses of insulating layers, like MgO on Ag(100) [6]. Such thicker insulating layers will further increase the life time of the excited states of adsorbed molecules.

7.2.4 Ag and Au Nanoclusters

Fe nanoclusters are grown on oxide and metal surfaces and studied with the laser STM in this dissertation, besides DC dI/dV spectroscopy, RF dI/dV spectroscopy is also recorded with the double lock-in technique. The catalytic properties of Fe nanoculsters can be further investigated. With the new amplifier and grating tips, RF signal may be detectable in the tunneling regime. Ag and Au nanoclusters which have better plasmonic properties can now be also grown on the surface as the Au and Ag evaporators are ready. The plasmonic enhancement of these nanoclusters can help detect the photoinduced signal in the tunneling regime. Moreover, the plasmons induced by the laser and greatly enhanced by the grating tip and nanoclusters could be used in photocatalysis [7].

`

Bibliography

1. "Hot-Electron Nanoscopy Using Adiabatic Compression of Surface Plasmons", A. Giugni, B. Torre, A. Toma *et al*, *Nat. Nano* **8**, 845-852(2013).
2. "Femtosecond Time-Resolved Two-Photon Photoemission Studies of Electron Dynamics in Metals", H. Petek and S. Ogawa, *Prog. Surf. Sci.* **56**, 239-310(1997), and private communication with H. Petek.
3. S. Li, A. Ye and W. Ho, to be published.
4. Original data from Peter Lu's Group at Bowling Green State University, OH; priviate communication with H. Kumar Wickramasinghe.
5. "Adsorption-Induced Switching of Magnetic Anisotropy in a Single Iron (II) Phthalocyanine Molecule on an Oxidized Cu (110) Surface", N. Tsukahara, M. Kawai et al, *Phys. Rev. Lett.* **102**, 167203 (2009).
6. "Oxide Ultra-thin Films on Metals: New Materials for the Design of Supported Metal Catalysts", H-J. Freund and G. Pacchioni, *Chem. Soc. Rev.* **37**, 2224-2242 (2008).
7. "Plasmon-Induced Hot Carrier Science and Technology", M.L. Brongersma, N.J. Halas and P. Nordlander, *Nat. Nano* **10**, 25-34(2015).

`

Appendix A

STM4 Optics Setup

A.1 Catalog

Below is the catalog of the optical devices in STM4, the optical path and setup photo is shown as in fig2.1 and fig2.2 of chapter 2.

Table A.1 Optics Catalog for STM4

Catalog of Optical Devices for STM 4				
Symbol	Device Purpose	Company	Product # & Characteristics	Price
Ti: Sapphire Laser	MaiTai Deepsee	Spectra Physics	Mai Tai EHP DS + Warrenty supplement +Gold Level Service Tunable from 690-1040, 70fs-100fs pulse width, 80MHz, 2.5W at 800nm	160,000
Periscope 1	Change the beam from p to s, change the height of the beam from 4.38" to 5.5 "	Newport	9151-M 12" Periscope kit and m1, m2	434.88
m1	Mirror for fundamental	Newport	10Q20UF.35S 45 degrees AOI, reflect over 99.6% from 680 to 1060 nm, optimized for s	499
m2	Mirror for fundamental	Newport	10Q20UF.35P 45 degrees AOI, reflect over 99.6% from 680 to 1060 nm, optimized for p	499
m3	Mirror for fundamental	Newport	10Q20UF.35S	499
m4	Mirror for fundamental	Newport	10Q20UF.35S	499
lens1	Combine with lens 2 as a telescope to reduce beam size f=75mm	CVI	PLCX-25.4-38.6-UV	140
lens2	f=65mm	CVI	PLCX-25.4-33.7-UV	300
TS 1	Adjust the distances between lenses	Newport?	From Stock	

`

LPC	Stabilize laser power, 700-1100nm	BEOC	MI - 10450 – NIR,	5450
BS 1	20% power goes to fundamental path, 80% goes to harmonic generator	Chroma	20-80bs-NIR 20/80 beam splitter, 20R, 80T. 600-1200nm wavelength range, laser-grade substrate AR-coating Actually 30-70 beam splitter	200
m5	Mirror for fundamental	Newport	10Q20UF.35S	499
m6	Mirror for fundamental	Newport	10Q20UF.35S	499
Harmonic Generaor	2^{nd}-4^{th} harmonic	Photop	TP-2000B THG + FHG NuAssembly Automatic Tuning 2^{nd} : 345-520 3^{rd}: 230-345 4^{th}: 210-230	20,360
m7	Mirror for fundamental	Newport	10Q20UF.35S	464.07 w/discount
m8	Mirror for fundamental	Newport	10Q20UF.35S	464.07
m9	Mirror for fundamental	Newport	10Q20UF.35S	464.07
BS 2	50% power goes to delay stage, 50% goes to retroreflector	Chroma	50/50bs-NIR 600-1200nm range, 25mm diameter, laser grade substrate, AR coating	200
TS 2	Translational Stage, adjust the two beams to overlap	Newport	Can be adjusted in 3 directions, same as TS8	From Stock
m10	Mirror for fundamental	Newport	10Q20UF.35S	464.07
m11	Mirror for fundamental	Newport	10Q20UF.35S	464.07
Retroreflector	Make sure reflected beam and incoming beam parallel	Newport	UBBR1-1S	1343
Shaker	With the PZ-70 power supply, modulate the laser beam at low frequency	Homemade	Refer to shaker manual for more detail	
Delay Stage	Vary the delay time between pump and probe beams	Newport	UTS100CC	3460.53
m12	Mirror for 2^{nd} harmonic	Photop	HR340/550-45	182
lens3	Combine with lens4	CVI	PLCX-25.4-25.8-UV-355-	266

`

	as a telescope to reduce the 2nd harmonic beam size f=50mm		532	
lens4	Laser grade UV fused silica lens, with 355-532nm AR coating f=250mm	CVI	PLCX-25.4-128.8-UV-355-532	225.00
TS 3	Adjust the lens position for different wavelengths	Thorlabs	LNR25M	620
TS 4	Adjust the 2nd harmonic path distance to make it overlap with the fundamental	Thorlabs	LNR25D (for laser path direction) LNR25M(for aligning purpose)	710 620
m13	Mirror for 2nd harmonic	Photop	HR340/550-45	182
m14	Mirror for 2nd harmonic	Photop	HR340/550-45	182
Periscope 2	Change the beam height of 2nd harmonic	Newport	BSD-2A	401.75
m15	Mirror for 2nd harmonic	Photop	HR340/550-45	182
m16	Mirror for 2nd harmonic	Photop	HR340/550-45	182
m17	Mirror for 2nd harmonic	Photop	HR340/550-45	182
m18	Mirror for 2nd harmonic	Photop	HR340/550-45	182
d1	Dichroic mirror Reflect 2nd harmonic, transmit fundamental	Chroma	600dcxru lot#239437	275
m19	Mirror for fundamental	Newport	10Q20UF.35S	464.07
m20	Mirror for 3rd harmonic, interchangeable with m26 short for below 880nm	Photop	m20L: HR288/340-45 m20S: HR230/300-45	Come with the HG
m21	Mirror for 3rd harmonic, short for below 880nm	Photop	m20L: HR288/340-45 m20S: HR230/300-45	Come with the HG
m22	Mirror for 3rd harmonic	Photop	HR230/350-45	382
m23	Mirror for 3rd harmonic	Photop	HR230/350-45	382

`

lens5	Combine with lens 6 as telescope to reduce 3rd harmonic beam size f=50mm	CVI	PLCX-25.4-23.6-CFUV-248-355	530
lens6	CaF2 lenses with AR coating f=200mm	CVI	PLCX-25.4-93.2-CFUV-248-355	375
TS 5	Adjust distance between lens 5 and lens 6	Thorlabs	LNR25M	535
TS 6	Adjust the 3rd harmonic path distance to make it overlap with the fundamental	Thorlabs	LNR25D (for laser path direction) LNR25M(for aligning purpose)	620 535
m24	Mirror for 3rd harmonic	Photop	HR230/350-45	382
m25	Mirror for 3rd harmonic	Photop	HR230/350-45	382
d2	Reflect 3rd harmonic, fundamental and 2nd harmonic transmitted Transmission not good under 400nm	Photop	HR230/350-45	382
m26	4th harmonic mirror, interchangeable with m20 30 degrees AOI	Photop	HR210/235-30	Come with the HG
m27	4th harmonic mirror, 30 degrees AOI	Photop	HR210/235-30	Come with the HG
lens7	Combine with lens 6 as telescope to reduce 4th harmonic beam size f=50mm	CVI	PLCX-25.4-23.6-CFUV-193-248	550
lens8	CaF2 lenses with AR coating f=150mm	CVI	PLCX-25.4-70.6-CFUV-193-248	395
TS7	Adjust distance between lens 7 and lens 8	Newport	Al made, not fancy	From Stock
m28	4th harmonic mirror, 45 degrees AOI	Photop	HR210/235-45	290
m29	Mirror for fundamental	Newport	10Q20UF.35S	464.07
m30	Mount with a flip mount, reflect the beam for diagnosis	CVI	DUVA-PM-1025-UV	220.8

`

m31	Reflect all wavelengths	CVI	DUVA-PM-1025-UV	220.8
lens9	Focus the beam to the crystal f=3”	CVI	PLCX-25.4-38.66-UV	140
BBO Crystal 1	For 1+1 autocorrelation 8×5×0.5mm	Photop	BBO, SHG-AC-A	760
BBO Crystal 2	For 1+2 and 3-1 autocorrelation 10x10x0.4mm	Photop	BBO- AC-3-1	1570
TS8	Adjust the BBO crystal in 3 directions to maximize the autocorrelation signal	Newport	Good one, same as TS2	From Stock
Filter 1	Block fundamental up to OD 6, transmit 2nd harmonic Used in 1+1 and 3-1 autocorrelation	Chroma	ET650SP-2p (spare)ET650sp-3P	575 800
Filter 2	Block fundamental and 2nd harmonic, transmit 3rd harmonic, need to combine with dichroic mirror	Schott	3mm UG11 glass filter	114
lens10	Focus the beam to the photodiode f=1.5”	CVI	PLCX-25.4-19.6-UV	290
TS9	Adjust the distance between lens9 and lens10			
Photodiode	Measure the laser signal	Thorlabs	DET10A	139.4

In August, 2013, we found the 2nd harmonic beam was not optimized; the beam is too broad when it meets lens 3 and lens 4. So we revised the 2nd harmonic path, lenses 3 and 4 are now in the later position, the 2nd harmonic beam now travels at 3 inches height for long distance. A few mirrors are added as below.

m32	Mirror for 2nd harmonic	Photop	HR340/550-45	182
m33	Mirror for 2nd harmonic	Photop	HR340/550-45	182
Periscope 3	Change the 2nd harmonic beam from	Newport	BSD-2A	401.75

`

	p-polarized to s-polarized, and change the beam height back			
m34	Mirror for 2nd harmonic	Photop	HR340/550-45	182
m35	Mirror for 2nd harmonic	Photop	HR340/550-45	182

A.2 MaiTai-DeepSee

To connect the MaiTai or DeepSee controller to our PC, we can use either RS232 cable or USB-RS232 adaptor. In case of using the latter, we have to use the National Instrument RS-232 USB adaptor, otherwise there is software crashed frequently somehow.

The laser beam coming out of the MaiTai has a horizontal polarization. We used the periscope with s- and p-polarized dielectric mirrors for femtosecond pulse laser to change the polarization to vertical since LPC and the harmonic generator require the vertical polarization for input beam. The repetition rate actually depends on the wavelength.

Table A.2 Mai Tai Frequency Dependence of Wavelength

λ (nm)	f(MHz)
700	79.59
800	79.55
900	79.90
940	80.03
950	80.07
1000	80.25

There is a huge RF interference peak at 80MHz picked up by our RF detection circuit, so the wavelength near 940nm might not be used.

DeepSee unit is attached to the end of MaiTai output inside the laser box and can provide the

`

computer-controlled group velocity dispersion (GVD) compensation in order to achieve the shortest pulses possible at the sample. This compensation is done by moving the motor that moves optical materials on a stage. DeepSee GUI screen shows the range of the motor which are determined by upper and lower "soft limits". The smaller percent values correspond to a lower absolute value of GVD. We found the shortest pulse width at each wavelength was achieved when the motor is at the lower limit by examining interference signal from the autocorrelation stage. Since the pulse width is minimized, the output power from the harmonic generator described in detail below is also maximized, more than twice with the DeepSee as that without it.

A.3 LPC

After turning on the power of LPC controller, LPC shows the minimum power and transmission state, which means that the polarization of the incoming beam is vertical according to BEOC. The glass mounted on the circuit board is the LC cell and the cubic crystal behind that is output polarizer, there is NO input polarizer in our LPC (figA.1).

The laser power will fluctuate if the input beam size is bigger than the input aperture which is 4mm. Power threshold of LPC is 4W/4mm, while MaiTai has the max power of 2.75W (2.6W with DeepSee) @ 800nm. We reduced the beam size from 4mm to 3.5mm by using the pair of Fused Silica lens with f=65mm and 75mm, and now the power threshold for 3.5mm is 3W.

A.4 **Harmonic generator** (TP 2000B Tripler, Photop Technologies)

2^{nd}, 3^{rd} and 4^{th} harmonic beams are generated here. The 1^{st} waveplate depicted on the manual has been removed from our setup since our input beams has a vertical polarization. Read the manual carefully (figA.2). Sheng gave us a set of crystals and here is the table. The crystals with boldfaced name are being used now.

`

Table A.3 Nonlinear Crystals for Harmonic Generator and Diagnosis

	Material (BBO or LBO)	Thickness	Wavelength
60fs 2nd harmonic	5x5x1.1mm LBO	1.1mm	680-1,100nm
100fs 2nd harmonic	**5x5x2mm LBO**	2mm	680-1,100nm
60fs 3rd harmonic	7x7x0.6mm BBO	0.6mm	680-1,100nm
100fs 3rd harmonic	**7x7x1mm BBO**	1mm	680-1,100nm
60fs 4th harmonic	**7x7x0.6mm BBO**	0.6mm	680-1,100nm
100fs 4th harmonic	7x7x1mm BBO	1mm	680-1,100nm
2nd auto crystal	8x5x0.5mm BBO	0.5mm	600-1,100nm
3-1 or 1+2 auto crystal	10x10x0.4mm	0.4mm	720-900nm

Here is some note we'd better keep in mind when optimizing THG and FHG in the harmonic generator (You can refer the layout of the optics inside HG and the generated laser path in the above photos).

1. Make sure the incoming fundamental beam go through near the center of the SHG crystal since the beam will slightly diverts as λ is changed.

`

2. Find “absolute zero” before calibration so that actuators can rotate the crystals with max range. First, using axis positioner window of TPI, send large negative value to each axis until – limit is lit on. Then turn off the motor and manually turn the actuator toward the positive direction until “-limit” was off. Finally press zero to reset. Now the positioner is at zero position.

3. Make sure SHG spot can be optimized within the range of the angle of the SHG crystal for all wavelengths.

4. Make sure arrows of time plate (TP) and SHG crystal are always antiparallel otherwise building up. Currently the crystal orientation of TP is Arrow Downward, while that of SHG crystal is Arrow upward.

5. For THG, we need to use THG crystal as well as the time plate (TP) with M3 and M4 mirrors labeled “S(hort)” for $\lambda < 900$nm. M3 and M4 mirrors must be replaced by those labeled “L(ong)” for $\lambda \geqq 900$nm.

6. For FHG, take out TP and swap the crystal from THG to FHG. There are thick green line on the crystal holder and scribed mark on the post holder so that we can align them. We must use M3 and M4 mirrors for FHG, but keep in mind that incident of angle of FHG mirror is 30°.

7. To optimized THG(FHG) signal, need to adjust F1, F2 and both angles of WP2 (θ,φ)

Another problem we found was that the beam size of higher harmonics got broader with length. We tried reducing the beam size with a pair of plano-convex lens in the telescope configuration

`

($d_2/d_1=f_2/f_1$). The resulting beam size, however, was not reduced and collimated at all. Instead, we could happen to reduce the size by swapping the lens so that lens with the shorter focal length is placed in front of lens with the longer focal length. It's also recommended that plano-convex UV grade CaF_2 lens with BBAR coating would better for shorter wavelength such as THG and FHG. The combinations of lenses we chose are

THG: CaF_2 lens, f_1=50mm, f_2=200mm, BBAR 248 to 355nm coating for the UV region

FHG: CaF_2 lens, f_1=50mm, f_2=150mm, BBAR 193-248nm coating for the UV region

According to Sheng, we need a faster lens to focus the beam first since the FHG (THG) beam is diverging a lot before lens.

With these pair of lens, the THG beam is reduced to 1.5mm x 1mm at far field (115" away from the lens with f_2) where 1.5mm is measured along the direction vertical to the table. The FHG beam size is ~2mm x 2mm. SHG beam coming out of the harmonic generator has the horizontal polarization. We change the polarization by using two periscopes. The beam size of SHG is again reduced with the telescope configuration of a pair of lenses:

SHG: Fused Silica lens, f_1=50mm, f_2=200mm, BBAR 355-532nm coating for the UV region

A.5 Autocorrelation stage

Our autocorrelation (AC) stage is the Michaelson interference setup consisting of two arms, one fixed and another movable by the linear translation stage (ESP 301-2G Newport) controlled by Labview program through GPIB cable. We use the delay stage UTS100CC from Newport (with a mounting plate UTS-TP from the same company) in the fundamental beam to get the delay τ between the 2 beams. The temporal resolution of the stepping motor is 1 en (0.1 micron), so the temporal resolution is 0.667fs/en. The fundamental beam is guided to a Michelson Setup as in the Figure A.3. One arm has the delay stage, retroreflector and shaker. The other arm has a mirror

`

pair mounted on a plate, which is connected to a 3-direction translation stage. Initially we also want to use the mirror pair on the delay stage arm since the mirrors are specially made for MaiTai laser and have higher reflectivity. But it turns out with the machine shop made mirror-mount; it's very hard to keep the beam constant horizontally when the stage moves. It's much easier to make the two fundamental beams overlap after we use the retroreflector UBBR1-1S from Newport.

Different from the previous fs laser setup in STM2 (which has the delay stage and shaker in different arms), we have the delay stage and shaker in the same arm. The main reason is that we want to do pump-probe experiments with 2 different color beams (fundamental and 2nd harmonic, fundamental and 3rd harmonic), to make things easier, the delay stage and shaker are in the same arm. However, it's still valuable to have 2 fundamental beams overlap; we can characterize the beam with autocorrelation.

The shaker to modulate the delay is home built, since PZ-80 from Burleigh has been obsolete for long time, we used a piezo tube (EBL# 2 Piezoceramic Tube 1.00" OD x 0.060" Wall x 2.00" Length, gold over nickel electrodes) mounted in a homemade pieces designed, a detailed drawing is shown in Fig A.4~FigA.6. The housing is made of aluminum, electrically isolated from the piezo with two macor pieces; all these pieces are designed and machined as light as possible and glued together by Varian torr seal. The retroreflector is connected to the front macor piece through a homemade connector. The controller of the piezo is a Burleigh PZ-70 (we got a manual from company). We use Viking Thorkom connector from Source Research Inc. to apply the high voltage from PZ-70 to the piezo. Parts list is as follows:

`

Table A.4 Homemade shaker commercial electric parts

Socket Contact	TS-100-AU
Plug	TNP07-101
Dummy Filler	TD-200
Bulkhead Receptacle	TBR07-101-P
Backshell .150-185 Cable Dia	TSR07-201
Pin Contact	TP-100-AU

There are 7 pins in the TKR-07 receptacle, among them 3 are HV and 4 are ground. Modulation output from EG&G 7265 lock-in amplifier was fed into PZ-70 as an input sine wave. It's necessary to tune the DC bias voltage to a few hundred volts such that the amplified sine wave signal is always positive, otherwise PZ-70 will shut down. The modulation frequency is 220 Hz. For example, the amplitude from the lock-in is 1.05V (rms) and turn the Gain knob to increase the voltage until the output/100 BNC connected with the oscilloscope shows 5 V (p-to-p), which corresponds to ~500V applied to the piezo shaker. 4V p-p voltage on the monitor output (about 400V on the HV output) gave us the clearest $dS/d\tau$. Other parameters of the lock-in for $dS/d\tau$ and $d^2S/d\tau^2$ are TC 100ms, sensitivity 50mV for 1st harmonics and 1mV for 2nd harmonics

We did the piezo shaker calibration as follows. The first calibration is to obtain the relationship between the HV output and the monitor output,

It is: $HVoutput(V) = 100.61 \times MonitorOutput(V) + 0.2842$.

A second calibration is the relationship between the piezo motion with the monitor output, it's done by comparing the time zero change in the autocorrelation spectra with tuning the bias voltage.

The relationship is $piezo(microns) \times 2 = -1.13 \times MonitorOutput(V) - 0.08$.

Note that the piezo shrinks at the positive voltage applied.

A.6 Simulation Path

`

We have two BBO crystals, one for 1+1 AC (crystal orientation is vertical to the table) and another for 3-1 or 1+2 AC. For 3-1 AC, the fundamental needs to be perpendicular to THG, so we use WP1 of the harmonic generator which hasn't been used to change the polarization. The black lines on the crystal holder should be horizontal to the optical table surface. Since each of the fundamental and THG generates SHG at BBO, we need minimize these signals to distinguish 3-1 SHG signal from them. Empirically SHG spot generated from the fundamental can be minimized by adjusting the BBO crystal position and angle. We usually monitor the beams after BBO with CCD camera to check the spatial overlap and check the temporal overlap by moving the translation stage of THG. Once you see the 3-1 SHG spot, you can maximize the signal by adjusting the crystal position, angle and fine tuning the optical path. A picture below shows the BBO crystal orientation for ω=880nm for the 3-1 autocorrelation. Note the polar angle of the crystal with respect to the laser path is rotated to maximize the AC signal. For the 2+1 autocorrelation, the crystal must be rotated along the azimuthal angle with respect to the laser path.

As for the in-plane crystal orientation, the black lines marked on the rotational crystal mount, should be parallel to the SHG and the fundamental input polarizations for 2+1. In this case, it should be vertical to table, i.e., " both fundamental and the second harmonic beams are vertical to the table as well as the BBO crystal orientation". For 3-1 case, the crystal orientation must be parallel to the fundamental beam polarization, which was already rotated to the horizontal polarization by the half waveplate, i.e., parallel to the table.

To detect AC signals for 3-1 and 2+1, we need a color filter such as one used for 1+1 AC measurements. We used the same color filter as 1+1 AC for 3-1 and UG11 color filter by Schott

`

for 2+1 AC measurement. Optical density data is on the STM4 manual and also could be got through the company website.

A.7 Beams into Junction

To focus the beams into the junction, we use a lens inside the UHV chamber (focal length 3 inches); the lens is mounted on the lens holder assembly for adjusting. The assembly drawings can be found in the STM4 folder. To get a 3-D view of the junction through the pyro viewport, we need to use a finder scope. We can only see fundamental and 2^{nd} harmonic with the commercial finder scope. To see 3^{rd} and 4^{th} harmonics in the junction, we need a finder scope with fused silica lenses, which is not commercially available. We assembled a home-made finder scope with the fused silica lenses and cage assembly from Thorlabs, POs of these parts could be found in the STM4 laser system POs. The home-made finder scope works though it could be improved to a better cage system or lenses.

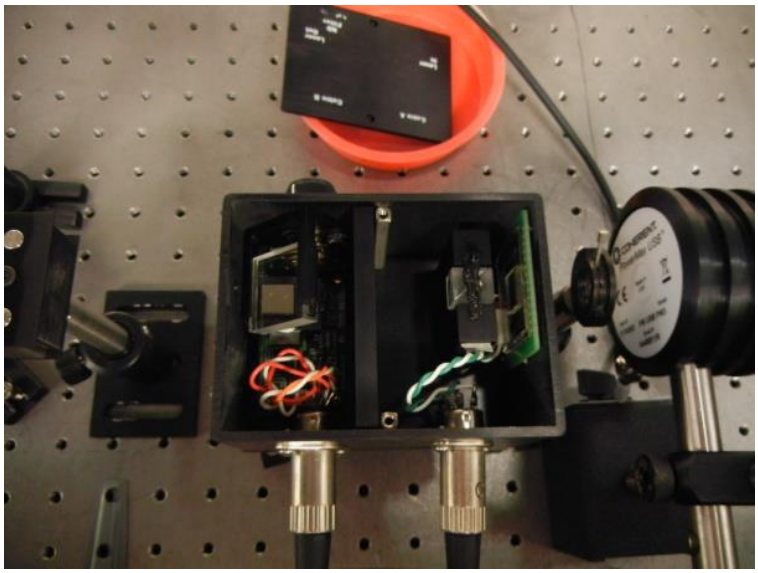

Fig A.1 Inside of LPC

`

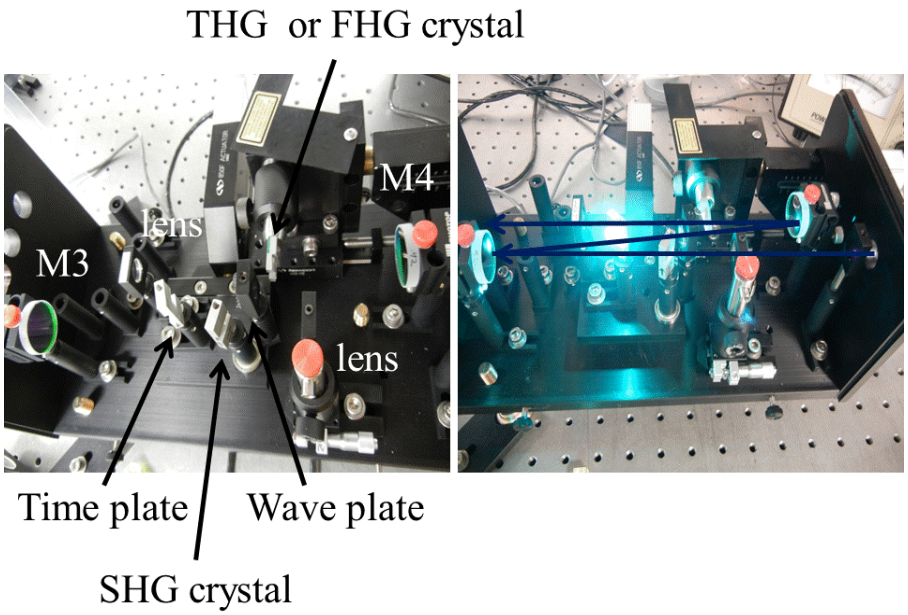

Fig A.2 Inside of the Harmonic Generator

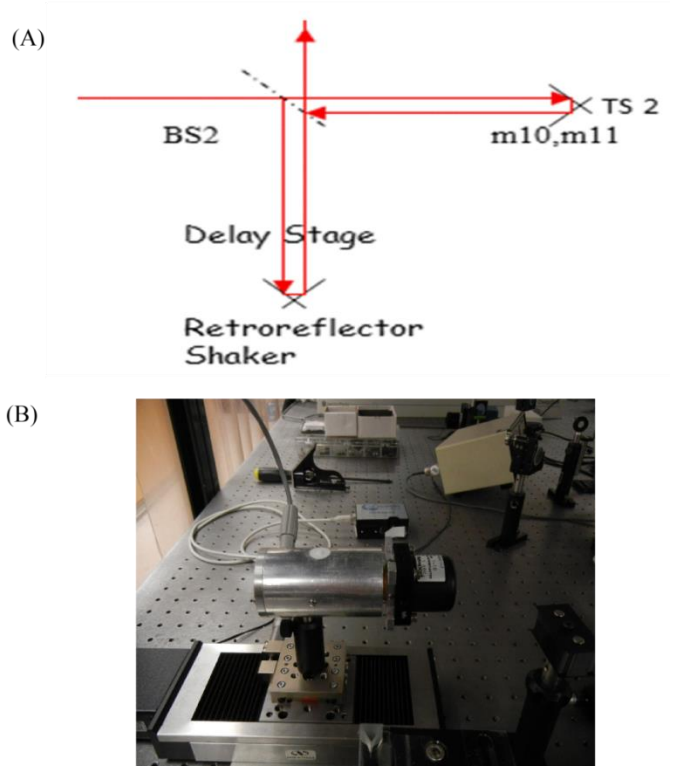

FigA.3 (A) Schematic of the Michaelson interference setup, (B) Photo of the delay stage and shaker.

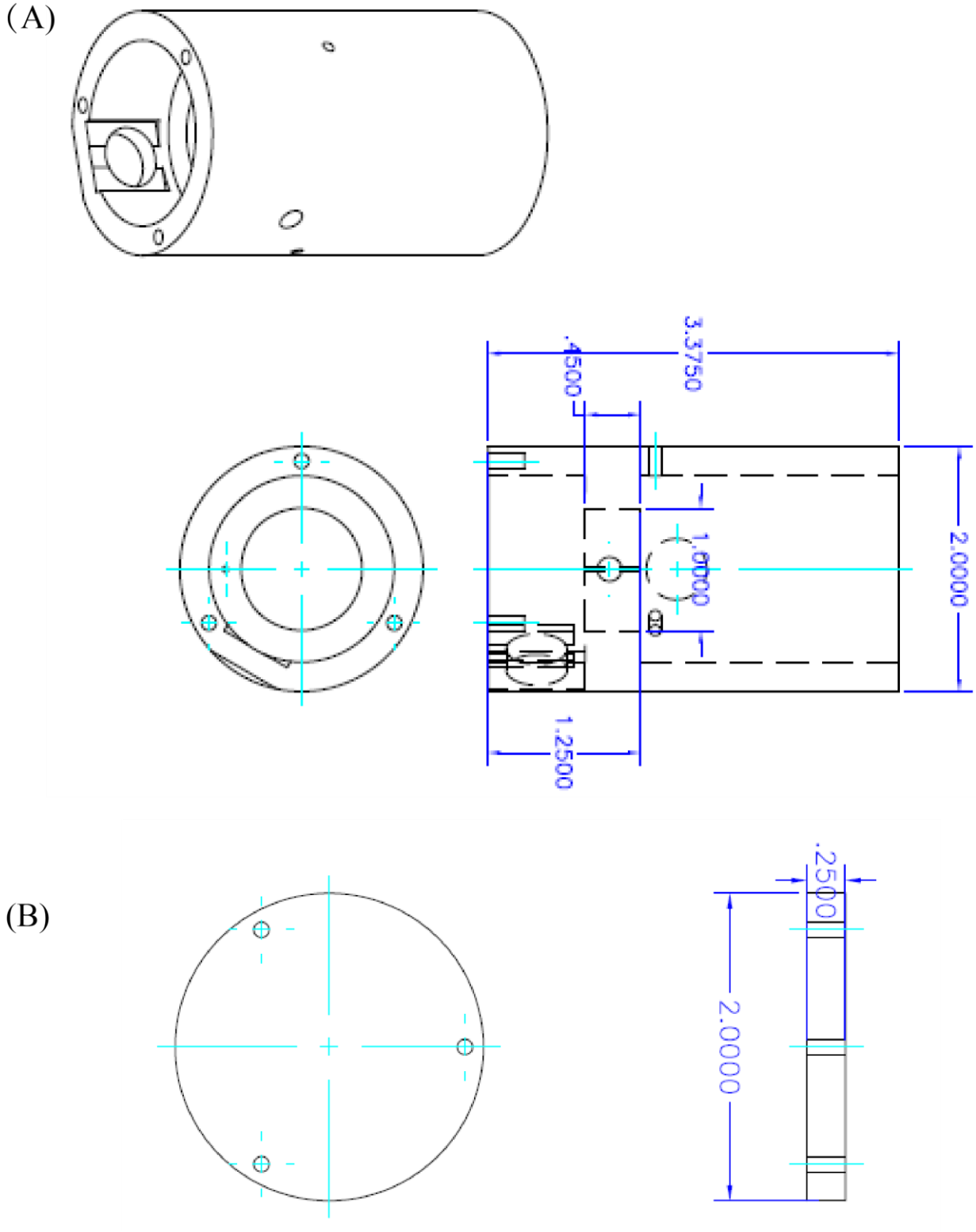

FigA.4 (A) homemade Al housing body for the shaker piezo, (B) Al cover for the housing.

`

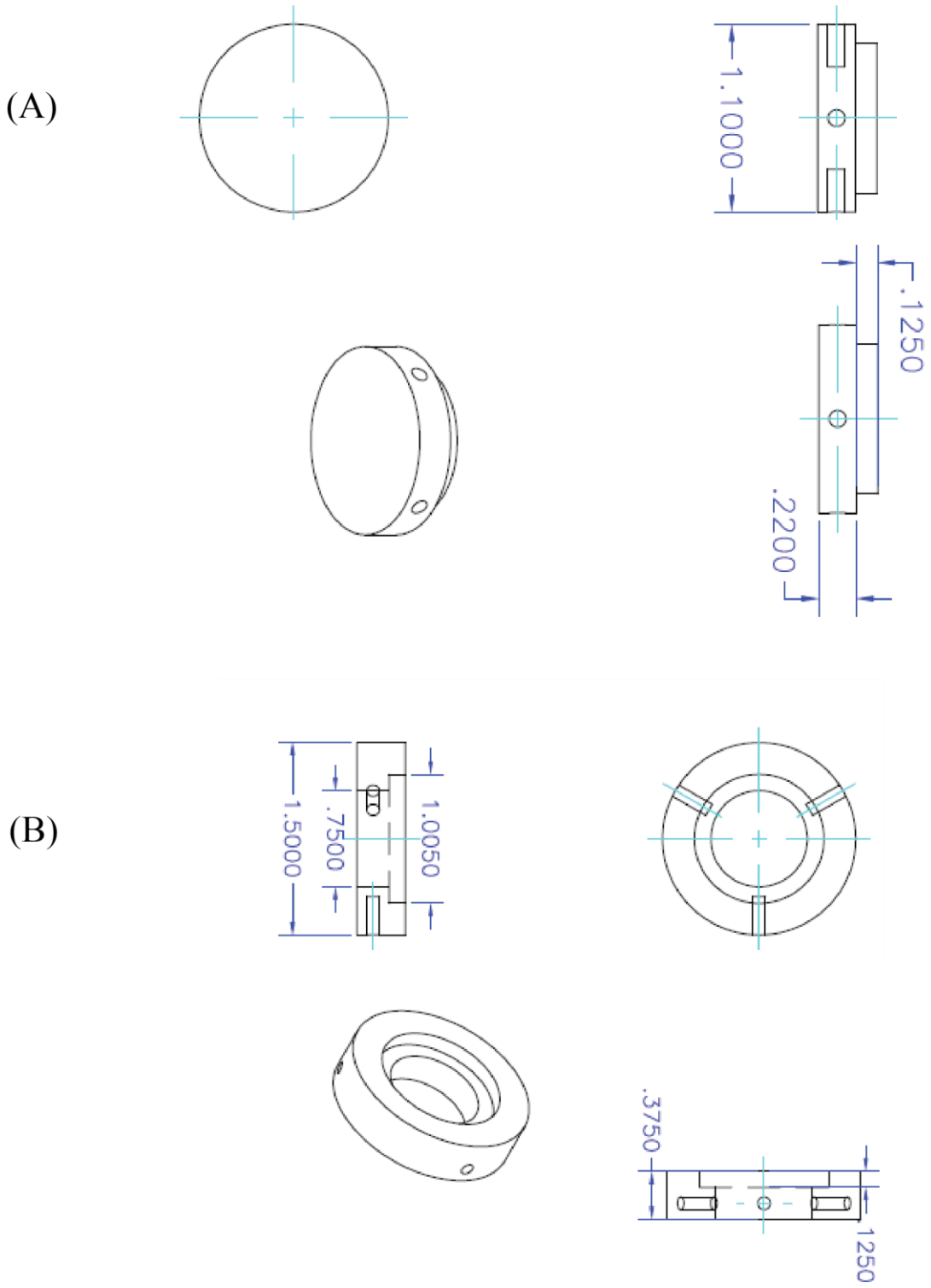

FigA.5 (A) macor piece attached to the piezo and Al mating piece, (B) macor piece attached to the piezo and Al housing.

`

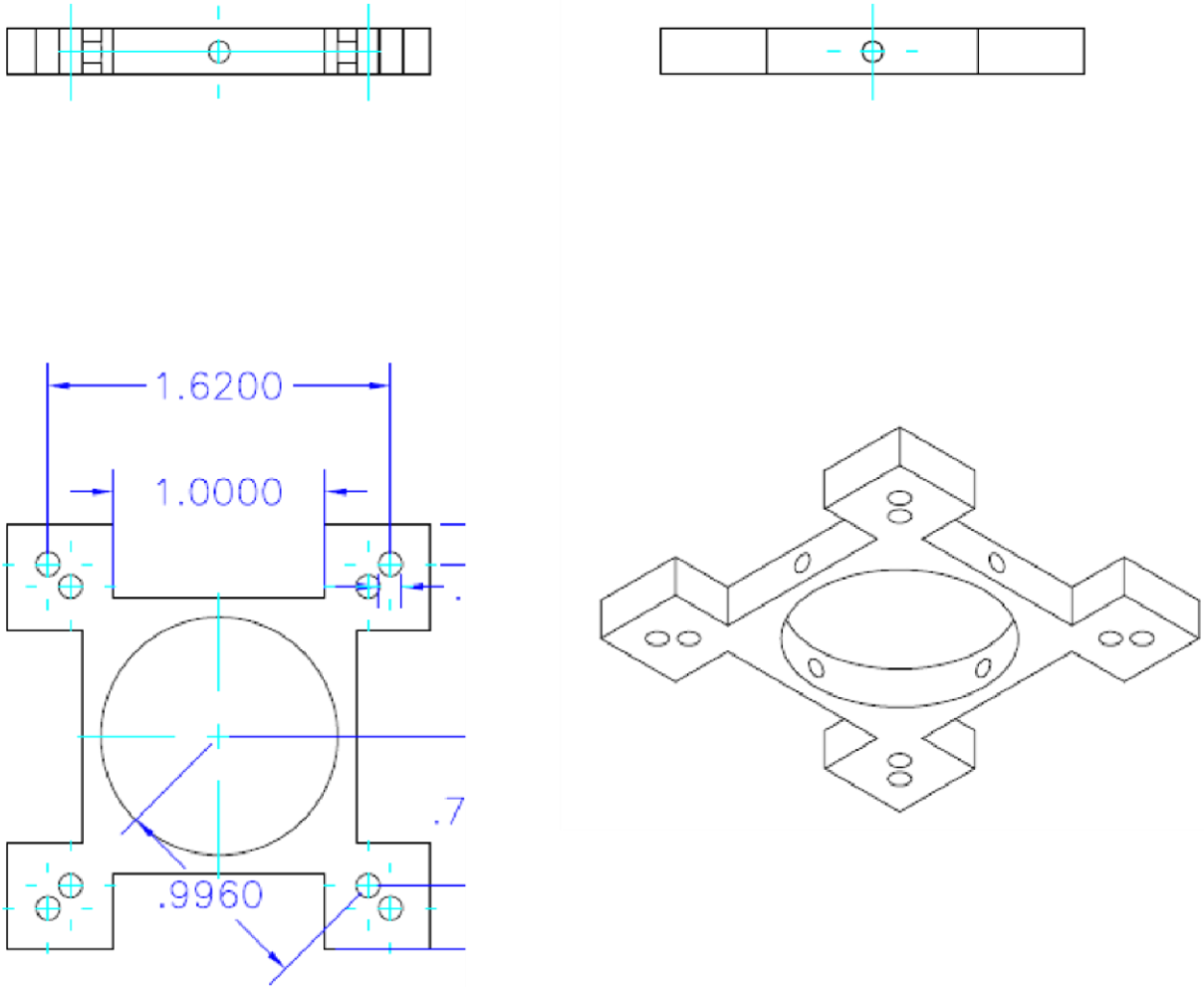

FigA.6 Al mating piece to connect the macor piece and retroreflector.

`

(A)

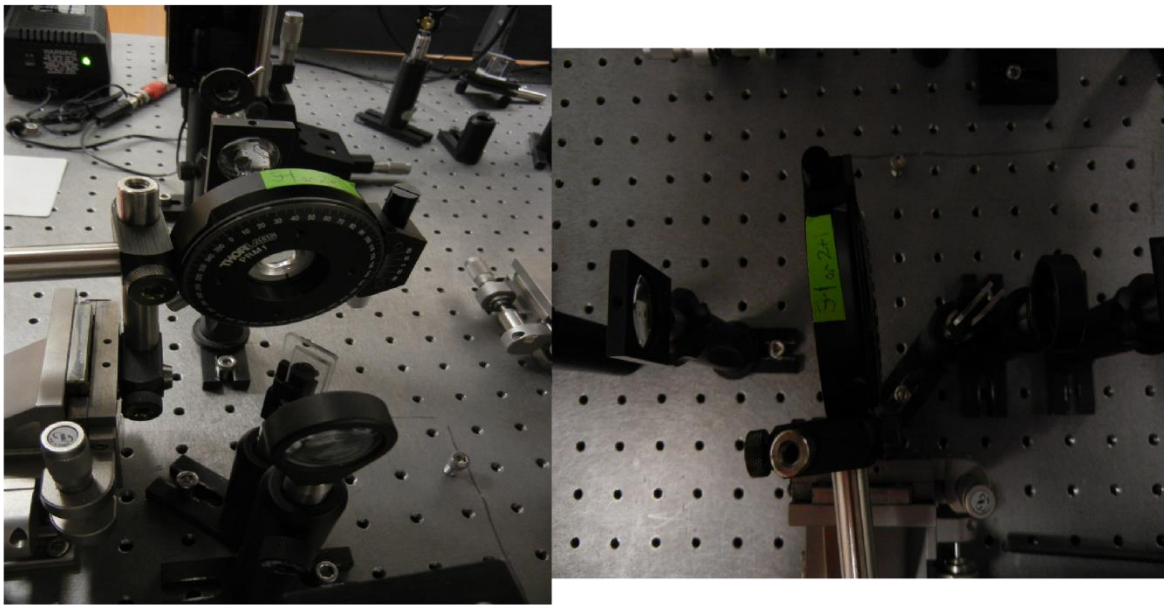

(B)

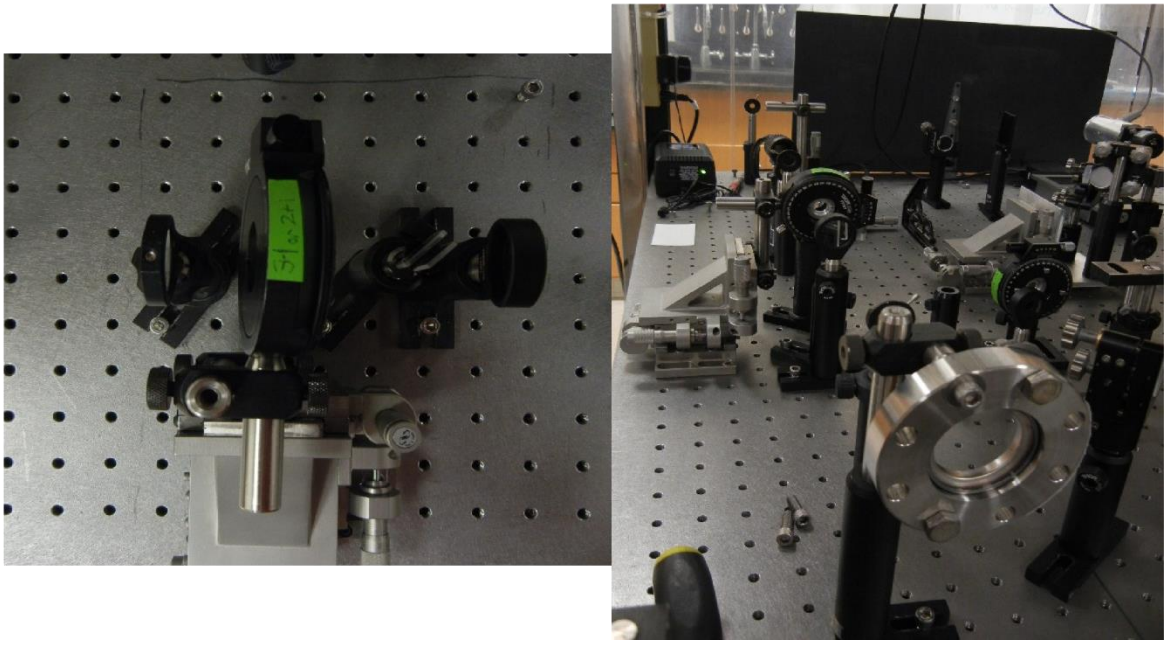

FigA.7 (A) BBO crystal position for “2+1” simulation at 840nm and 420nm, (B) crystal position for “3-1” simulation at 880nm and 293nm.

`

Appendix B

STM4 Doser Loadlock and Doser

B.1 New Lab

To couple to the new femtosecond laser described in this thesis, we need a new lab with darkroom capabilities. So the first major task for me was to move STM4 (which was in the main lab between STM1 and STM3) to the previous storage room with my partners, fig B.1 shows the initial stage and later stage of the moving, (A) shows the lab after we cleaned up and relocate the optical table, (B) shows the lab after we moved the STM and gas system. It took a few months to move the system and debug, making it back to work.

B.2 New Loadlock and Other Ports Change

Before as shown in figB.2 (A), every time we want to study a new molecule or metal atom, we need to vent the whole chamber, it usually takes ~4 weeks to bake and degas until the system is ready to run experiments again. So it's desirable to have an evaporator interlock system to enable rapid turnaround of metal and molecular dosers that can be made without venting the vacuum chamber, thus allowing fast screening of molecules and metal atoms. The modified system with the new loadlock is shown in fig B.2 (B), a zoomed in image of the loadlock is shown if fig B.3 (A). To shine laser beams into the junction, two lens holder assemblies are mounted on the two sides of the chamber (3.38 ports, through hole), before dosers were mounted there. Before the gas doser was mounted on the side and a molecule doser was mounted in the front port, later we mounted Mg or C_{60} dosers on the side to form MgO on Ag (100) or C_{60} layer on Al_2O_3 at RT.

`

The gas doser now is mounted in the front with a linear stage; the gas tube can get really close to the scanner door, enabling a more effective gas or molecule dose from the gas line.

The main parts of the loadlock are a small ion pump, a getter pump, a linear translator, two gate valves, a gold seal valve and tees (crosses, reducer and nipple). The flange on the port which loadlock was assembled has a tap hole, so a short nipple is used before the gate valve, which also has tap holes. After the gate valve is a tee with a viewport, the linear translator for the dosers is attached to the straight side of the tee while the pumps connect through the other side. A six-way cross is connected to the tee first on the pumps side, one side the six-way cross is connected to the gold seal valve, the other side connects to the ion pump and getter pump through a gate valve. Three ports are blanked on the six-way cross now for later improvements like gauge or RGA. The ion pump and getter are mounted on a 4.62 inches tee, enabling bigger volume for the getter. The process to change doser is:

1 close both gate valves,

2 vent the load lock by opening gold seal valve,

3 take the old doser out,

4 put the new doser in,

5 connect the load lock to pumps,

6 start pumping, wait till the pressure reaches lowest,

7 open the valve near the pumps, activate getter pump if necessary, start baking.

B.3 New Dosers

Before the Ho group dosers use a 3.38 flange, same as the lens holder ports, the other ports are 2.75” flange, so we need a reducer to mount the dosers. Now with a 2.75 inches linear translator, new dosers with 2.75 inches are designed, machined and assembled; the vacuum length of these

`

dosers is 12.5”~13 inches. FigB.3 (B) shows a doser with water cooling. On a 2.75” flange, three holes are drilled, the center hole is for water cooling; one of the side holes is for electrical feedthrough and the other one for rotational feedthrough. The watercooling system contains a 0.375” out tube, a 0.25” inner tube and a machined water tank top, it’s very important to bend the out tube and inner tube same time before welding. It’s also very important to weld the tube concentric to the flange, usually, we can cut several tubes and roll on the flat table in the machine shop and choose the straightest one. The electrical feedthrough is from CeramTec (electrode diameter 0.094 inches); the rotational feedthrough is from MDC (less expensive ones may be found at Huttington). Home-made adaptors are used to connect the electrical feedthrough and rotational feedthrough to the 2.75 inch flange. One more hole could be made on the flange to mount the thermocouple if needed. The electrical feedthrough is connected to 30mil or 20mil W wire (which wound around a ceramic crucible) through Cu rod and Ta rod, a shaft collar is needed to fix the rods. The ceramic crucible is made by making threads on a one-end-sealed ceramic tube (0.313 inch OD, 0.188 inch ID) from Ortech. Fig B.4 (A) shows the drawing of the doser after machining and welding, fig B.4 (B) shows the dimension of the welding holes on the 2.75” flange. Fig B.5 (A) shows the dimension of the one-end sealed water tank; fig.5 (B) shows the dimension of the adapter to weld to the 2.75 inches flange to connect the electrical feedthrough.

Fig B.3 (C) shows a dual-doser with two crucibles mounted, enabling co-evaporation of two molecules same time onto the surface, the inset shows the top view of the two crucibles. It needs two smaller crucibles to fit into the space and a good isolation between the two crucible housings; two pairs of electrodes are needed to heat up the crucibles. Fig B.6 (A) is the drawing after the doser is assembled. The top shield and crucible structure are supported by two 6-32

`

screw rods, given that the top structure is heavy and the doser is 13” long, stainless steel tubes are needed to outfit the screw rods to stabilize. A home-made shaft collar is needed to clamp in the middle. Fig B.6 (B) shows the dimension of the welding holes and tap holes on the flange and fig B.6 (C) shows the dimension of the shaft collar. Fig B.7 shows the housing structure for the two crucibles, it’s made up of three pieces, the body structure as shown in (A), the separating piece as shown in (B) and the cover as shown in (C). To make smaller crucibles for the new dual doser, new jig to cut the ceramic tubes is needed, the design is shown if figB.8, (A) shows the mail piece, (B) shows the female piece and (C) shows the clamping piece.

Below is a table of different dosers for STM4:

Doser Material	Doser Type	Crucible and Current
Mg	3.38 flange, to chamber, face junction or heater, w/ water cooling	Old fat crucible, 28~32A
K	2.75 flange, Load lock, strip from SAES getter, face junction, no need of water cooling	The strip is spot welded to the two Ta rods, 5~6A
Fe	3.38 flange, to chamber, face junction, w/ water cooling	Ceramic crucible wound with 30 mil W wires, 16~18A
C60	3.38 flange, to chamber, face heater, no water cooling	Ceramic crucible wound with 20 mil W wires, 3.4A~3.8A
Ag	3.38 flange, to chamber, face heater, w/ water cooling	Ceramic Crucible wound with 30 mil W wires, 11~12A
Au	3.38 flange, to chamber, face junction, w/ water cooling	Ceramic Crucible wound with 30 mil W wires, 14~15A
Th-Th-BT-Th-Th	2.75 flange, load lock, face STM junction, w/ water cooling	Ceramic Crucible wound with 30 mil W wires, around 2.75A

Table 1 Evaporators of STM4

`

(A)

(B)

Fig B.1 (A)Initial stage of the new STM4 lab (which used to be the storage room) after cleaing and setting up new optical table, (B) latter stage of the new STM4 lab after setting up the STM table and pumpig systems.

`

(A)

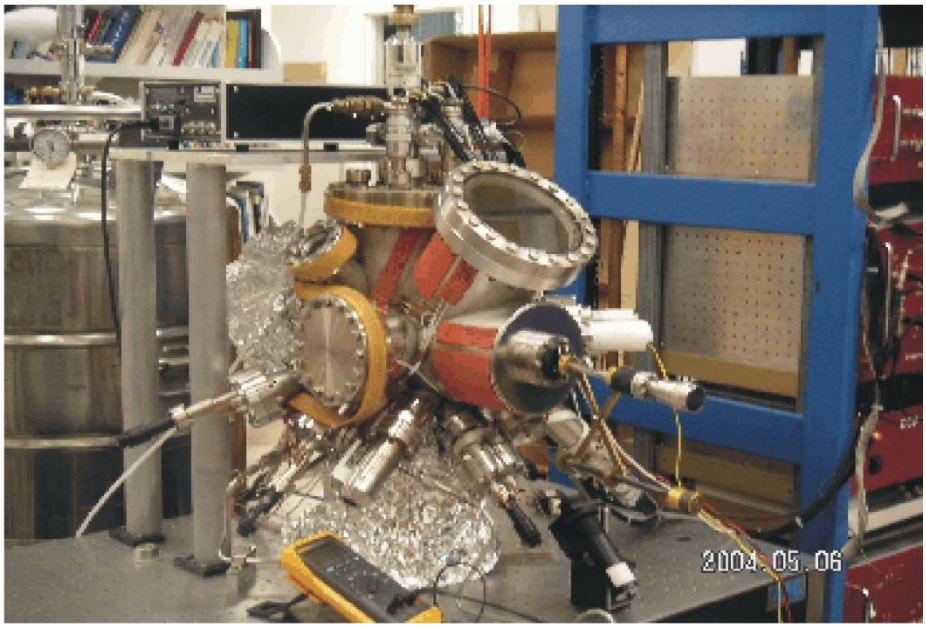

(B)

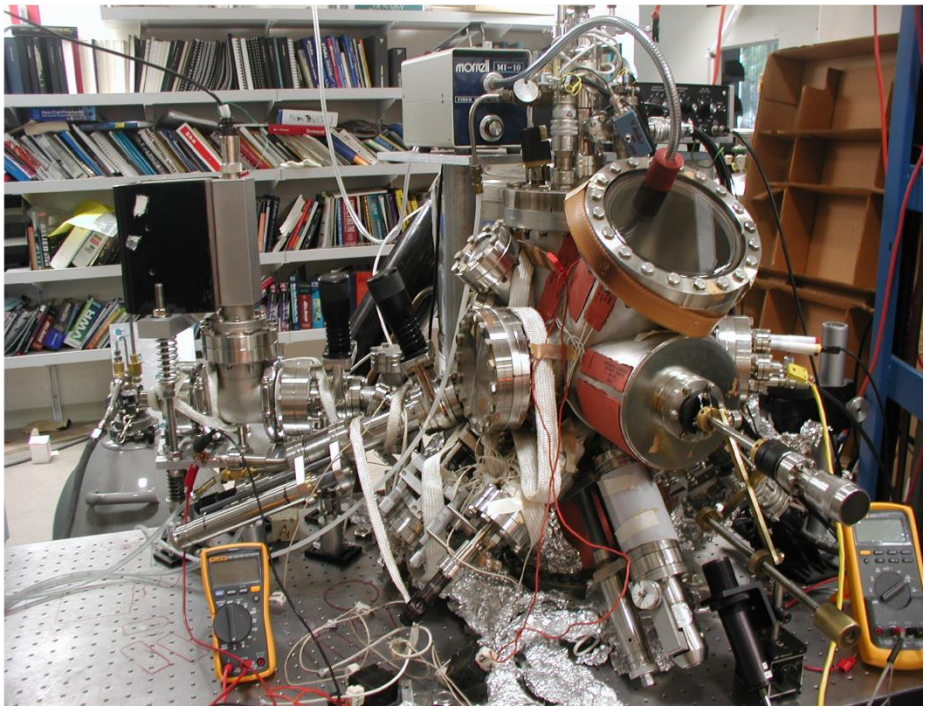

FigB.2 (A) Former STM4 setup, with no optical setup or load lock, it should be also noted that the gas doser is on the side and a molecule doser is in the front; (B)new STM4 setup, with load lock and optical setup, the gas doser is now in the front with a linear translator and a molecule or metal doser is mounted on the side facing the heater.

`

(A)

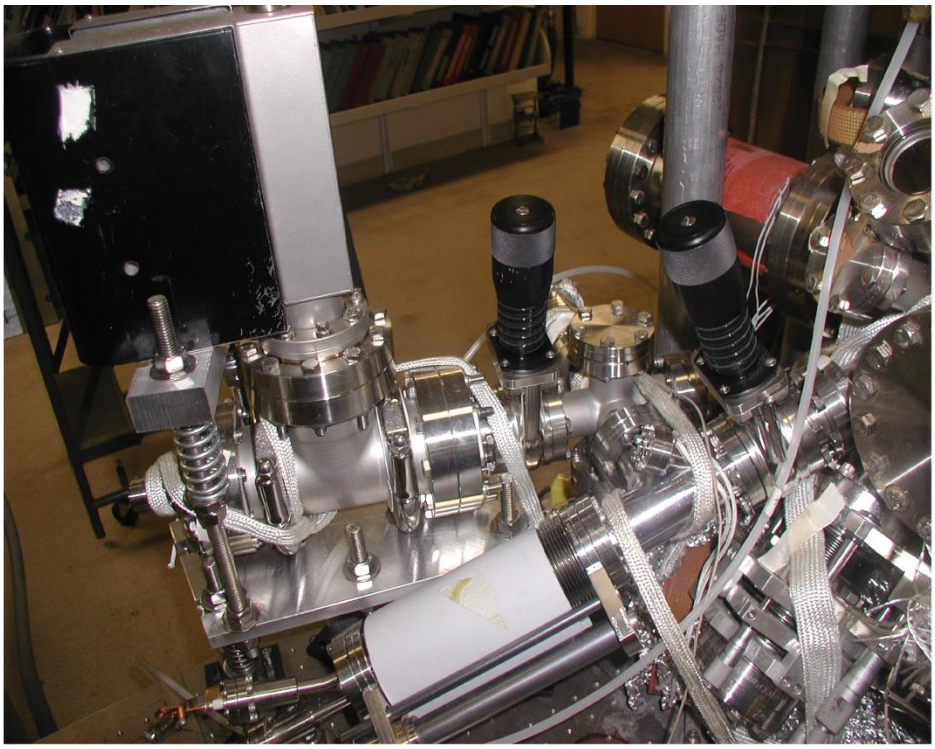

(B)

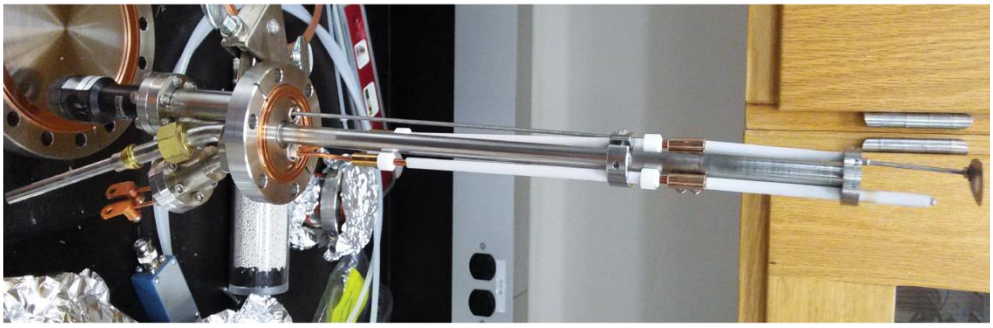

(C)

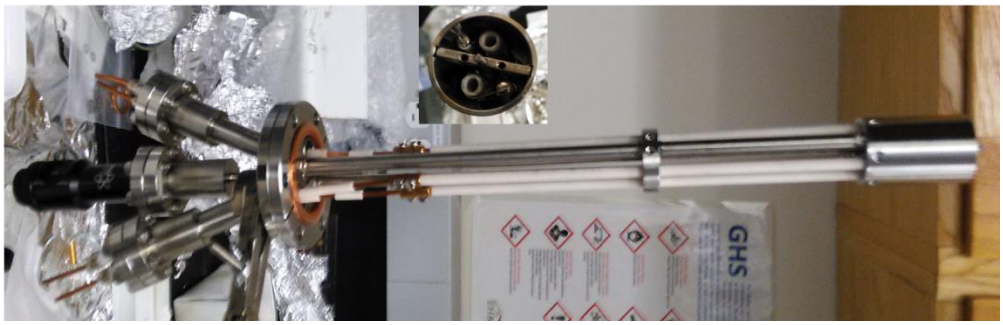

Fig B.3(A)STM4 doser loadlock system,(B)a load lock doser with water cooling, (C) a load lock doser with two crucilbe (inset) mounted.

`

(A)

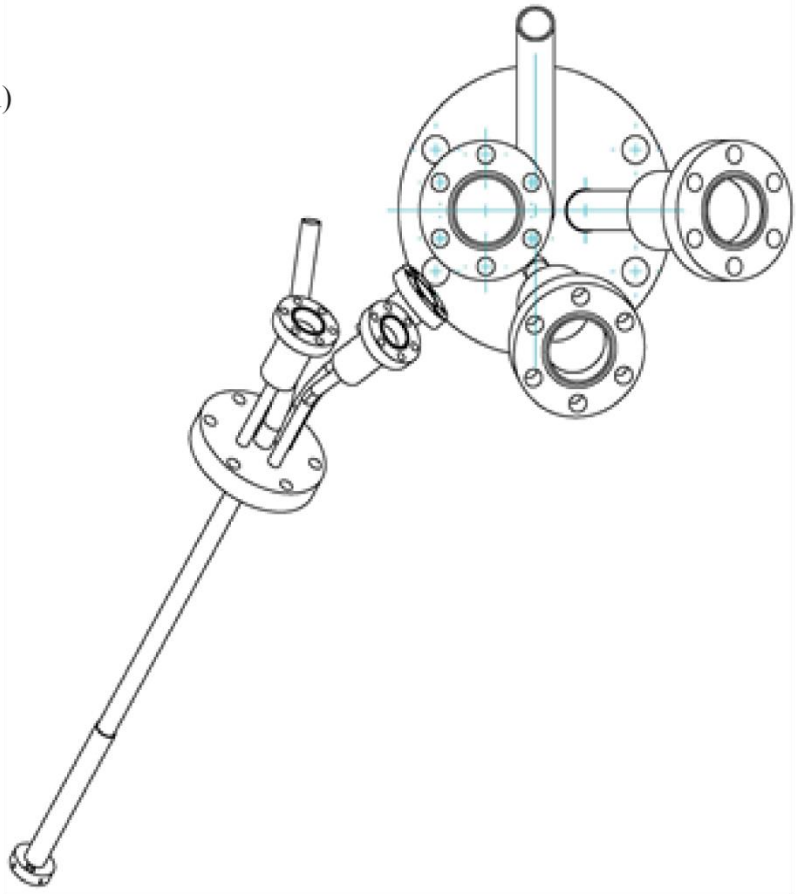

(B)

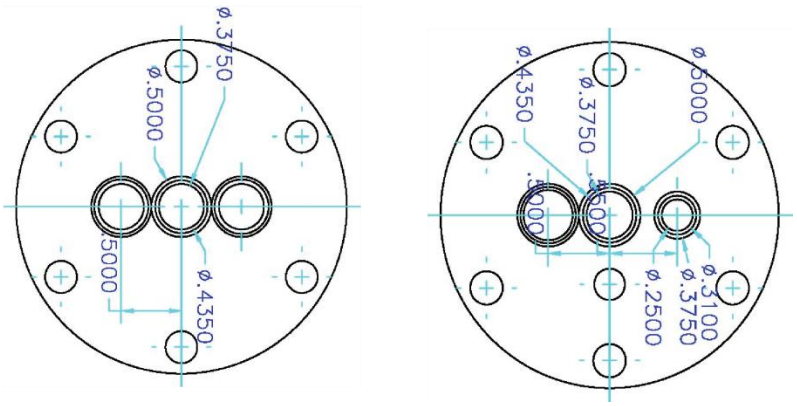

FigB.4 (A) Load lock doser with water cooling after welding, this one has a third miniflange for thermocouple, (B) two possible flange welding holes dimension, the shutter hole can be small.

`

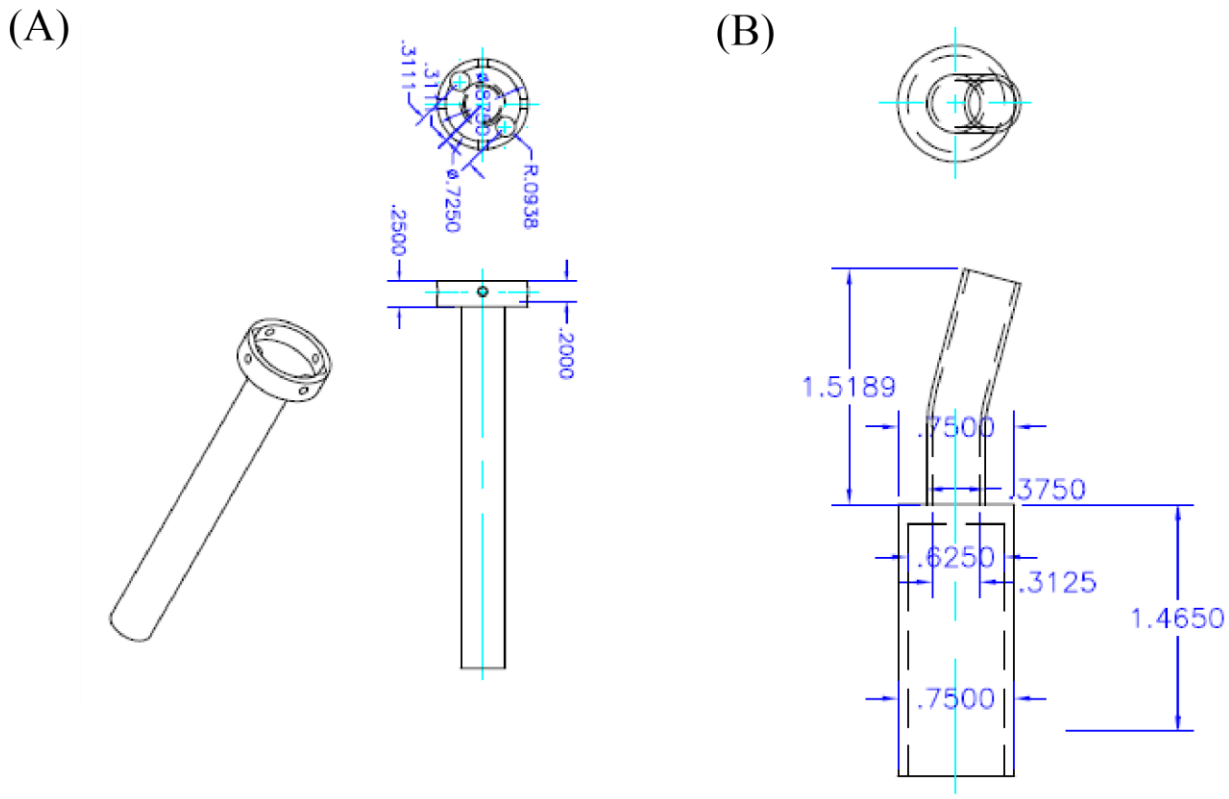

FigB.5 (A) water tank top, bottom is welded to the water flowing outer tube, top attached to the Ta shield, (B)welding adapter, top welded the 2.75" flange and bottom is welded to the minflange.

`

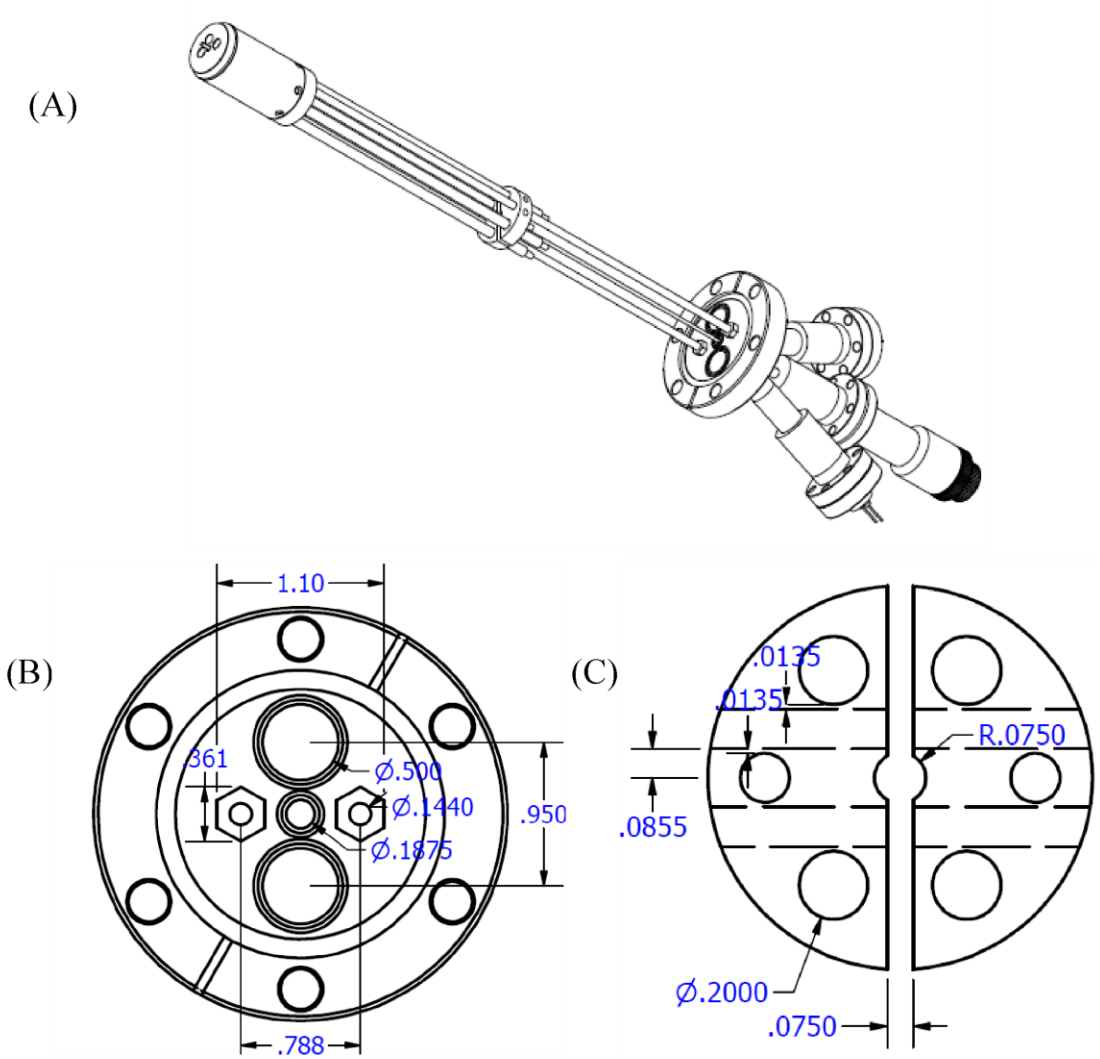

FigB.6 (A) Dual molecule evaporator with 2 crucibles, (B) flange holes dimension, (C) shaft collar dimension.

`

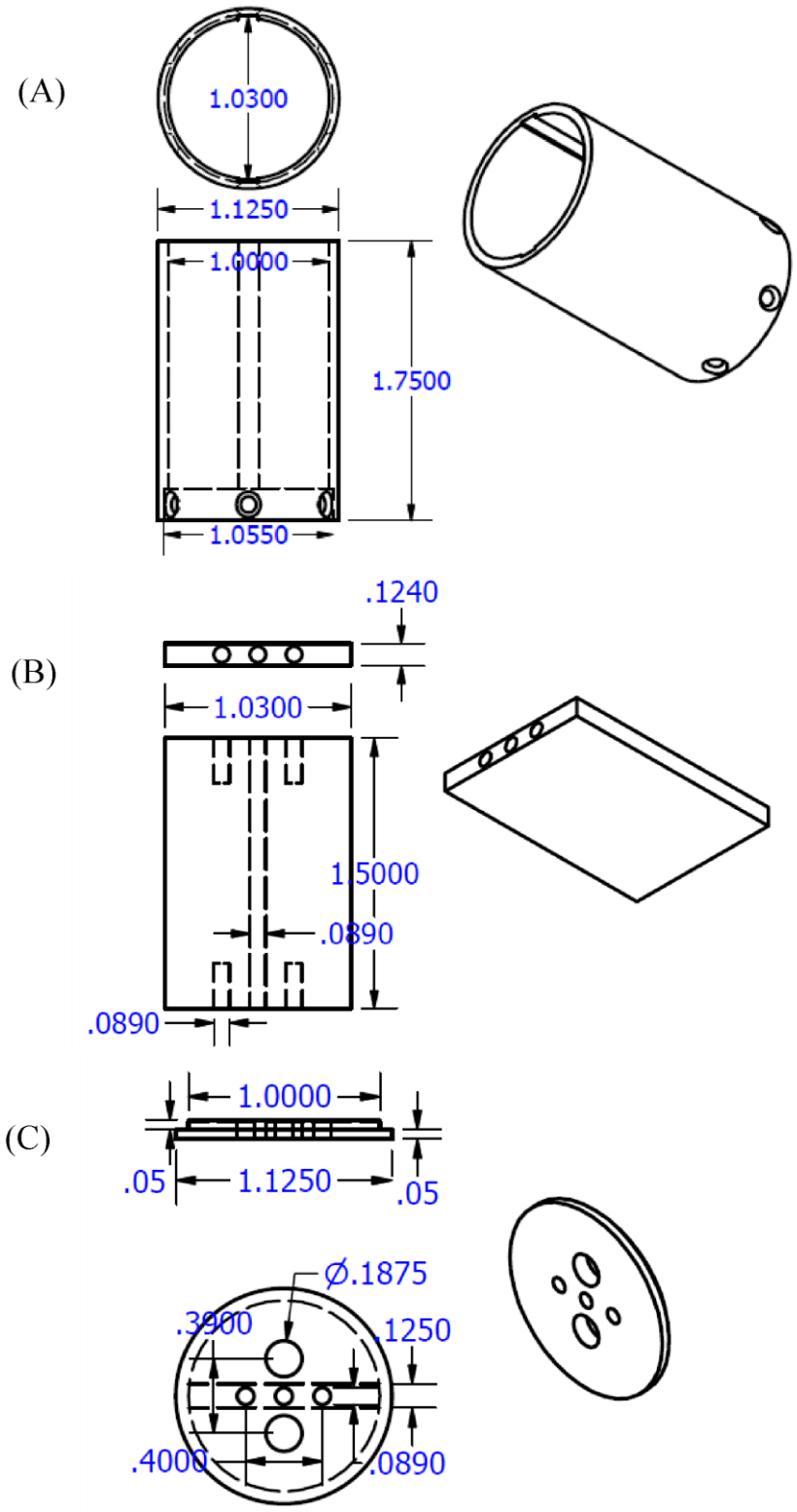

FigB.7 (A) housing body dimension, (B) housing middle piece dimension, (C) housing top piece dimension.

(A)

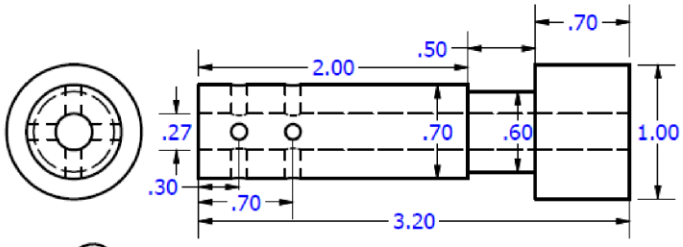

(B)

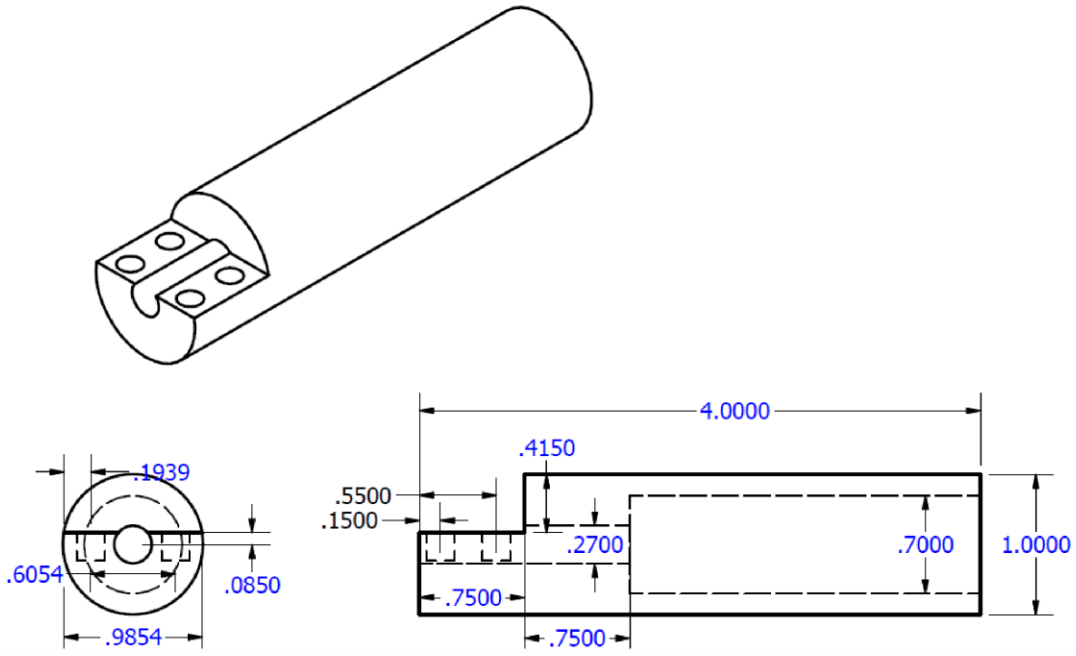

(C)

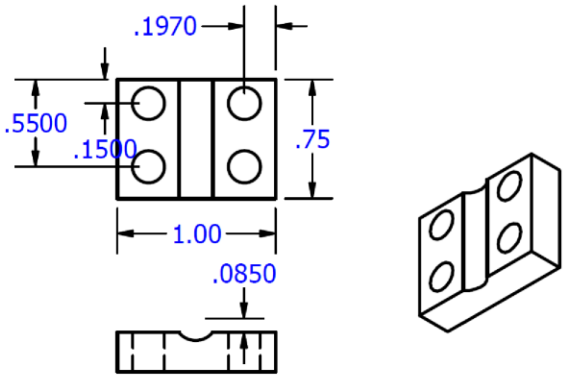

FigB.8 (A) mail piece for the jig, (B) female piece for the jig, (C) top clamping piece for the jig.